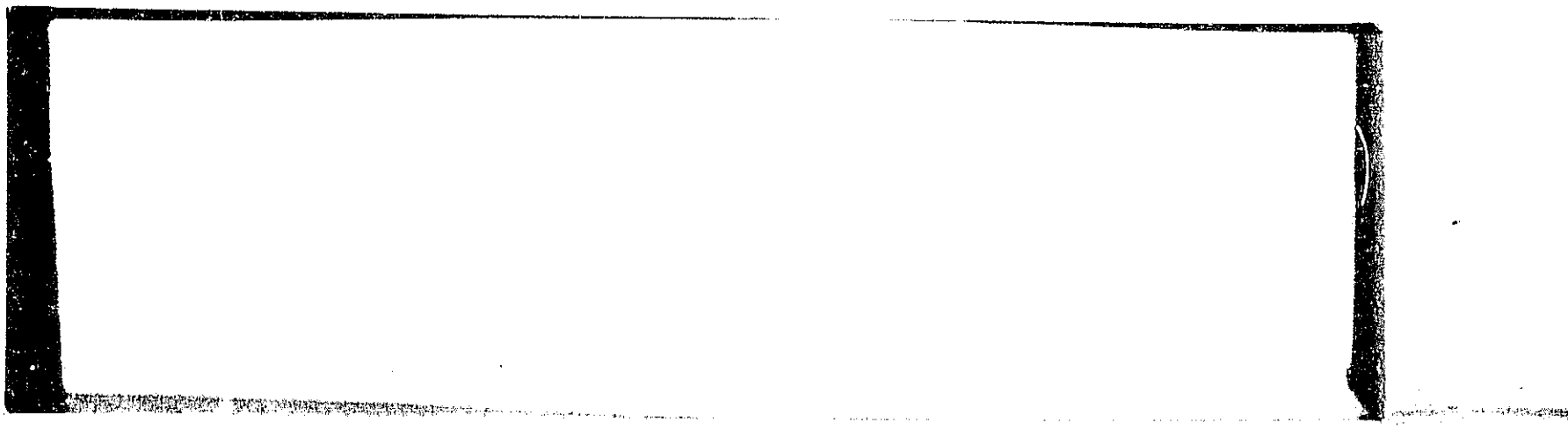

TEXAS INSTRUMENTS
INCORPORATED

03

HEAT STERILIZABLE AND IMPACT RESISTANT Ni-Cd BATTERY DEVELOPMENT

Jet Propulsion Laboratory
Contract No. 951972, Modification No. 10

Report for Ninth Quarter
July 1 to September 30, 1969

by

P. V. Popat, Project Manager

Principal Contributors:

R. L. Crawford - Electrochemistry
J. M. Gondusky - Impact Resistant Cells
E. J. Rubin - Battery Engineering

TEXAS INSTRUMENTS INCORPORATED
Research and Development Laboratories
Attleboro, Massachusetts

This work was performed for the Jet Propulsion Laboratory, California Institute of Technology, sponsored by the National Aeronautics and Space Administration under Contract NAS-7-100; Task Order No. RD-26.

NOTICE

This report was prepared as an account of Government-sponsored work. Neither the United States, nor the National Aeronautics and Space Administration (NASA), nor any person acting on behalf of NASA

(a) makes warranty of representation, expressed or implied with respect to the accuracy, completeness, or usefulness of the information contained in this report, or that the use of any information, apparatus, method, or process disclosed in this report may not infringe privately owned rights;

(b) assumes any liabilities with respect to the use of, or for damages resulting from the use of any information, apparatus, method or process disclosed in this report.

As used above, "person acting on behalf of NASA" includes any employees or contractor of NASA, or employee of such contractor to the extent that such contractor, prepares, disseminates, or provides access to any information pursuant to his employment with such contractor.

Request for copies of this report should be referred to:

National Aeronautics and Space Administration
Office of Scientific and Technical Information
Attention: AFSS-A

1. Introduction

This is the ninth quarterly report on the heat-sterilizable, as well as heat-sterilizable and impact resistant Ni-Cd battery research and development under Jet Propulsion Laboratory Contract No. 951972 Modification No. 6. The program is sponsored under NASA Contract NAS-7-100, Task Order No. RD-26. The object of this contract is to perform research development and engineering work leading to the design, development, engineering, manufacture and testing of hermetically sealed, rechargeable nickel-cadmium cells capable of heat sterilization as well as heat sterilization and impact landing for space missions.

Since the last quarterly report, several modifications have been made in the technical portion of the work statement. The several tasks under the modified work statement may be grouped under the following three broad headings:

1. Electrochemistry of Heat-sterilizable Cells. This will include basic research and development work on the positive and negative plates and separator as well as design, assembly and testing of complete cells leading to batteries capable of satisfactory operation after undergoing heat sterilization.

2. Battery Engineering. This will include full size cell design, development, optimization, production and testing of heat-sterilizable cells. Initially, two

designs (a) cylindrical and (b) rectangular (prismatic) of 25 AH nominal capacity will be developed and evaluated. Hermetic seal design, assembly and testing to withstand the heat sterilization will be part of the battery engineering Program.

3. Impact Testing of Cells and Components. Both static and dynamic testing of seals, cases, plates, and complete cells will be performed up to approximately 4000 g in order to develop data for the design of cells capable of hard impact landing missions.

The work performed during the ninth quarter is reported in the following pages.

I. DEVELOPMENT OF HEAT-STERLIZABLE Ni-Cd CELLS

SECTION I -- ELECTROCHEMISTRY OF HEAT-STERILIZABLE CELLS

TABLE OF CONTENTS

SECTION I -- ELECTROCHEMISTRY OF HEAT-STERILIZABLE CELLS

LIST OF TABLES

I. ELECTROCHEMISTRY OF HEAT-STERILIZABLE CELLS

TASK V. Electrochemical Mechanism Investigation

a. The problem of lowering of delivered capacity of post-sterilized cells has been practically solved by improved assembly techniques, active material ratios and cell conditioning. This is shown by two types of tests: (1) the capacity of 4 AH prismatic, 17-plate factorial cells after 248 deep discharge post-sterilization cycles is that expected for the positive limited cells, based upon the formation capacity of unsterilized positive plates. Similarly, the capacity of 4 AH, prismatic, 18-plate experimental cells for reproducibility studies show the same predicted capacity for positive limited cells after 189 deep discharge cycles; (2) the 25 AH cylindrical engineering cells designed, built, characterized, heat sterilized and cycled during this contract have shown no capacity lowering during post-sterilization charge-discharge cycles (over 65 deep discharge cycles after sterilization) at C/10 rate of charge and C/2 rate of discharge. It is therefore concluded that the problem of capacity lowering of post-sterilization cells now does not exist.

In some cases, with experimental 4 AH cells, we have observed a lower efficiency of active material utilization during presterilization characterization. No significant change in the post-sterilization capacity was observed. Detailed investigation using reference electrode in sealed as well as vented flooded cell experiments has shown that in these cases, the cells had become negative limited on discharge due to insufficient charged cadmium (charge adjust) in these cells. Either the charge adjust was initially insufficient or else the excess cadmium

got oxidized during storage and handling. Since this parameter influences the weight and volume energy density, it is necessary to determine the optimum charge adjust for heat-sterilizable cells for best performance. Two types of experiments are being performed with sealed cells. The parameters investigated for various lot materials and other experimental details are given in Tables I and II. The effect of lot materials on the electrochemical performance is generally minor, although in some cases the difference in efficiency is as high as 10%. For details see Table III. The effect of the charge adjust on the capacity of unsterilized cells is small. This was not expected. We still do not know why variation in charge adjust did not result in capacity variation. Data are given in Table IV.

b. Higher end-of-charge voltage after sterilization. As reported earlier, there has been consistently observed slightly higher (30 to 60 mV) end-of-charge voltage after heat sterilization. Cell gas analysis and individual (single) electrode potential measurements using reference electrodes have shown this increase to be associated with nickel electrode. The important finding from the point of view of cell performance is that this higher voltage is not associated with hydrogen evolution. This eliminates the problem of pressure built up during charge.

The higher polarization of the sterilized nickel electrode may be due to a reduction in the surface area resulting in higher current density and/or higher oxygen over-voltage after sterilization. To separate the two effects will require a lot more fundamental work on

TABLE I-I

EXPERIMENTAL PLAN TO DETERMINE THE EFFECTS OF LOT MATERIALS ON CELL PERFORMANCE

Fixed Parameters: 4 AH, 18-plate, prismatic sealed cells; FT2140 polypropylene separator, 80% pore fill with 30% KOH, room temperature.

I. FACTORS	Levels (Lot Type or No.)	
A. Positives	#175	#155
B. Negatives	#183	#170
C. Separator Lot	R&D	Production
D. KOH Lot	R&D	Production

II. CELL CHARACTERIZATION

Five cycles presterilization, 5 cycles post-sterilization under the following cycling routine:

A. Charge Rate - 0.400 A

B. Charge Level - 137%

C. Discharge Rate - 2.00 A to 1.0 volt cutoff (100% d.o.d.)

III. CHARACTERISTICS MEASURED

ECV, ECR, EDR, ECC, Efficiency.

TABLE I-2

EFFECT OF CHARGE ADJUST

Fixed parameters, cell characterization, charge routine and characteristics measured: Same as in Table I.

Factors to be Evaluated	Levels (AH)			
Charge Adjust	0.00	0.50	1.00	2.00

Lot Materials: Positive #175, Negative #183, R&D Separator and KOH

TABLE I-3

Ni-Cd Rectangular Cells; Factorial Design Experiment

ELECTROCHEMICAL PERFORMANCE DATA

FOR FACTOR DESCRIPTION AND LEVELS SEE TABLE I

EFFECT OF LOT VARIATION

Pre-sterilization
Cycle #4

Cell No.	Factors				Cycle No.	Charge Data						Discharge Data; 1.0V Cut Off				
	A	B	C	D		Amp.	Hrs.	AH Input	ECV Volts	ECP PSIA	ECR mΩ	Amp	AH Output	EDP PSIA	EDR mΩ	Eff. %
1	0	0	0	0	4	.4	17	6.8	1.430		7.17	2.0	3.166		9.73	60.4
2	0	0	1	0	4	.4	17	6.8	1.429		12.68	2.0	3.118		11.80	59.5
3	0	0	0	1	4	.4	17	6.8	1.426		11.37	2.0	3.334		10.23	63.6
4	0	0	1	1	4	.4	17	6.8	1.432		11.82	2.0	3.134		11.22	59.8
5	0	1	0	0	4	.4	17	6.8	1.424		11.44	2.0	3.752		10.93	71.6
6	0	1	1	0	4	.4	17	6.8	1.423		11.16	2.0	3.500		10.74	66.8
7	0	1	0	1	4	.4	17	6.8	1.426		11.34	2.0	3.900		10.84	74.4
8	0	1	1	1	4	.4	17	6.8	1.438		12.69	2.0	4.066		12.03	77.6
9	1	0	0	0	4	.4	17	6.8	1.418		10.29	2.0	3.052		9.64	58.2
10	1	0	1	0	4	.4	17	6.8	1.433		11.34	2.0	3.066		10.62	58.5
11	1	0	0	1	4	.4	17	6.8	1.421		11.06	2.0	3.018		10.59	57.6
12	1	0	1	1	4	.4	17	6.8	1.430		11.15	2.0	3.334		10.51	63.6
13	1	1	0	0	4	.4	17	6.8	1.420		11.37	2.0	3.584		10.90	68.4
14	1	1	1	0	4	.4	17	6.8	1.431		9.88	2.0	3.666		9.22	70.0
15	1	1	0	1	4	.4	17	6.8	1.421		11.86	2.0	3.652		11.40	69.7
16	1	1	1	1	4	.4	17	6.8	1.443		10.45	2.0	4.100		9.63	78.2

TABLE I-4

Ni-Cd Rectangular Cells; Factorial Design Experiment

ELECTROCHEMICAL PERFORMANCE DATA

FOR FACTOR DESCRIPTION AND LEVELS SEE TABLE I

EFFECT OF LOT VARIATION

Post-sterilization Cycle #9

Cell No.	Factors				Cycle No.	Charge Data						Discharge Data; 1.0V Cut Off				
	A	B	C	D		Amp.	Hrs.	AH Input	ECV Volts	ECP PSIA	ECR mΩ	Amp	AH Output	EDP PSIA	EDR mΩ	Eff. %
1	0	0	0	0	9	14	17	6.8	1.489		11.60	2.0	2.952		9.67	56.3
2	0	0	1	0	9	14	17	6.8	1.476		11.95	2.0	2.666		11.21	50.9
3	0	0	0	1	9	14	17	6.8	1.481		11.88	2.0	2.918		9.87	55.7
4	0	0	1	1	9	14	17	6.8	1.478		11.48	2.0	2.800		10.83	53.4
5	0	1	0	0	9	14	17	6.8	1.466		11.35	2.0	2.972		10.61	56.3
6	0	1	1	0	9	14	17	6.8	1.460		10.55	2.0	2.918		10.28	55.7
7	0	1	0	1	9	14	17	6.8	1.470		12.14	2.0	2.966		10.48	56.6
8	0	1	1	1	9	14	17	6.8				2.0				
9	1	0	0	0	9	14	17	6.8	1.481		11.22	2.0	3.200		9.26	61.1
10	1	0	1	0	9	14	17	6.8	1.477		11.61	2.0	3.000		10.52	57.3
11	1	0	0	1	9	14	17	6.8	1.480		12.20	2.0	3.118		10.83	59.5
12	1	0	1	1	9	14	17	6.8	1.470		10.86	2.0	3.184		10.15	60.8
13	1	1	0	0	9	14	17	6.8	1.460		12.31	2.0	3.100		11.61	59.2
14	1	1	1	0	9	14	17	6.8	1.464		9.30	2.0	3.984		9.13	76.0
15	1	1	0	1	9	14	17	6.8	1.463		13.68	2.0	3.052		13.75	58.2
16	1	1	1	1	9	14	17	6.8	1.459		9.37	2.0	3.084		9.71	58.9

TABLE I-5

EFFECT OF CHARGE ADJUST

Test Conditions; C.R. = C/13.1, C.L. - 129.8%, c.c. = 400 ma, D.R. = C/2.62, D.C. = 2.0 A

	AVERAGE EFFICIENCY (%)			
Cycle No.	0.0 A.H. Charge Adjust	0.5 A.H. Charge Adjust	1.0 A.H. Charge Adjust	2.0 A.H. Charge Adjust
1	52.0	65.0	- *	60.4
2	67.9	70.7	72.7	67.8
3	69.8	69.9	74.0	73.2
4	71.0	71.9	68.1	70.8
5	73.1	74.9	70.3	74.6
6	73.8	75.2	72.9	76.7
7	71.4	75.8	76.1	78.5
8	74.4	75.3	74.4	76.1
9	78.6	75.6	72.9	75.7
10	73.7	79.0	73.8	75.4
Average	70.6	73.3	72.8	72.9

* Not included in average

TABLE I-6

PERFORMANCE OF RAI TREATED EM-476 SEPARATOR IN 4 AH RECTANGULAR CELLS

Test Conditions: C.R. = C/12.4; C.L. = 137%;c.c. = 400 ma; D.R. = C/2.5; D.C. = 2.0 A
Cell Type: 18-Plate (10 neg - 8 pos), Cell #1, 1-layer EM-476; Cell #2, 2-layer EM-476

Cycle No.	Cell No.	E.C.V.	O.C.V.	E.C.R. (mΩ)	E.D.R. (mΩ)	Eff. (%)
1	1	1.460	1.416	10.20	9.61	78.6
	2	1.461	1.413	16.22	14.93	61.8
2	1	1.464	1.402	10.25	9.05	80.0
	2	1.465	1.397	15.87	13.89	67.9
3	1	1.486	1.396	9.93	9.38	80.3
	2	1.509	1.393	15.36	13.89	69.2
4	1	1.551	1.384	10.36	9.50	82.3
	2	1.582	1.383	17.23	14.02	71.9
5	1	1.577	1.405	10.27	9.50	82.0
	2	1.589	1.405	17.05	15.35	71.2
6	1	1.600	1.434	11.14	9.69	80.6
	2	1.613	1.430	19.26	18.21	68.9
7	1	1.590	1.450	10.76	10.42	78.6
	2	1.599	1.443	18.69	20.81	65.2
8	1	1.603	1.414	10.83	11.76	75.3
	2	1.511	1.390	17.50	18.72	63.5

(1) Cells made with a single of separator show lower resistance and higher efficiency than cells made with two layers of separator.

(2) The end-of-charge voltage is higher than for cells made with untreated FT2140 separator.

the oxygen electrode kinetics on complex nickel hydroxide electrode and the BET surface area measurements then planned. Since this higher end-of-charge voltage does not affect the cell performance and since it is doubtful whether it can be completely eliminated as a result of fundamental work, it is recommended that this aspect may not be pursued further at this time. With this qualification the task is essentially complete.

TASK VI. Sealed Cell Design Optimization

Major portion of this task with 4 AH prismatic cells has been completed and this technology has been extended to the 25 AH prismatic, engineering prototype cells. The design and performance data for these two sizes of cells have been reported earlier and additional data are reported in Section II of this report. Specifically, the work on the selection and optimization of the heat-sterilizable separator capable of long cycle life has been completed. A new separator, RAI P-476-22 Roll #B-04-0101-022, composed of irradiated, crosslinked EM-476 polypropylene and supplied by Jet Propulsion Laboratories has been evaluated and the results are given in Table V. The work on electrolyte composition and amount is also completed except for the effect of LiOH addition to the electrolyte. The work in progress on this study was terminated as per Jet Propulsion Laboratories instructions. The work on the packaging parameters (core compression for prismatic cell) is also completed. These cells have been characterized prior to sterilization. Post-sterilization characterization data will be presented in the Final Report.

TABLE I-7

Ni-Cd Rectangular Cells; Factorial Design Experiment
ELECTROCHEMICAL PERFORMANCE DATA
FOR FACTOR DESCRIPTION AND LEVELS SEE BELOW

Cell No.	Factors				Cycle No.	Charge Data						Discharge Data; 1.0V Cut Off				
	A	B	C	D		Amp.	Hrs.	AH Input	ECV Volts	ECP PSIA	ECR mΩ	Amp	AH Output	EDP PSIA	EDR mΩ	Eff. %
17	1	0	0	1	248	.400	17.0	6.8	1.467	---	18.59	2.0	2.918	---	47.1	58.8
						.400	17.0	6.8								
19	1	0	0	1	248	.400	17.0	6.8	1.461	---	21.77	2.0	3.300	---	42.2	66.5
						.400	17.0	6.8								
						.400	17.0	6.8								
21	1	0	1	1	248	.400	17.0	6.8	1.471	---	10.89	2.0	3.834	---	12.2	77.3
						.400	17.0	6.8								
23	1	0	1	1	248	.400	17.0	6.8	1.568	---	21.50	2.0	3.934	---	27.0	79.3
						.400	17.0	6.8								
						.400	17.0	6.8								
25	1	1	0	1	248	.400	17.0	6.8	1.484	---	15.36	2.0	2.884	---	53.1	58.1
						.400	17.0	6.8								
* 27	1	1	0	1	248	.400	17.0	6.8								
						.400	17.0	6.8								
						.400	17.0	6.8								
29	1	1	1	1	248	.400	17.0	6.8	1.501	---	10.46	2.0	4.166	---	12.0	84.0
						.400	17.0	6.8								
31	1	1	1	1	248	.400	17.0	6.8	1.477	---	13.83	2.0	4.234	---	18.8	85.4
						.400	17.0	6.8								

SEPARATOR
A 0 14019
1 FT2140

CONCENTRATION KOH
B 0 30%
1 34%

PORE FILL
C 0 70%
1 80%

D 0 Unsterilized
1 Sterilized

TASK VII. Performance and Cycle Life Tests of Sealed Cells

Since we have already demonstrated the capability of 4 AH experimental, heat-sterilized cells up to 260 cycles at 100% depth of discharge without performance (capacity) loss, no further routine cycling is planned with these 17-plate and 18-plate cells. A program of characterization is now being formulated to characterize these cells at various charge levels, charge rates and discharge rates. This program will be coordinated with long-range testing program. The cycling data for these cells are given in Tables VI and VII.

Table I-8

Ni-Cd, RECTANGULAR, 18-PLATE CELLS

30% KOH, 80% Pore Fill, FT2140 Separator

Post-Sterilization Data

C.R. = C/12.5 C.L. = 137% D.R. = C/2.5

CELL No.	CYCLE No.	ECV Volts	ECR mΩ	EDR mΩ	ECC mΩ	% EFF.
1	188	1.459	11.78	14.14	3.952	79.7
2	188	1.468	11.36	11.09	4.052	81.7
3	188	1.471	11.21	12.07	4.418	89.1
5	188	1.463	17.36	30.03	4.100	82.7

II. BATTERY ENGINEERING

SECTION II -- BATTERY ENGINEERING

TABLE OF CONTENTS

SECTION II -- BATTERY ENGINEERING

LIST OF FIGURES

- Cont'd. -

SECTION II -- BATTERY ENGINEERING

LIST OF FIGURES -- CONT'D.

SECTION II -- BATTERY ENGINEERING

LIST OF TABLES

II Cell Design, Construction and Evaluation

A. Seal Development

Seals incorporating the design changes discussed in the last quarterly report have been fabricated. These changes included a reduction in polymer cross section and the use of polypropylene, as well as the KEL-F material used in the previously tested seals.

Other changes included the mechanical design discussed on page II-3 and shown in Figure II-A of the report for the 8th quarter. These seals were fabricated and leak tested on a NCR 925 mass spectrometer. There were no detectable leaks down to 1×10^{-10} std cc He sec^{-1} atm^{-1}, the limit of the device. After heat sterilization at 135°C all seals leak to the extent that the vacuum system could only maintain a pressure of 25 μ . Examination of the seals shows that in spite of the changed mechanical design the KEL-F 300 material used still flows sufficiently during the heat sterilization process to cause the seals to leak. Therefore, to form an effective heat sterilizable seal materials other than KEL-F 300 and polypropylene will have to be used.

B. Prismatic Cells

The testing of the engineering development cells continued this reporting period. The present status of these cells is shown in Table II-1

TABLE II-1

Test Status of Engineering Model Prismatic Cells

Cell Type	Cycle No	Cell Capacity (Ah)	ECV (volts)	ECP (psia)	V @ 50% DOD (volts)
Polyamide Separator	65	29.5	1.456	96	1.261
Polypropylene Separator Not H. Ster.	100	29.0	1.445	21	1.248
Polypropylene* Separator H. Ster.	34	28.0	1.488	110	1.248

* Testing discontinued after 34 cycles.

These data do not reveal, to date, any deleterious effects resulting from the use of polypropylene separator or heat sterilization.

More important for the completion of task goals, is that a group of prismatic cells were heat sterilized and tested prior to their submittal for the long range testing program. The test results of ten of these cells are shown in Figure II-A. The behavior of the cells just after heat sterilization results from high rate discharging performed in agreement with JPL, NASA Langely, and Martin Marietta, The testing included discharging these cells at the 4C rate to a 1.00 volt per cell cut-off point. This test routine resulted in an incomplete cell discharge and therefore, greater degree of overcharge, which produced higher than normal end-of-charge voltages and pressures.

After completion of these tests, the cells performed as designed.

Figure II-A

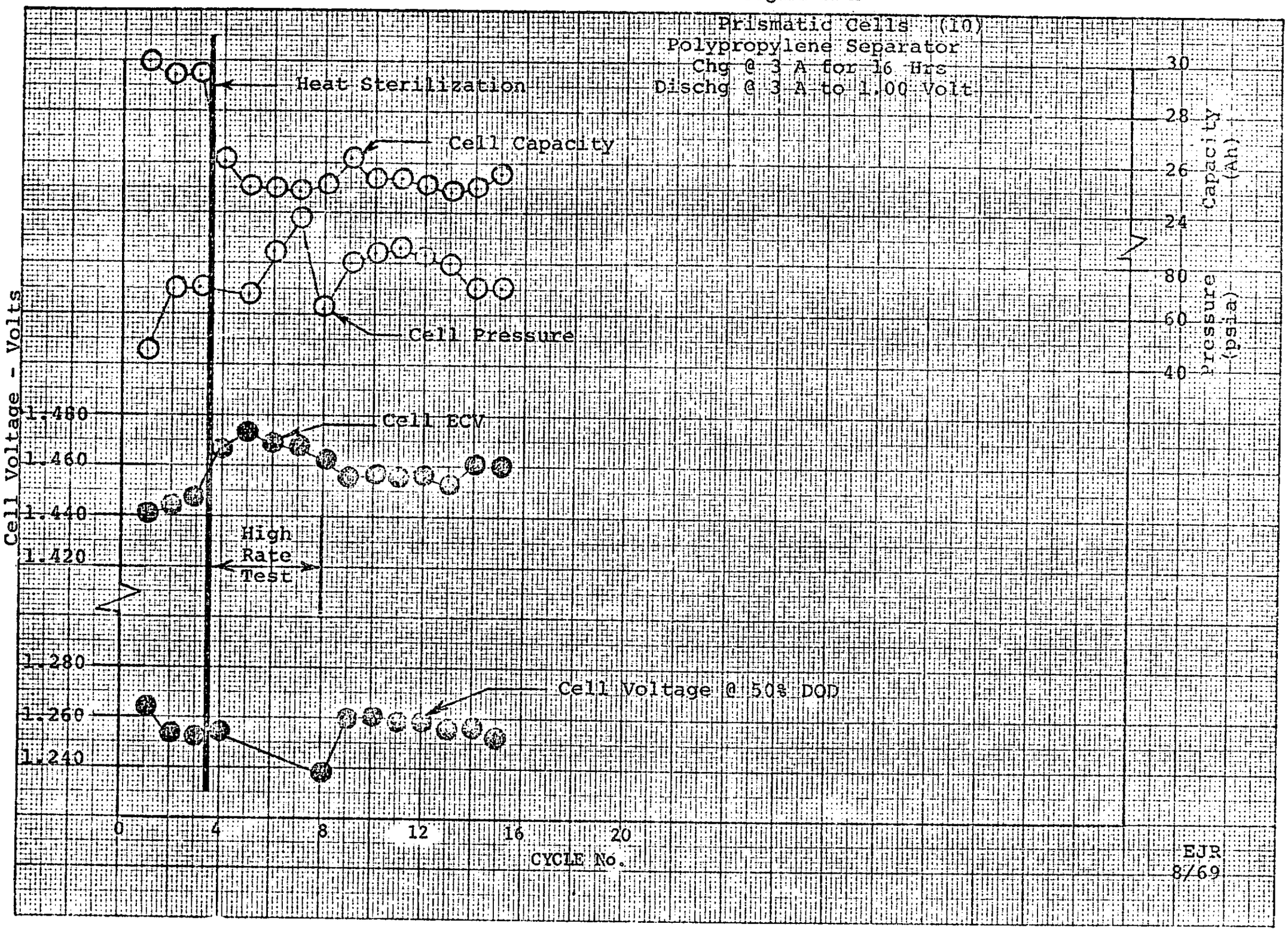
Prismatic Cells (10)
Polypropylene Separator
Chg @ 3 A for 16 Hrs
Dischg @ 3 A to 1.00 Volt
Heat Sterilization
Cell Capacity
Cell Pressure
Cell ECV
High Rate Test
Cell Voltage @ 50% DOD
Cell Voltage - Volts
1.480
1.460
1.440
1.420
1.280
1.260
1.240
Pressure (psia)
Capacity (Ah)
30
28
26
24
80
60
40
0
4
8
12
16
20
CYCLE No.
EJR 8/69

As expected, the cells showed small capacity losses and higher end-of-charge voltages. The cells' pressure and discharge voltage profile were performed on the other ten cells which comprise the remainder of this group of initial design cells. Similar performance results were obtained. The entire group of cells was then submitted for long range testing.

C. Cylindrical Cells

Testing of engineering development cells continued this reporting period. The present status of these cells is shown in Table II-2

TABLE II-2

Test Status of Engineering Model Cylindrical Cells

Cell Type	Cycle No.	Cell Capacity	ECV (volts)	ECP (psia)	V @ 50% DOD (volts)
Polyamide Separator	113	31.0	1.433	44	1.198
Polypropylene* Separator Not H. Ster.	58	22.0	1.408	60	1.170
Polypropylene Separator H. Ster.	80	29.8	1.450	70	1.226

* Testing discontinued after 58 cycles.

A group of twenty cylindrical cells were also heat sterilized and tested this reporting period. The results of testing ten of these cells are

shown in Figure II-B. These cells were also subjected to the high discharge rate testing performed on the heat sterilized prismatic cells. The effect of this test regime on these cells was similar to that observed for prismatic cells. All cells were tested and submitted to the long range test program.

D. Interim and Final Design Cells

During July a design review meeting was held with JPL representatives to discuss the various cell design parameters investigated and their effect on cell performance. It was determined that the characteristics of cylindrical and prismatic cells presented in Tables II-3 and II-4 of the Report for the Eighth Quarter represented satisfactory designs. The attributes of prismatic vs cylindrical design were discussed. The design considerations for each cell type are presented in outline form in Table II-3

TABLE II-3

DESIGN CONSIDERATIONS

I. Prismatic Cell

A. Mechanical

1. Cell packaging is more conventional
2. Physical restraints required for packaging cells
3. Thermal transport - 64 in^2 of surface
4. Cell weights = 1080 grams

B. Electrochemical

1. Limited geometric plate ratio (using conventional cross sections)

i.e. N positives, N+1 negatives

Figure II-B

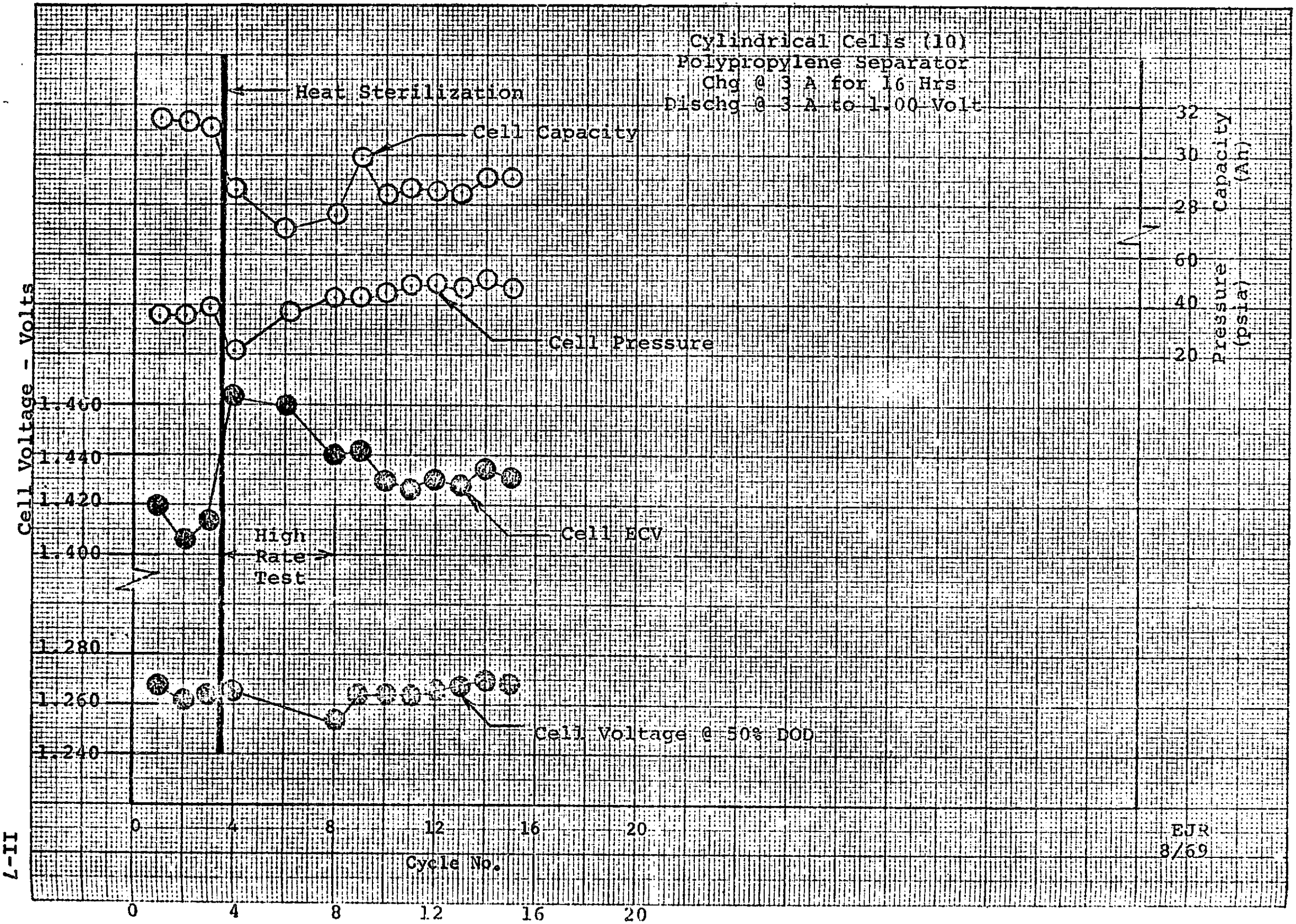
Cylindrical Cells (10)
Polypropylene Separator
Chg @ 3 A for 16 Hrs
Dischg @ 3 A to 1.00 Volt
Heat Sterilization
Cell Capacity
Cell Pressure
Cell ECV
Cell Voltage @ 50% DOD
High Rate Test
Cell Voltage - Volts
1.460
1.440
1.420
1.400
1.280
1.260
1.240
Pressure (psia)
32
30
28
60
40
20
0
4
8
12
16
20
Cycle No.
EJR
8/69

2. Limited practical negative to positive ratio

3. Operating pressure controlled by electrolyte content and plate loading

C. Effect of Sterilization

1. Higher end-of-charge voltage (than prior to sterilization)

2. 10-20% loss in capacity

II Cylindrical Cell

A. Mechanical

1. Cell packaging is less conventional

2. Cell self containing - no restraints required

3. Thermal transport - 50 in^2 of surface

4. Fewer internal welds (14 vs 25 for prismatic cell)

5. Cell weight = 1155 grams

6. Fewer plate edges which act as a potential cutting edge (310 in^2 vs 670 in^2)

B. Electrochemical

1. Wider range of geometric plate ratio

2. Wider range of negative to positive ratio

3. Intrinsically lower operating pressure (due to coreless design)

C. Effect of Sterilization

1. Higher end-of-charge voltage (than prior to sterilization)

2. Negligible capacity loss

One of the basic differences between the behavior of the two designs is that the cylindrical cells do not exhibit any appreciable capacity loss after heat sterilization. Experimental data obtained while performing

the electrochemical investigations show that 4 Ah prismatic cells are negative limited during discharge after being subjected to a heat sterilization cycle. Other data indicate that a considerable quantity of oxygen gas is evolved during heat sterilization. It is hypothesized that this evolved oxygen reacts with the residual cadmium thus removing the "charge adjust" or free cadmium used to assure positive limitation during discharge. Since the cylindrical cell has a larger amount of free cadmium metal compared to the prismatic cell, which results from a larger negative to positive ratio (i.e. 1.65 vs 1.40), all the free cadmium metal is not consumed. Therefore, the cylindrical cell remains positive limited after sterilization. To increase the negative to positive ratio of the prismatic to these higher levels to allow for more free cadmium metal would require the use of more heavily loaded negative plates. Other studies show that cadmium plates loaded to the level necessary to attain this ratio do not perform well electrochemically. They exhibit lower oxygen recombination rates, a tendency to lose capacity and polarize such that charging voltages are higher and discharge voltages are lower than less heavily loaded plates.

Based on these considerations as well as those presented in Table II-3, the cylindrical cell design was selected for the interim as well as final design.

The interim cell design characteristics are shown in Table II-4

TABLE II-4

Design Characteristics, Interim Cell Design

25 Ampere - hour Heat Sterilizable Cylindrical Cells

Plates		
Number of positive		3
Number of Negative		4
Ratio (negative to positive formation capacity)		1.8
Separator	non-woven polypropylene	Pellon FT2140
Electrolyte		
Type		KOH
Concentration		30%
Quantity		90 cc
Weight		1155 gr
Seals		Glass to Metal

These cells were built to these parameters and tested for capacity. These test data are shown in Table II-5

The final design will include mechanical and procedual improvements determined during the manufacture of the interim design cells. The final design cells will also include ceramic-to-metal seals in place of the glass-to-metal seals previously used.

E. Long Range Testing Program

The long range testing program described on pages II-14 through II-17 in the Report for the Eighth Quarter began during this reporting period as outlined cell data was obtained daily during the initial stages of testing

TABLE II-5

PERFORMANCE DATA FOR INTERIM MODEL CELLS

Charging Conditions 3.0 Amperes for 16 hours
Discharging Conditions 10 Amperes to 1.00 volt cut off
Cycle Number 3

Cell No.	ECV (volt)	OCV (volt)	V @ 50% (volt)	ECR (mΩ)	ECP (psia)	ECC (Ah)
C250	1.435	1.389	1.263	5.6	32	32.88
C251	1.429	1.388	1.264	4.2	35	33.45
C252	1.427	1.386	1.262	4.4	33	32.78
C253	1.427	1.387	1.263	4.2	31	33.15
C254	1.422	1.382	1.263	3.9	29	33.03
C255	1.426	1.386	1.262	4.2	31	32.48
C256	1.423	1.383	1.263	3.8	32	32.60
C257	1.423	1.385	1.267	3.7	28	33.48
C258	1.437	1.389	1.258	6.6	28	33.23
C259	1.436	1.391	1.267	3.8	29	32.63
C260	1.438	1.394	1.270	3.8	32	32.65
C261	1.432	1.390	1.267	4.4	28	32.75
C262	1.437	1.392	1.264	4.0	30	33.33
C263	1.428	1.385	1.262	4.4	30	32.65
C264	1.424	1.381	1.263	3.8	15	32.15
C265	1.426	1.384	1.256	3.8	33	31.28
C266	1.427	1.385	1.265	3.6	31	32.30
C268	1.430	1.387	1.262	3.7	27	32.98
C269	1.437	1.391	1.261	4.0	15	32.60
C270	1.441	1.393	1.258	5.1	28	33.08
AVG.	1.430	1.387	1.263	4.2	30	32.56
STD. DEV.	0.006	0.003	0.003	0.7	5	0.49

and only periodically thereafter. The cycle test outline and corresponding cells are shown in the Appendix to Section II. To date all cells are cycling without any failure. Cycling data is shown in Figures II-C through Figure II-Y. There are some erratic results evident, however, these are analysed as test equipment problems which will be corrected. All data will be analysed when testing is completed using a factorial format.

F. High Energy Density Plate

There was a continued effort this reporting period to determine the plaque design parameters which effect the charge rate and discharge rate sensitivity and strength of high energy density plate. Specifically under study are the effects of porosity and pore size distribution of plates of thickness 0.035 inches to 0.045 inches .

A factorial experiment was designed to specifically measure the effect of plaques porosity, pore ratio*, electrolyte quantity and duty cycle. The plaques prepared to date have been catagorized based on porosity and pore rates. These data are shown in Table II-6. The planned factorial test outline is shown in Table II-7. Testing has begun and complete results will be presented the next reporting period.

---

* ratio = $\frac{\text{pure volume of } 10\,\mu \text{ to } 15\,\mu \text{ size pores}}{\text{pure volume of } 15\,\mu \text{ to } 20\,\mu \text{ size pores}}$

pores as determine using mercury porosimeter techniques.

TABLE II-6

PLAQUE SAMPLES PREPARED TO DATE

Factor Code		Grouping No.	Plaque Lot No.	Thickness (inches)	Porosity (%)	Ratio
Porosity	Ratio					
High	High	I	17-901-1	.0264	84.0	2.59
			17-901-3	.0345	83.6	2.89
			17-901-4	.0405	83.3	3.40
			17-901-7	.0433	83.1	3.16
			16-902-2	.0402	84.0	3.18
			16-902-4	.0490	82.4	6.12
Low	High	II	17-901-4B	.0485	81.6	6.34
			18-902-7	.0299	80.7	2.43
			18-902-9	.0368	80.7	3.20
			19-902-15	.0433	78.4	2.40
High	Low	III	17-901-2	.0301	83.6	2.08
			16-901-1	.0266	85.3	2.06
			16-901-2	.0307	84.5	2.38
			16-902-1	.0351	84.6	2.18
Low	Low	IV	18-902-6	.0268	81.5	2.16
			18-902-8	.0340	81.2	2.17
			19-902-10	.0250	79.6	1.93
			19-902-11	.0295	79.6	1.71
			19-902-12	.0320	79.2	2.29
			19-902-13	.0362	79.2	2.19
			19-902-14	.0398	78.9	2.38
				Median	82.4	2.40

TABLE II-7

HIGH ENERGY DENSITY PLATE
FACTORIAL EXPERIMENT OUTLINE

INDEPENDENT VARIABLES

TEST SEQUENCE I

Factor Ident.	Independent Variables	Levels 0	1
A	Porosity	78.9 - 80.7%	83.1 - 84.6%
B	Ratio	2.19 - 2.38	3.16 - 3.20
C	Electrolyte Fill Level	60%	70%

TEST SEQUENCE II

A & B	As above		
C	Electrolyte Fill Level	60%	80%

TEST SEQUENCE III

A & B	As above		
C	Electrolyte Fill Level	70%	80%

APPENDIX TO

SECTION II

CYCLING TEST STATUS CHARTS

TABLE II-8

LONG RANGE CYCLE TESTING OUTLINE

Charge Rate	Cell Type	Temperature					
		30°F		50°F		70°F	
		Depth of Discharge		Depth of Discharge		Depth of Discharge	
		70%	80%	70%	80%	70%	80%
C/10	Cyl Prism	C-24 P-24	C-23 P-23	C-25 P-20	C-15 P-19	C-12 P-12	C-21 P-13
C/20	Cyl Prism	C-27 P-27	C-28 P-25	C-26 P-21	C-13 P-22	C-10 P-10	C-11 P-11

TABLE II-9

LONG RANGE CYCLE TEST - CELL LISTING (Numerical order)

Cell No.	Cell Type	Test Conditions		
		Temp. (°F)	Depth of Discharge (%)	Charge Rate
C-10	Cyl.	70	70	C/20
C-11	Cyl.	70	80	C/20
C-12	Cyl.	70	70	C/10
C-13	Cyl.	50	80	C/20
C-15	Cyl.	50	80	C/10
C-21	Cyl.	70	80	C/10
C-23	Cyl.	30	80	C/10
C-24	Cyl.	30	70	C/10
C-25	Cyl.	50	70	C/10
C-26	Cyl.	50	70	C/20
C-27	Cyl.	30	70	C/20
C-28	Cyl.	30	80	C/20
P-10	Prism	70	70	C/20
P-11	Prism	70	80	C/20
P-12	Prism	70	70	C/10
P-13	Prism	70	80	C/10
P-19	Prism	50	80	C/10
P-20	Prism	50	70	C/10
P-21	Prism	50	70	C/20
P-22	Prism	50	80	C/20
P-23	Prism	30	80	C/10
P-24	Prism	30	70	C/10
P-25	Prism	30	80	C/20
P-27	Prism	30	70	C/20

Figure II-C

Test Conditions

Temp.	70°F
DOD	70%
CHG Rate	C/20
Cell Type	Prism
Cell No.	P-10

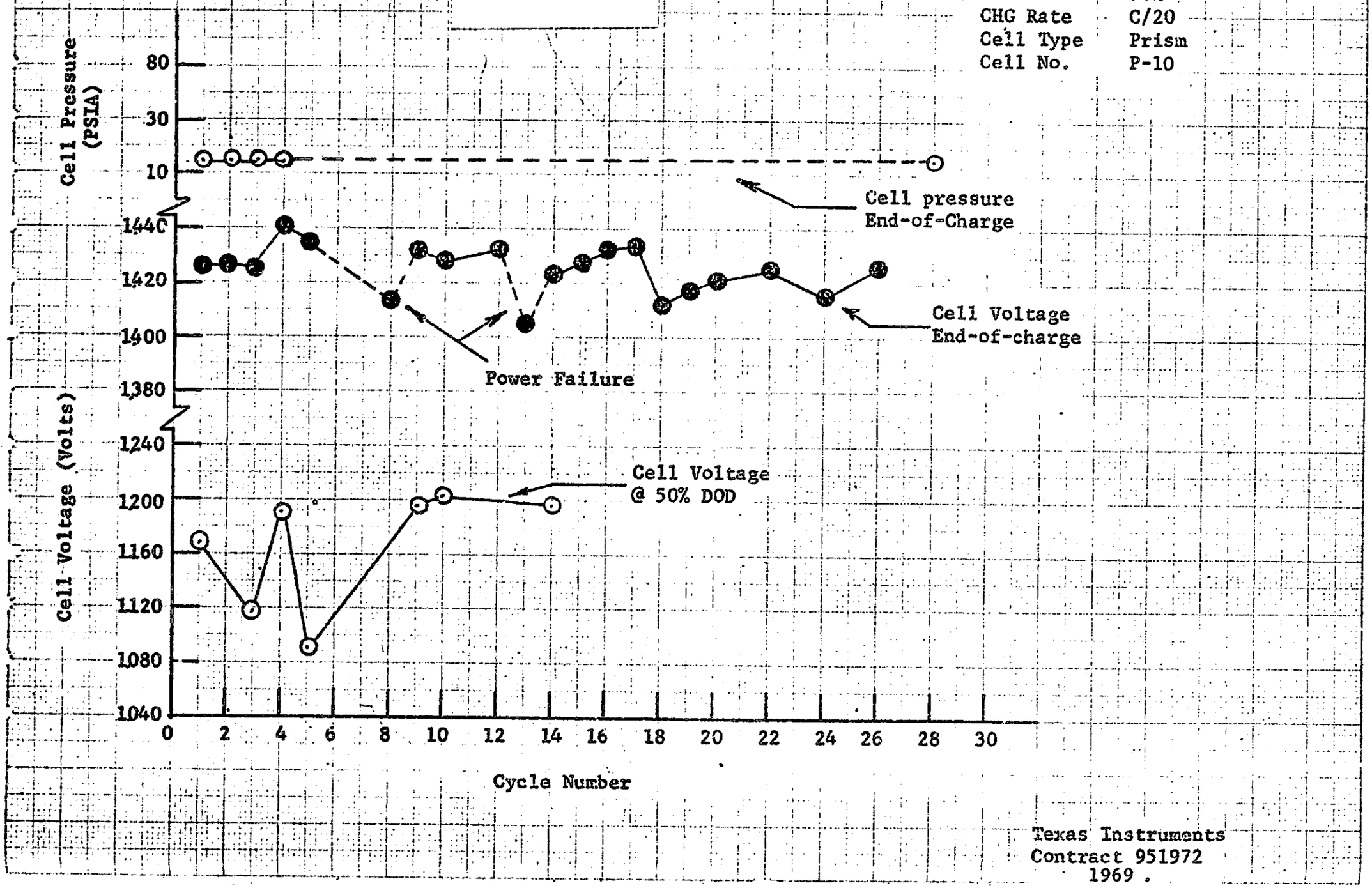

Texas Instruments
Contract 951972
1969 .

Figure II-D

Test Conditions

Temp.	70°F
DOD	80%
Chg Rate	C/20
Cell Type	Prism
Cell No.	P-11

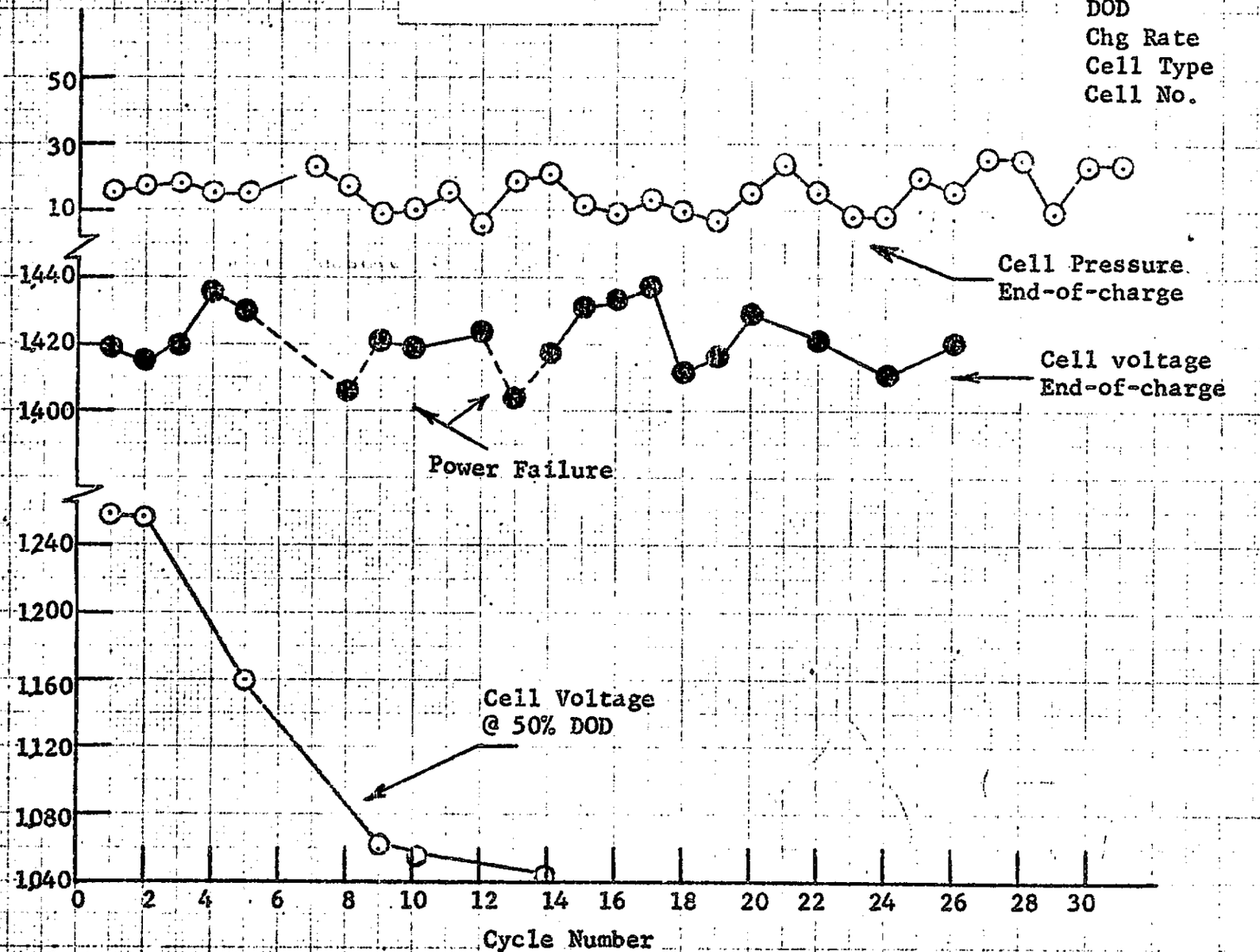

Texas Instruments
Contract 951972
1969

Figure II-E

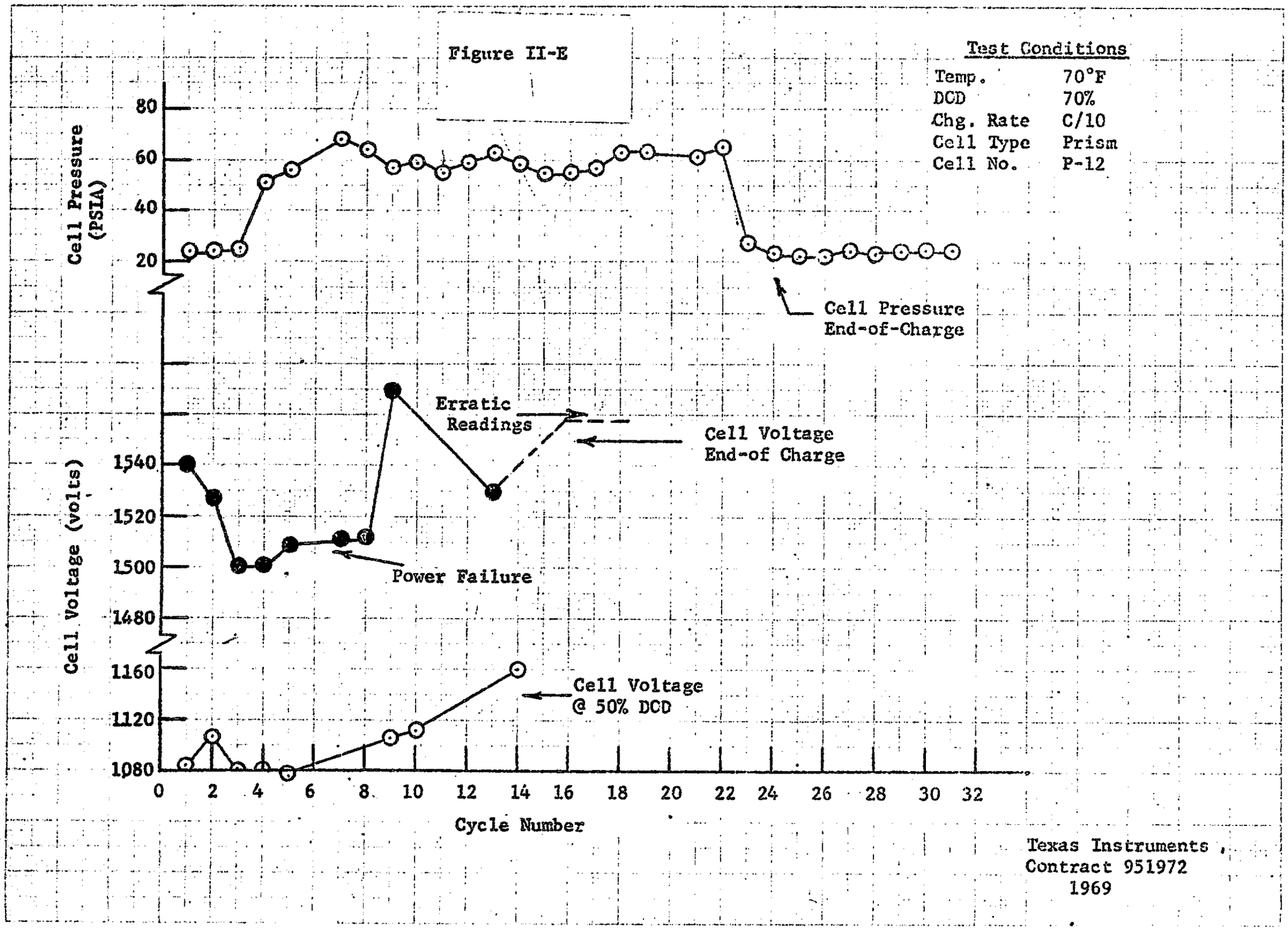

Texas Instruments,
Contract 951972
1969

Figure II-F

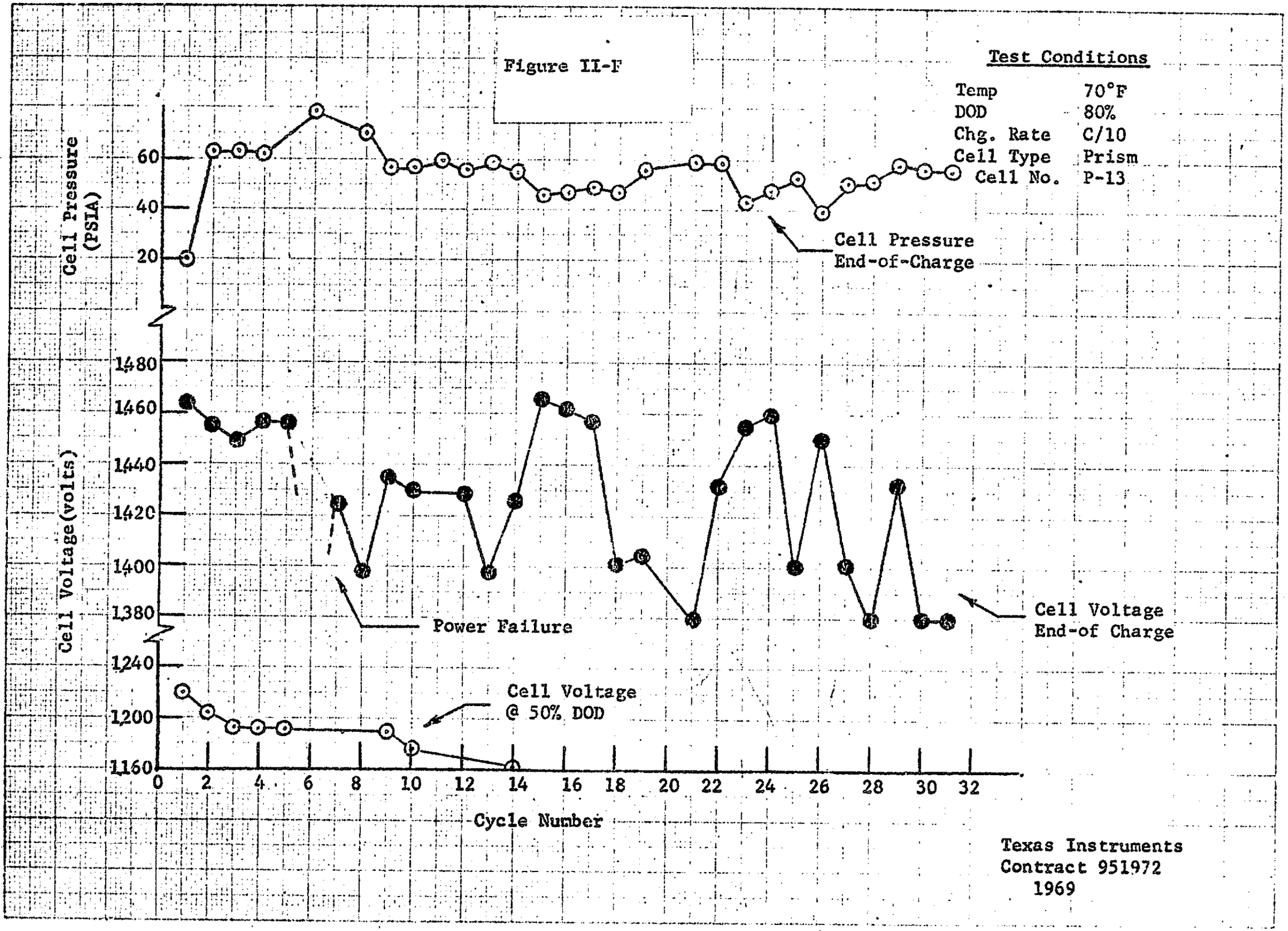

Texas Instruments
Contract 951972
1969

Figure II-G

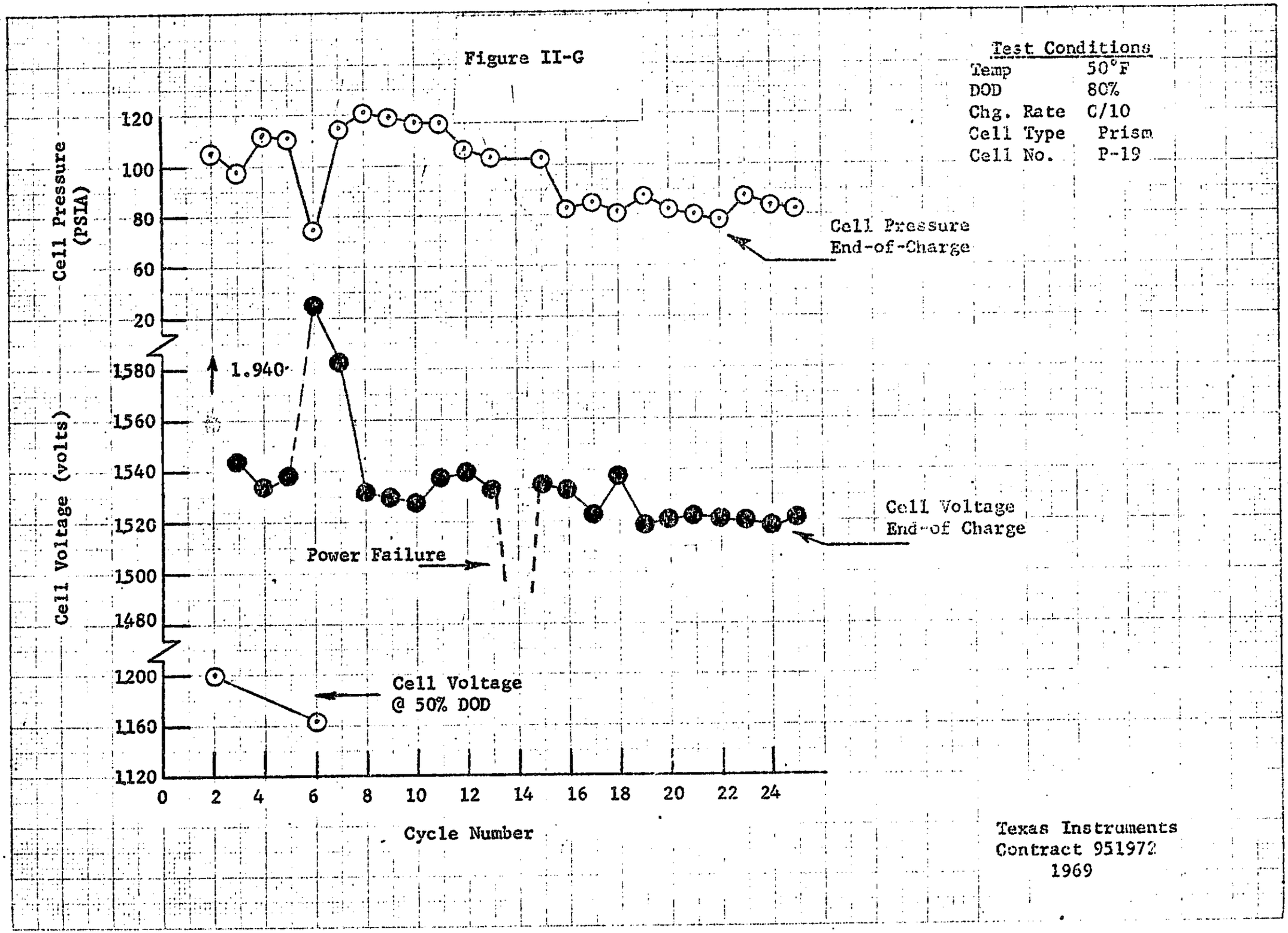
Test Conditions
Temp 50°F
DOD 80%
Chg. Rate C/10
Cell Type Prism
Cell No. P-19
Cell Pressure (PSIA)
120
100
80
60
20
Cell Pressure End-of-Charge
Cell Voltage (volts)
1580
1560
1540
1520
1500
1480
1200
1160
1120
1.940
Power Failure
Cell Voltage End-of Charge
Cell Voltage @ 50% DOD
0 2 4 6 8 10 12 14 16 18 20 22 24
Cycle Number
Texas Instruments
Contract 951972
1969

Figure II-H

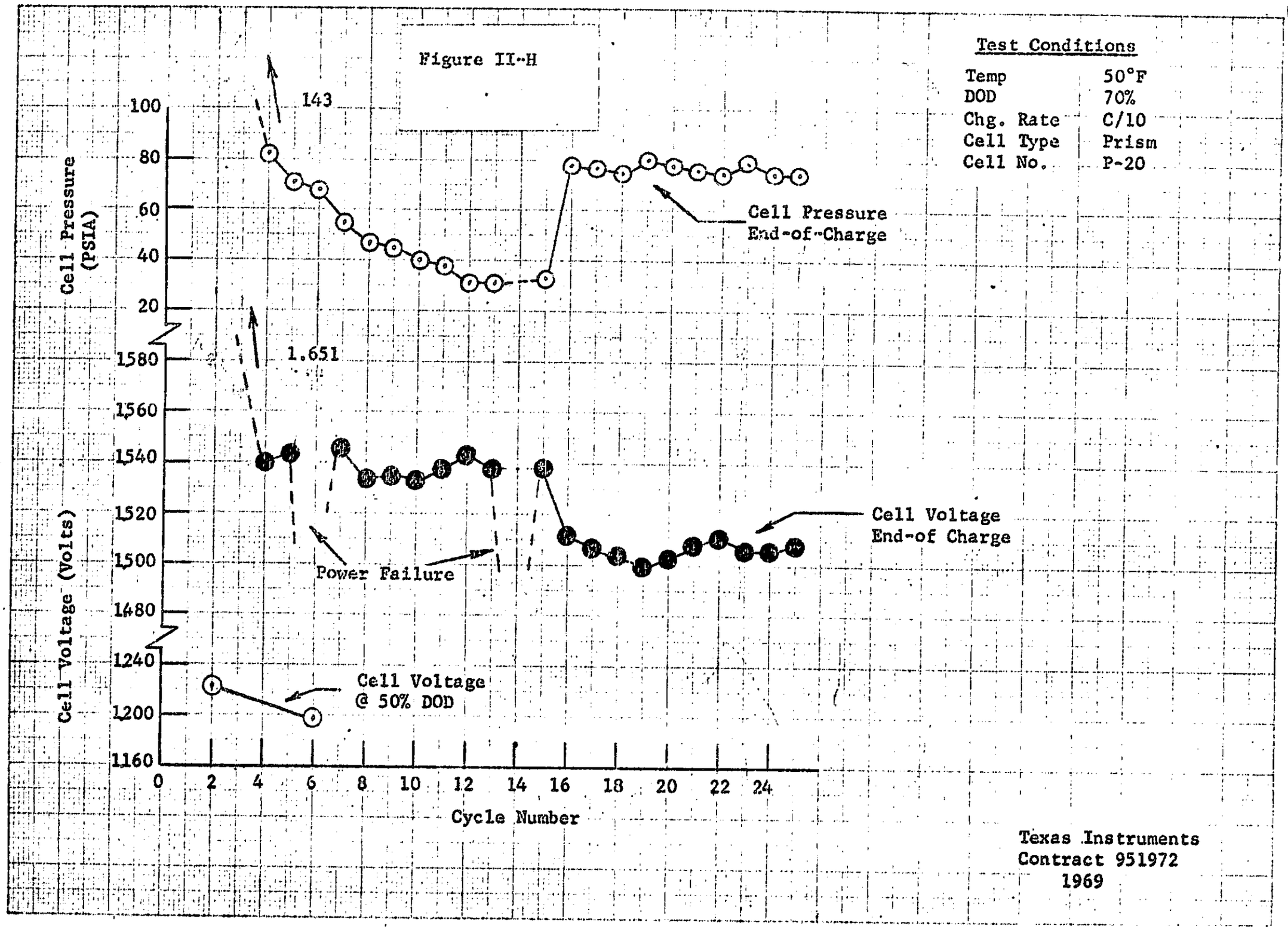
Test Conditions
Temp 50°F
DOD 70%
Chg. Rate C/10
Cell Type Prism
Cell No. P-20
Cell Pressure (PSIA)
100
80
60
40
20
1580
1560
1540
1520
1500
1480
1240
1200
1160
143
1.651
Cell Pressure End-of-Charge
Power Failure
Cell Voltage End-of Charge
Cell Voltage @ 50% DOD
Cell Voltage (Volts)
0 2 4 6 8 10 12 14 16 18 20 22 24
Cycle Number
Texas Instruments
Contract 951972
1969

Figure II-I

Test Conditions

Temp	50°F
DOD	70%
Chg. Rate	C/20
Cell Type	Prism
Cell No.	P-21

1.725 volts

1939 volts

Cell Voltage End-of Charge

Cell Voltage End-of Charge

Power Failure

Cell Voltage @ 50% DOD

Cell Pressure (PSIA)

100
80
60
40

Cell Voltage (Volts)

1600
1580
1560
1540
1520
1500
1200
1160
1120

0 2 4 6 8 10 12 14 16 18 20 22 24 26

Cycle Number

Texas Instruments
Contract 951972
1969

Figure II-J

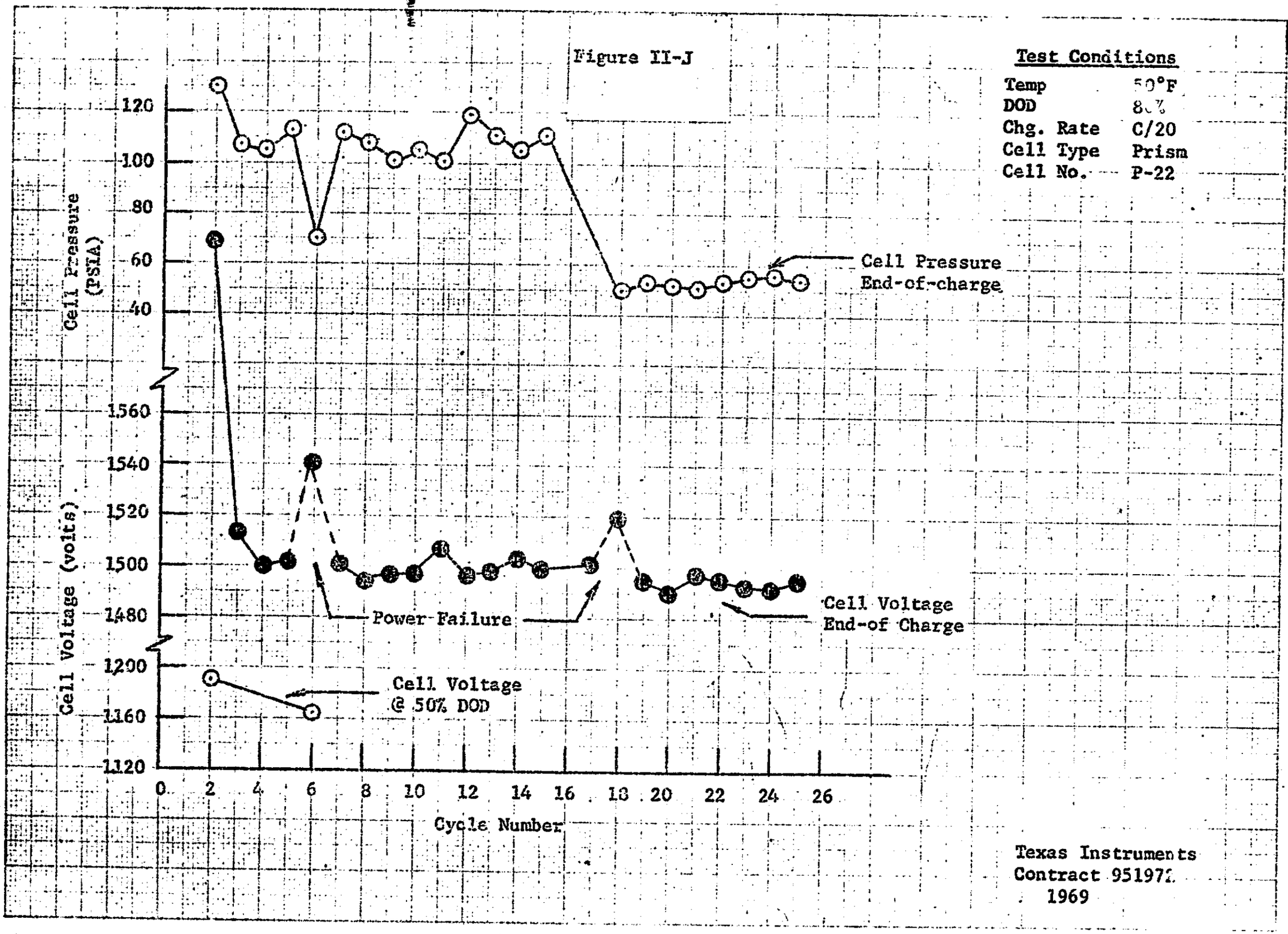

Texas Instruments
Contract 951972
1969

Figure II-K

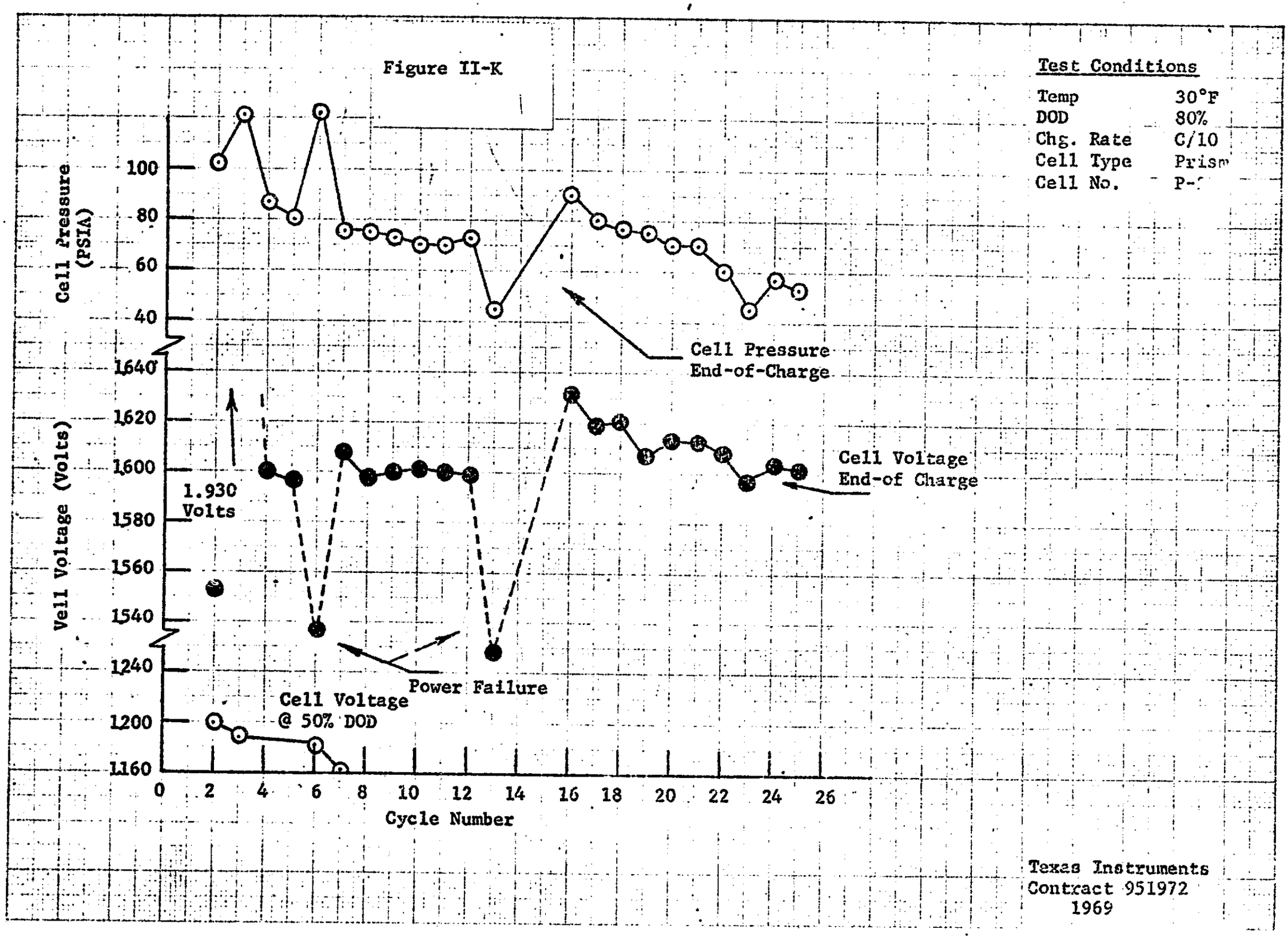

Texas Instruments
Contract 951972
1969

Figure II-L

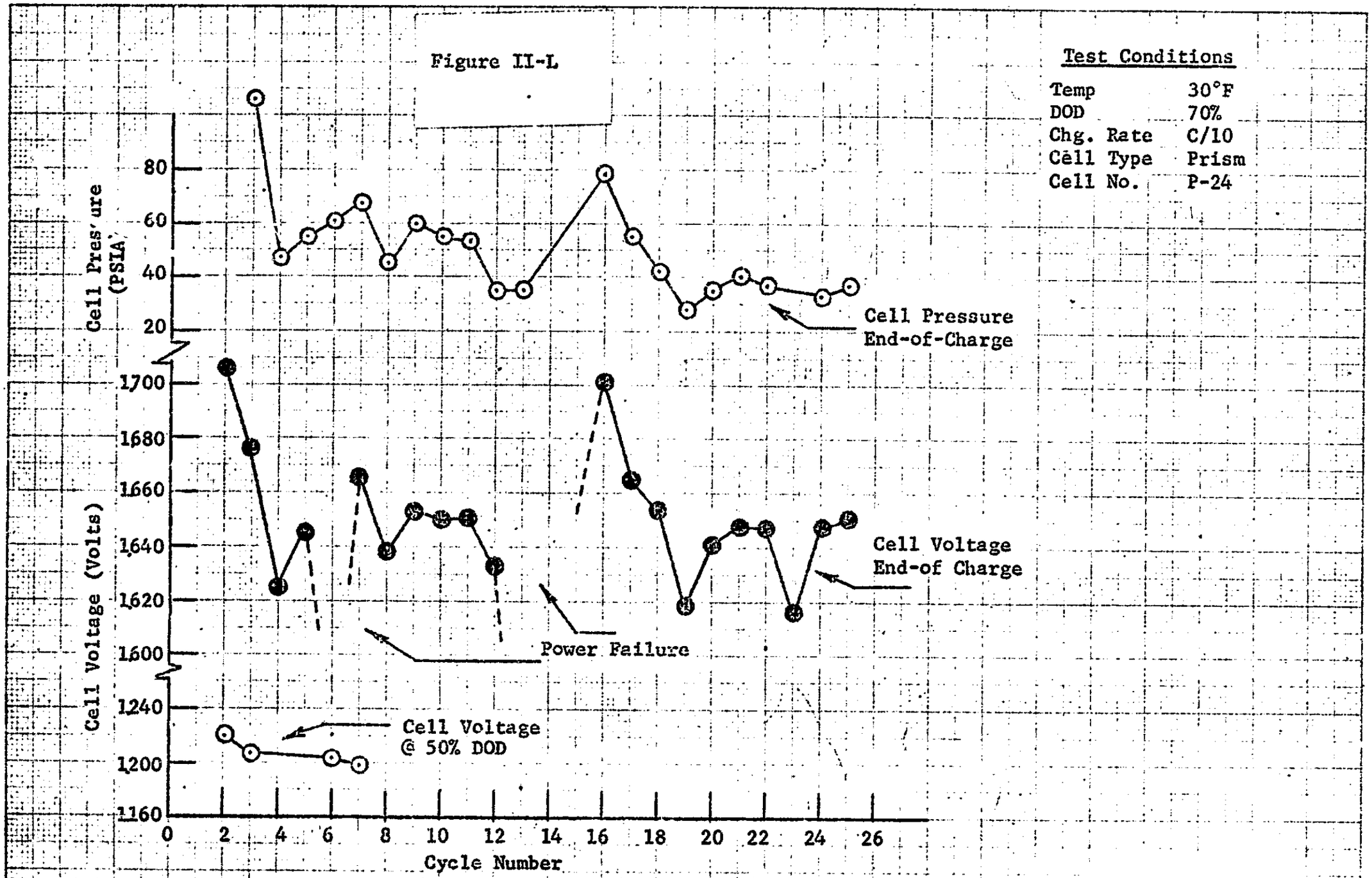

Texas Instruments
Contract 951972
1969

Figure II-M

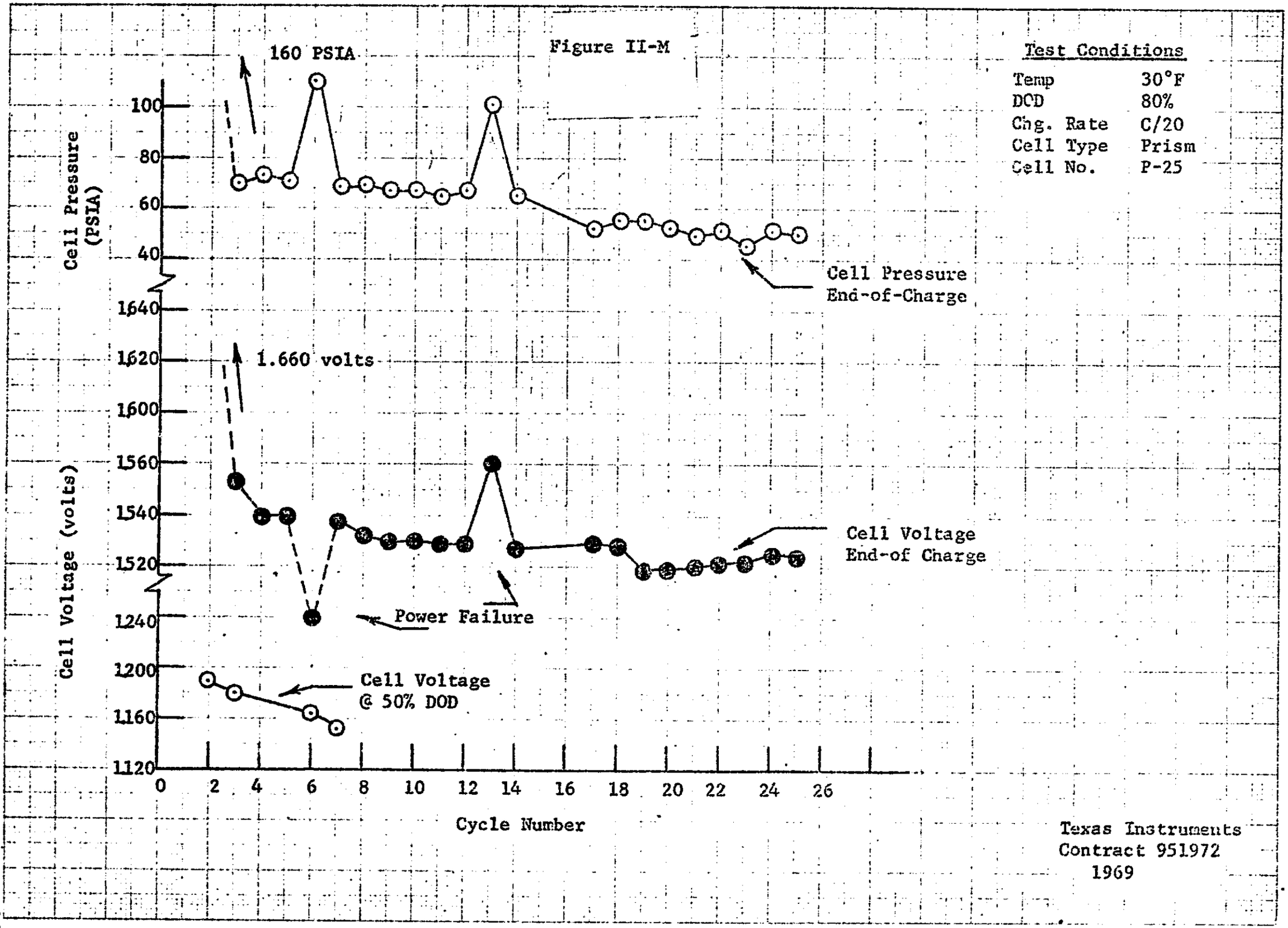

Texas Instruments
Contract 951972
1969

Figure II-N

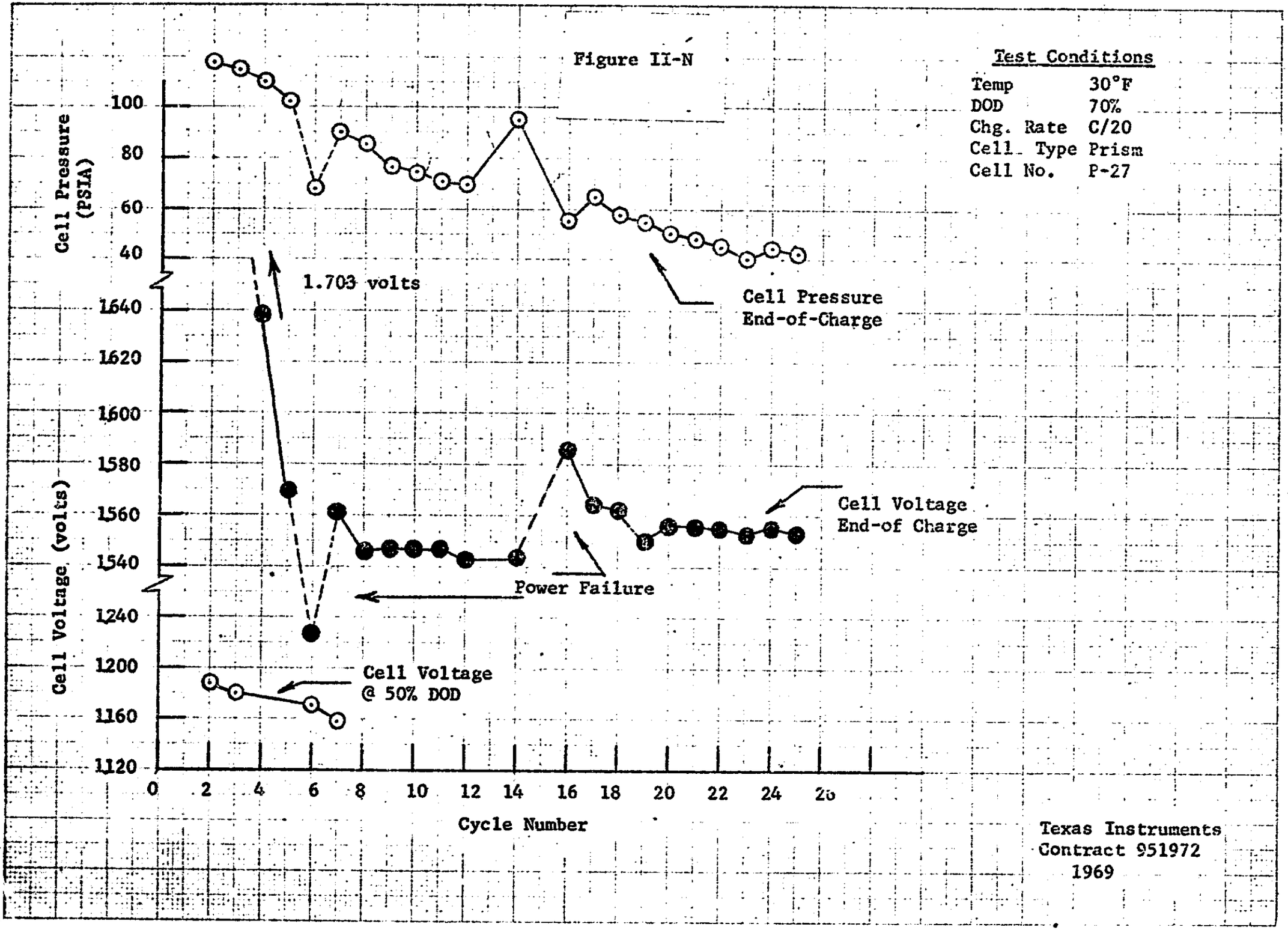

62-II

Figure II-0

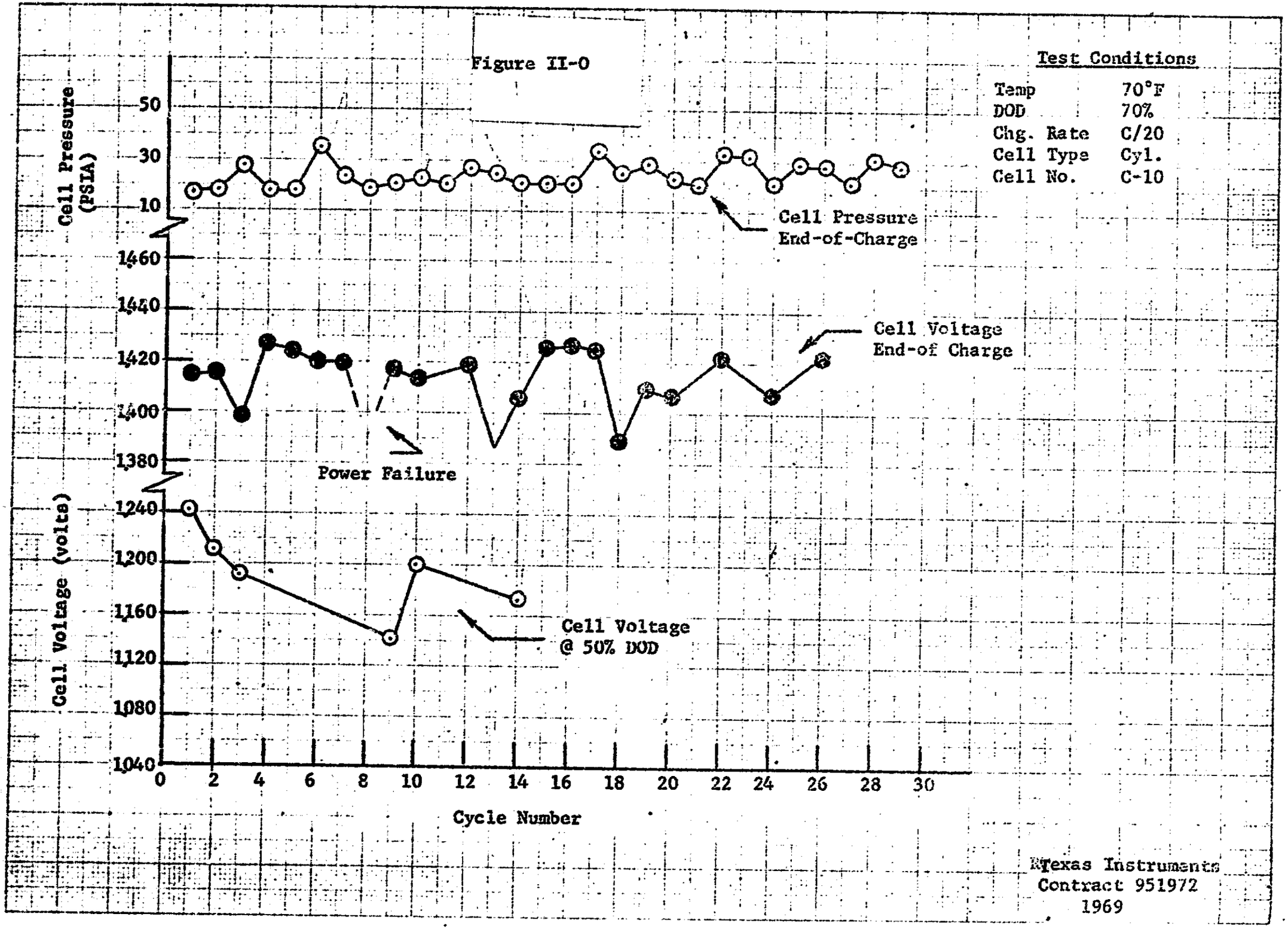

Texas Instruments
Contract 951972
1969

Figure II-P

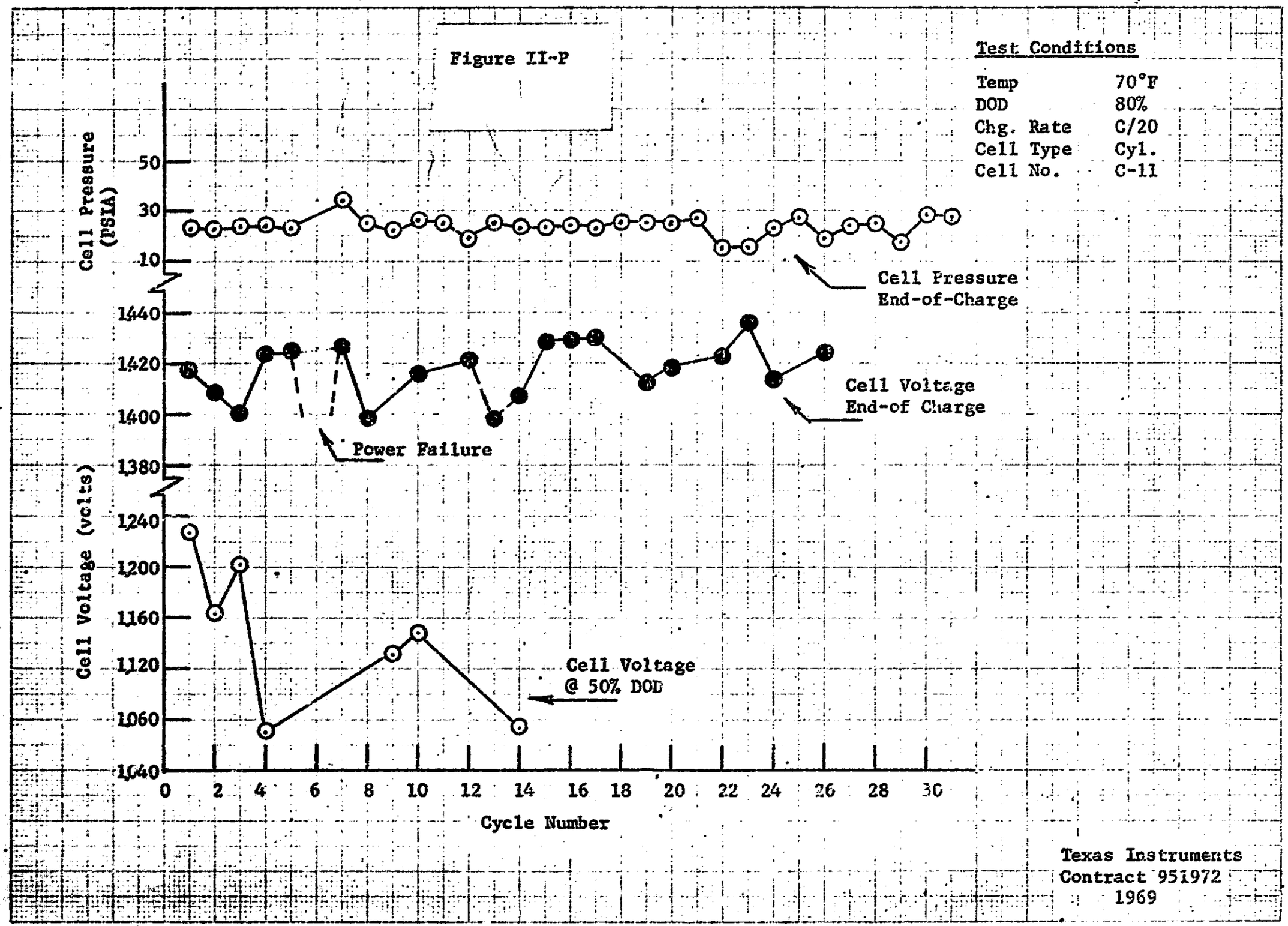

Texas Instruments
Contract 951972
1969

II-31

Figure II-Q

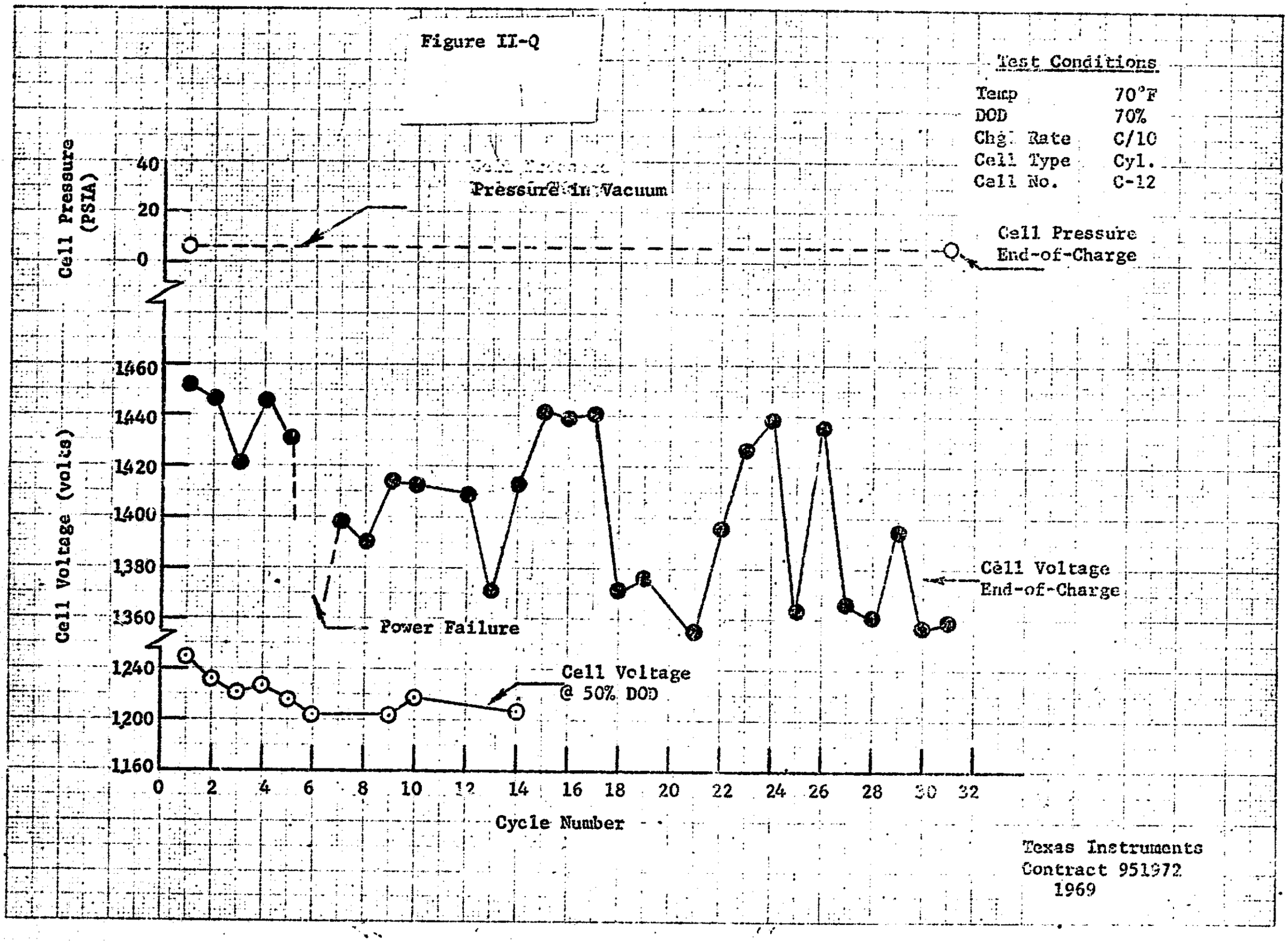

Texas Instruments
Contract 951972
1969

Figure II-R

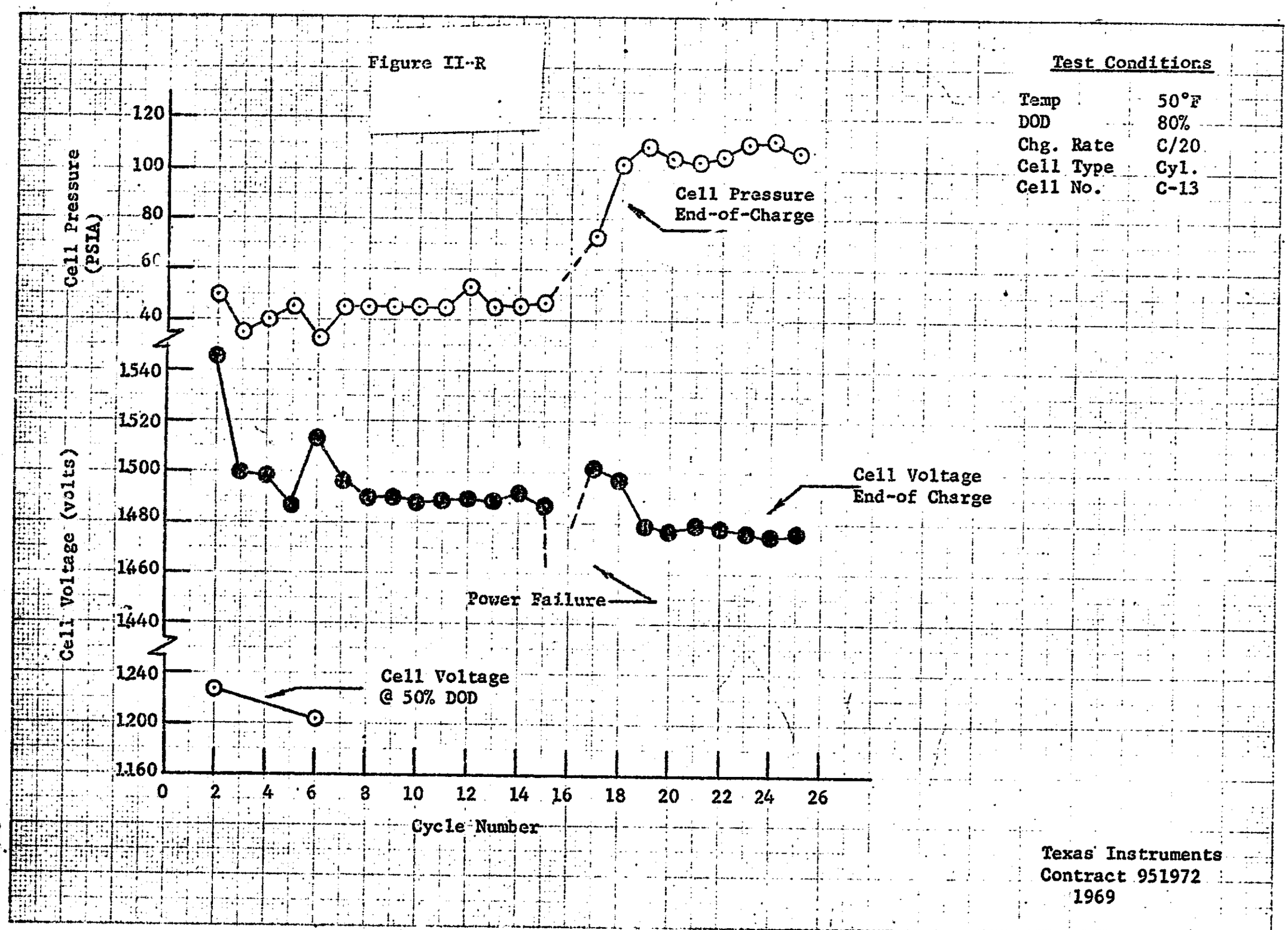

Texas Instruments
Contract 951972
1969

Figure II-S

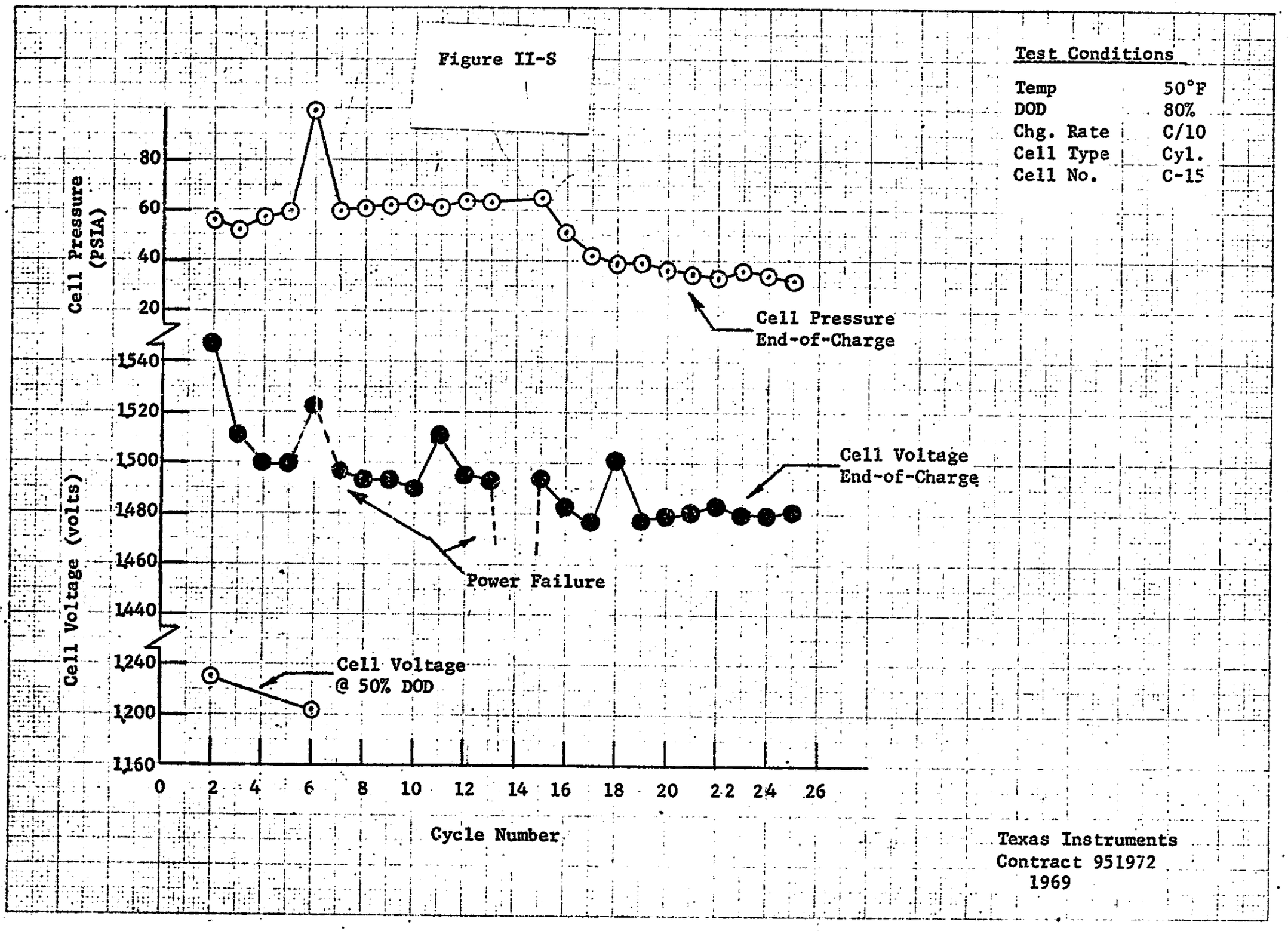
Test Conditions
Temp 50°F
DOD 80%
Chg. Rate C/10
Cell Type Cyl.
Cell No. C-15
Cell Pressure (PSIA)
80
60
40
20
1540
1520
1500
1480
1460
1440
1240
1200
1160
Cell Pressure End-of-Charge
Cell Voltage End-of-Charge
Power Failure
Cell Voltage @ 50% DOD
Cell Voltage (volts)
0 2 4 6 8 10 12 14 16 18 20 22 24 26
Cycle Number
Texas Instruments
Contract 951972
1969

Figure II-T

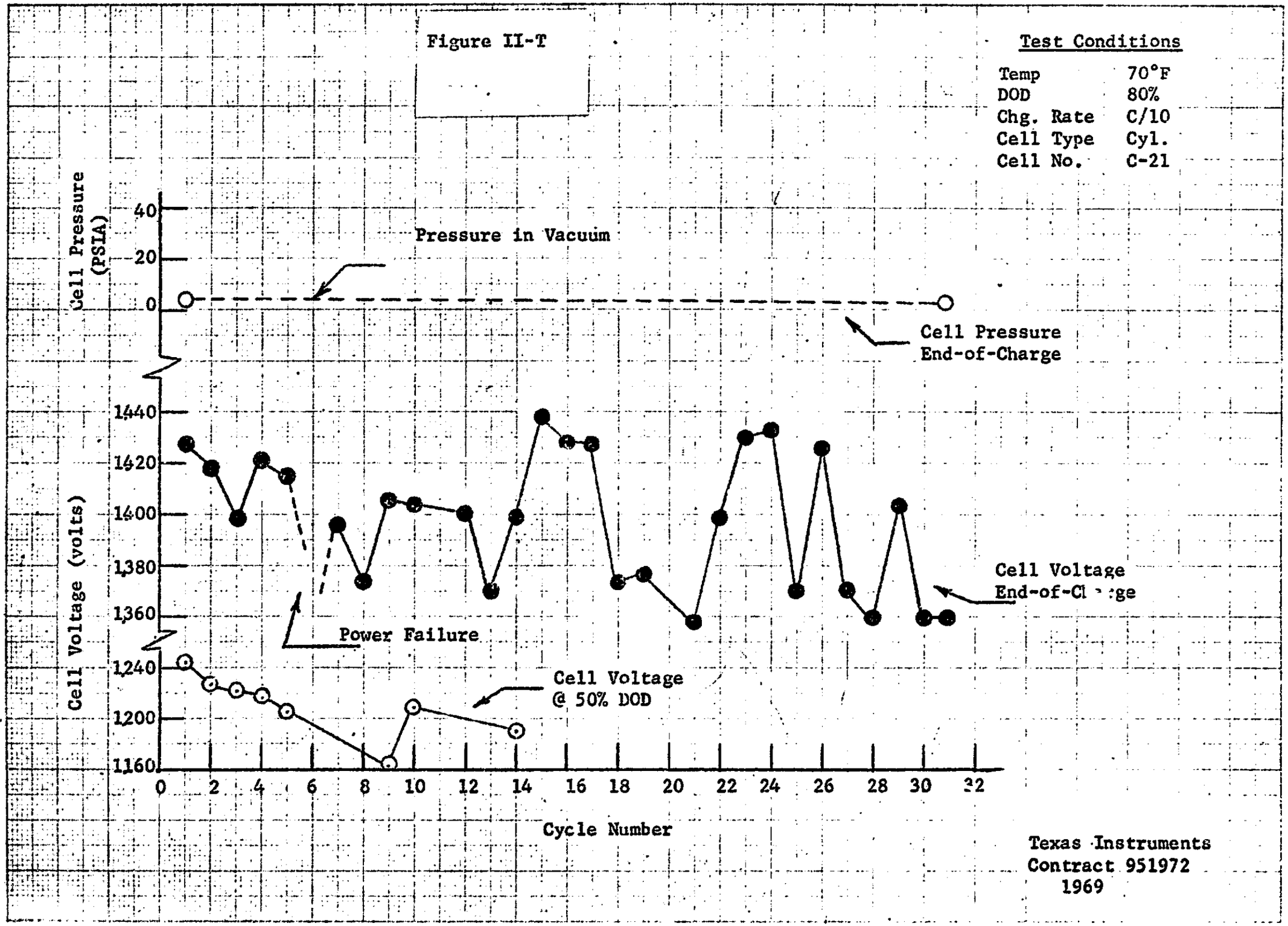
Test Conditions
Temp 70°F
DOD 80%
Chg. Rate C/10
Cell Type Cyl.
Cell No. C-21
Cell Pressure (PSIA)
40
20
0
Pressure in Vacuum
Cell Pressure End-of-Charge
1440
1420
1400
1380
1360
1240
1200
1160
Cell Voltage (volts)
Power Failure
Cell Voltage @ 50% DOD
Cell Voltage End-of-Charge
0 2 4 6 8 10 12 14 16 18 20 22 24 26 28 30 32
Cycle Number
Texas Instruments
Contract 951972
1969

Figure II-U

Test Conditions

Temp	30°F
DOD	80%
Chg. Rate	C/10
Cell Type	Cyl.
Cell No.	G-23

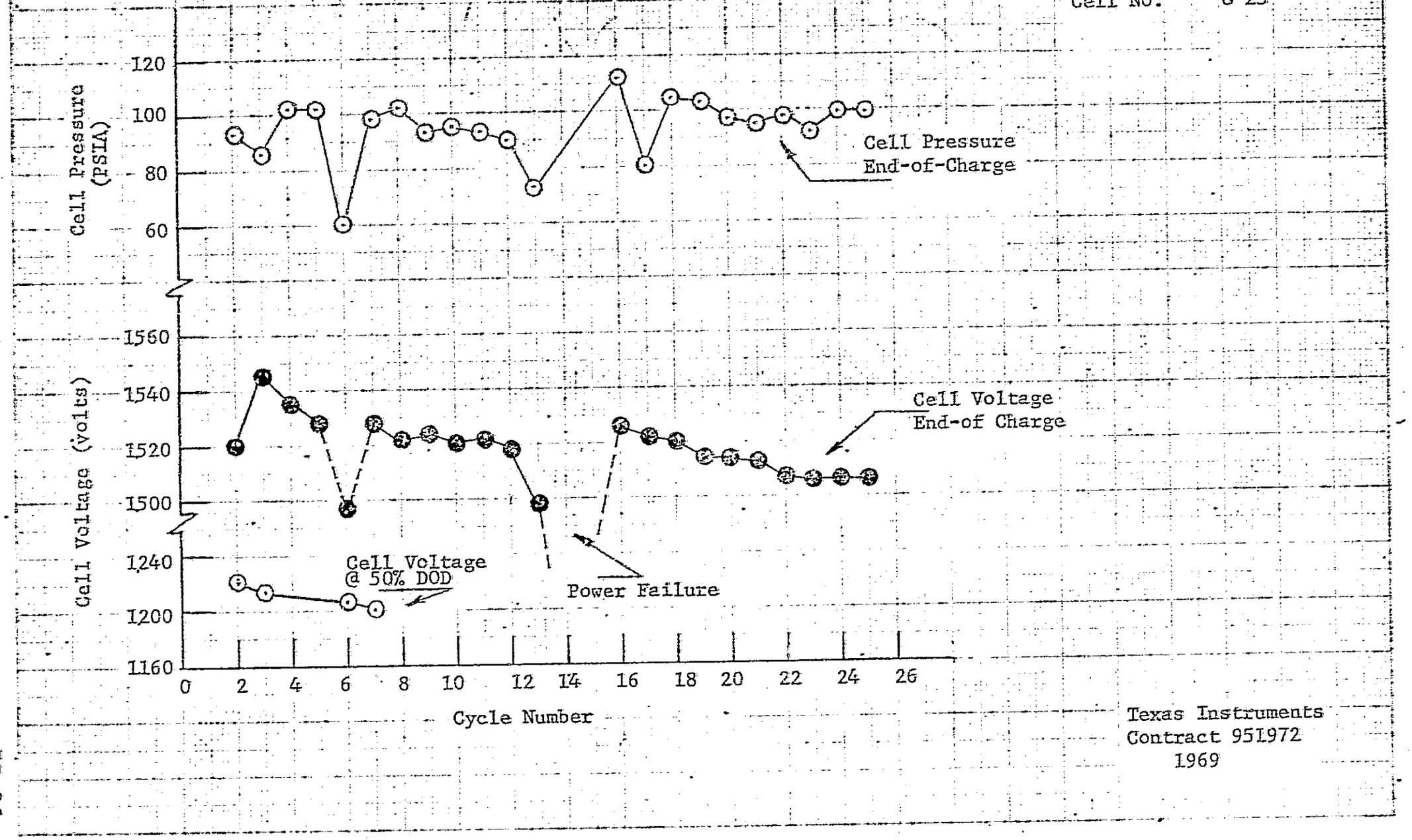

Texas Instruments
Contract 951972
1969

Figure II-V

Test Conditions

Temp	30°F
DOD	70%
Chg. Rate	C/10
Cell Type	Cyl.
Cell No.	C-24

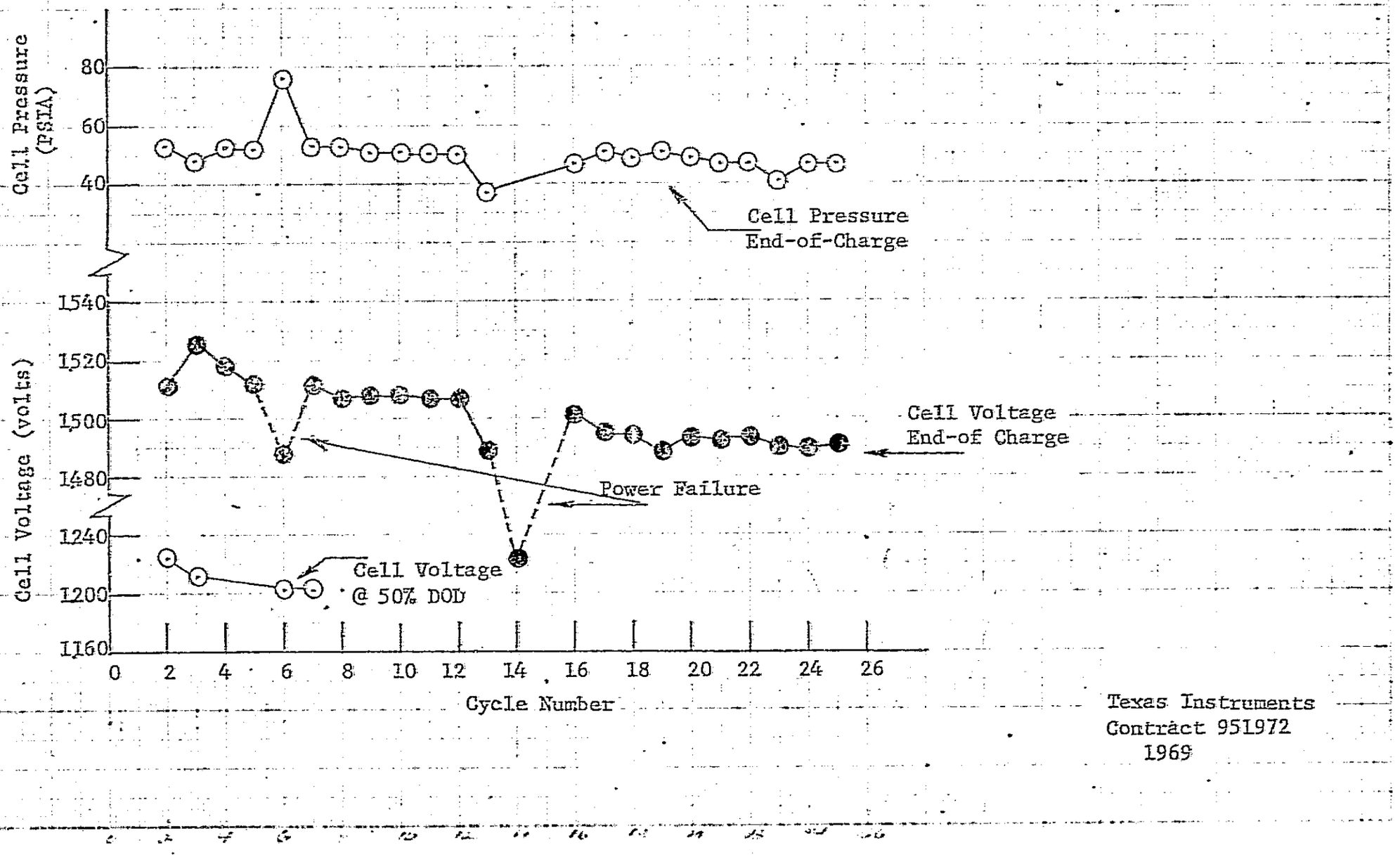

Texas Instruments
Contract 951972
1969

Figure II-W

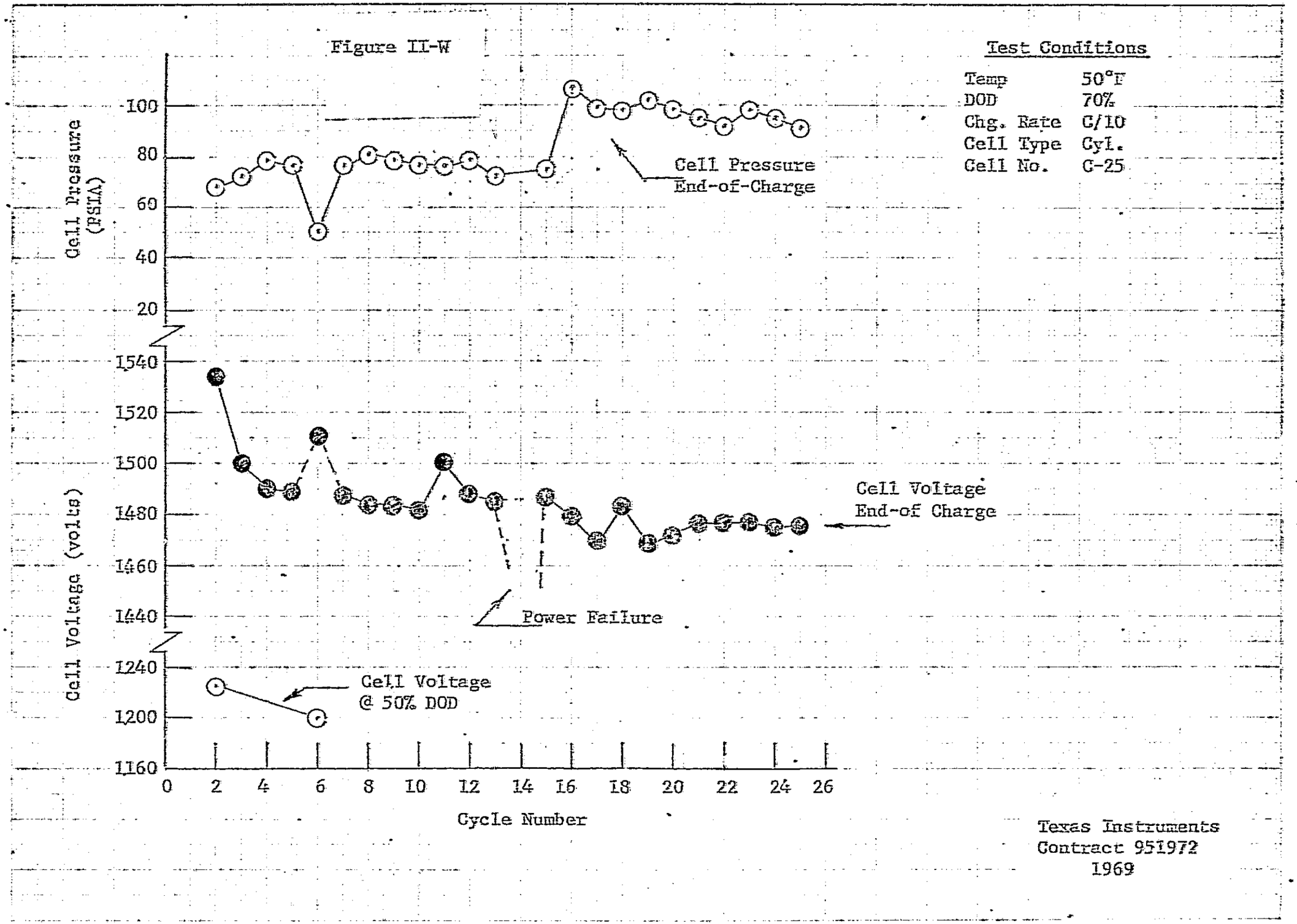

Texas Instruments
Contract 951972
1969

Figure II-X

Test Conditions

Temp	50°F
DOD	70%
Chg. Rate	C/20
Cell Type	Cyl.
Cell No.	C-26

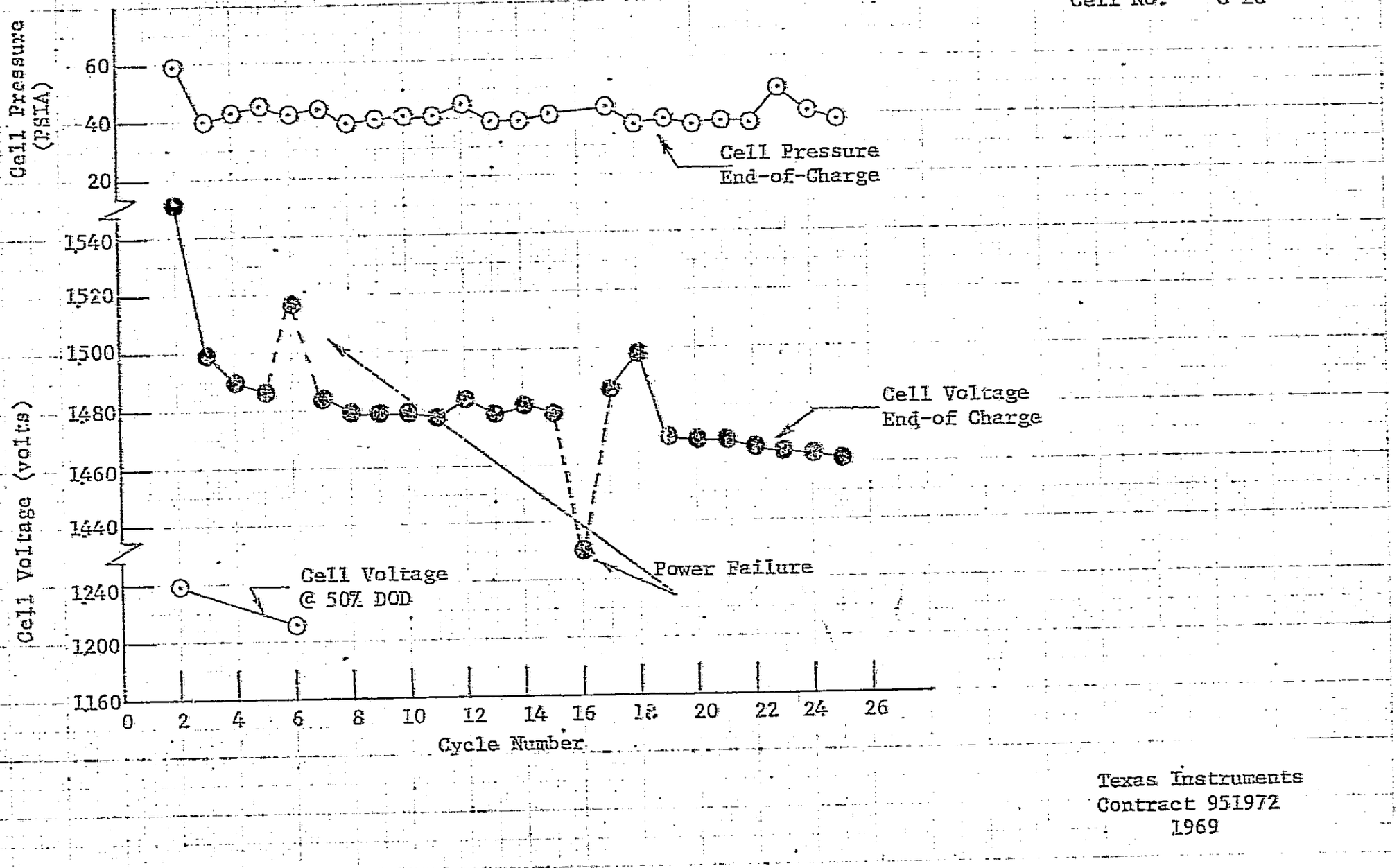

Texas Instruments
Contract 951972
1969

Figure II-Y

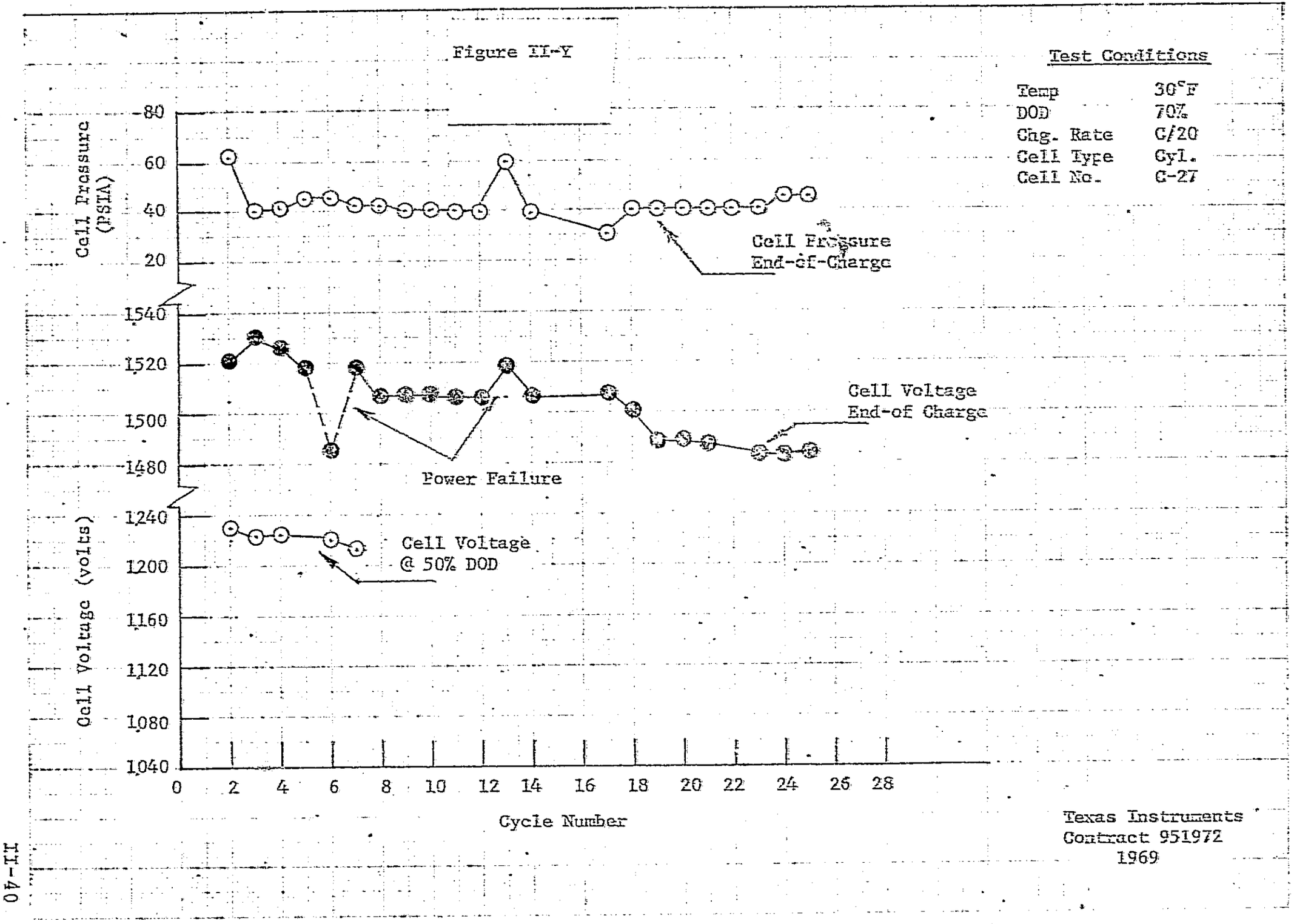

Texas Instruments
Contract 951972
1969

Figure II-Z

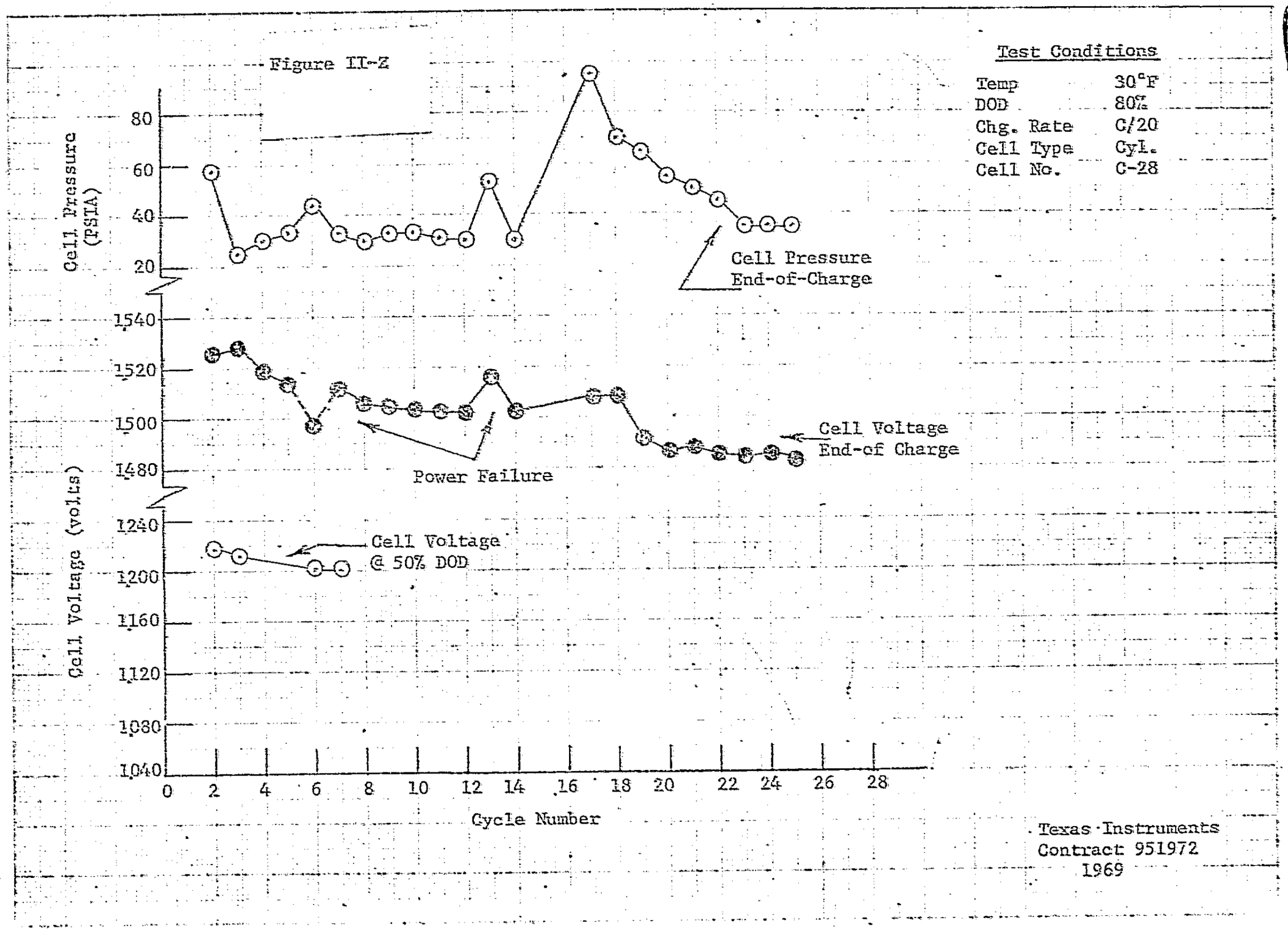
Test Conditions
Temp 30°F
DOD 80%
Chg. Rate C/20
Cell Type Cyl.
Cell No. C-28
Cell Pressure (PSIA)
80
60
40
20
Cell Pressure End-of-Charge
1540
1520
1500
1480
Cell Voltage End-of Charge
Power Failure
Cell Voltage (volts)
1240
1200
1160
1120
1080
1040
Cell Voltage @ 50% DOD
0 2 4 6 8 10 12 14 16 18 20 22 24 26 28
Cycle Number
Texas Instruments
Contract 951972
1969

III. IMPACT TESTING OF CELLS AND COMPONENTS

SECTION III -- IMPACT TESTING

TABLE OF CONTENTS

- Cont'd. -

SECTION III -- IMPACT TESTING

TABLE OF CONTENTS -- (CONT'D.)

SECTION III -- IMPACT TESTING

LIST OF FIGURES

- Cont'd. -

SECTION III -- IMPACT TESTING

LIST OF FIGURES -- CONT'D.

SECTION III -- IMPACT TESTING

LIST OF TABLES

A. Development of Impact Testing Facility

(a) Study of Acceleration Characteristics:

During the impact testing of large Ni-Cd cells, we observed failure occuring before impact as shown by our monitor of cell voltage in some instances. This was primarily due to their lack of impact-resistant design, however, it prompted us to investigate the nature of our acceleration impulse in detail. The accelerometer mounted on the carriage was used with a trigger system which allowed the signal to be displayed throughout carriage travel. Figure III-1(a) illustrates the overall acceleration - time history of our system. The acceleration portion has been expanded in Fig. III-1(b) to describe in detail the impulse typically experienced at nearly maximum test velocity and carriage weight. We observe four discrete impulses responsible for creating this change in velocity. The maximum acceleration is an initial 1400 g peak. The rise times appear to be low and a vibration frequency of approximately 1150 cy/sec can be observed throughout the trace which illustrates the first mode of the square back plate of the carriage. A final observation was the role of the rubber stopper which is ordinarily used to "cushion" the force coupling between ram and carriage. Under the high rates of loading encountered, this element serves only to allow time for ram velocity buildup. A lower acceleration input to the carriage can be achieved by use of a more rigid force distributing element between the ram and carriage.

(b) Accelerometer Comparison and Carriage Behavior:

Following the installation of the larger conical carriage main plate the lower frequency vibrations were eliminated. However, a higher frequency disturbance persisted and somewhat resembled an excitation of the transducer

FIG. III-1

ACCELERATION - TIME

(a)

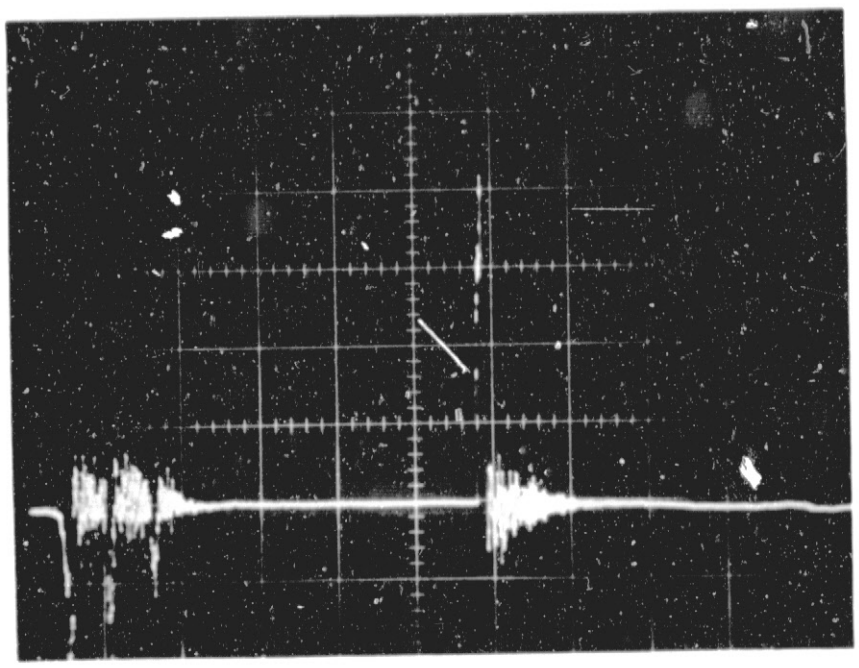

1000 g/cm

10 msec/cm

103 ft/sec

(2R)

1 1/4" DIA.

ACCEL IMPULSE

UNIFORM VELOCITY

IMPACT DECELERATION

16 msec

(b)

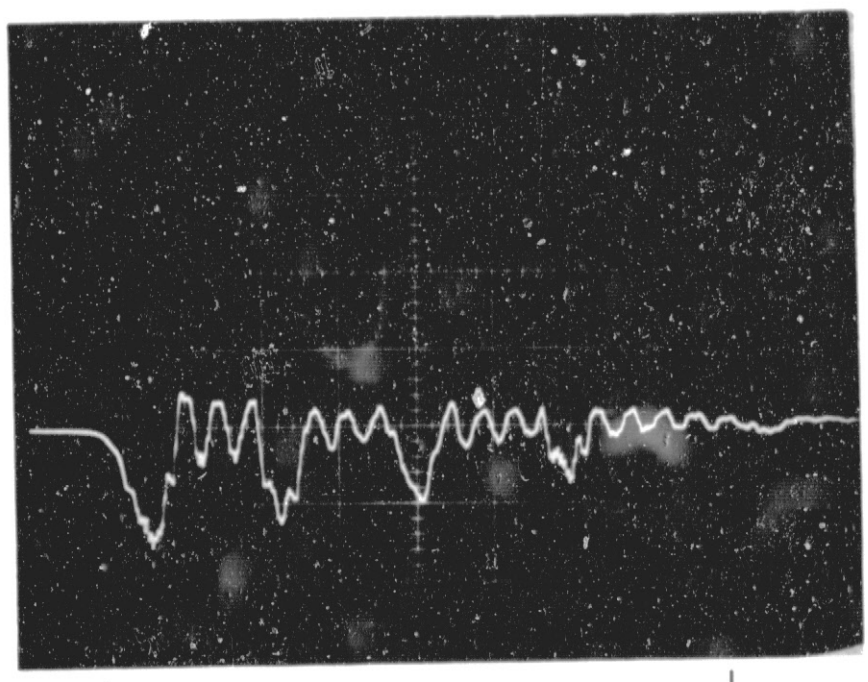

1000 g/cm

2 msec/cm

115 ft/sec

(1R)

1 1/2" DIA.

CARRIAGE ACCELERATION

16 msec

resonance. Two accelerometers were used to investigate: Kistler 808A-41.5 K HZ and Kistler 805A - 62.5 K HZ. Both traces obtained indicated a disturbance at 24-26 K HZ and thus eliminated transducer resonance as the source. We calculated the speed of one-dimensional stress wave propagation within the 9" long back plate support struts and found it to be approximately 45 μ sec which would imply a frequency of 22 K HZ. We are quite certain that this is the source of the high frequency disturbance. Since it is much higher than the fundamental and lower harmonics of interest, little difficulty has been experienced by employing filtration. However, the best solution would be to design an accelerator yoke extension as a permanent part of the ram. A third rail would be placed on the rail bed beneath the carriage for pitch guidance. Removal of this acceleration structure from the carriage would not only eliminate the disturbance during impact but the vibration during acceleration would also be eliminated. Alternatively, groove extension wings might be an integral part of the carriage if a third rail was not practical. The possibility also exists that a guide-rod, spring and damper could be used at the end of each strut and tuned for minimum transmissibility at the disturbing frequency.

(c) High Speed Photographic analysis:

Films of the overall system performance were taken in preparation for photographic study of test elements within the carriage during impact. High-speed 16 mm photography with a Fastax camera running at 7000 frames per second provided us with information concerning the acceleration phase and the lead wire motion during impact. More importantly we could now measure the

rebound velocity encountered relative to the impact velocity. This had been of some concern with the use of the heavier carriage and much larger tool diameters since the calculated g-levels were higher than those measured and the pulse length (penetration) had been shortened. The detailed observation of the Cu deformation indicated that the same shape could not be used throughout the range of 3/8"-1 1/2" tool diameters. Thickness of the target block should probably be raised at the higher g-levels to arrest the rebound.

B. Impact Testing of Ni-Cd Cells

(a) Description of Large Capacity Cells:

Since it was decided that a cell specifically designed for impact resistance would not be manufactured under the current contract, we felt it would be of value to study the large heat-sterilized Ni-Cd cells. Three cells of the approximately 25 AH size were available. Again it must be emphasized that these cells were not designed for impact resistance but were of geometric value in supporting some of our data on plate strength.

Cell #PR38 (Figure III-2a)

(12) Positive plates 6.6" lg. x 2.8" wd. x .0255" tk.
1.46 gm/in^2, 0.0596#/plate

(13) Negative Plates 6.6" lg. x 2.8" wd. x .026" tk.
1.61 gm/in^2, 0.0656#/plate

(26) Separator 0.005" tk.

Case 7 5/8" high x 2.925" wide x 0.832" tk. internal

Spacer 0.5" @ top

free SPACE:

Thickness -
Approx. 0.002"/plate

Width -
Approx. 1/16" each side

Height -
Approx. 7/16" Top
Approx. 1/16" Bottom

from: $\sigma = \frac{F}{A} = \frac{W(N)}{w \cdot t}$

4000 g → $\sigma_{\substack{max \\ pos}}$ = 3,340 psi

(assume no dynamic amplification) $\sigma_{\substack{max \\ neg}}$ = 3,610 psi

Cell #PR114 (Figure III-3a)

(10) Positive Plates 5.4" lg. x 2.8" wd. x 0.030" tk.
1.67 g/in^2. 0.0557 #/plate

(11) Negative Plates 5.4" lg. x 2.8" wd. x 0.032" tk.
2.04 g/in^2, 0.0680#/plate

(22) Separator 0.005" tk.

Case 6.31" high x 2.925" wd. x 0.832" tk internal

Spacer 0.5" tk. @ Top

free SPACE:
Thickness - Approx. 0.0018"/plate
Width - Approx 1/16" each side
Height - Approx 1/4" @ Top
Approx 1/8" @ Bottom

from: $\sigma = \frac{W(N)}{w \cdot t}$ (assume no dynamic ampl.)

4000 g → $\sigma_{\substack{max \\ pos}}$ = 2,650 psi

$\sigma_{\substack{max \\ neg}}$ = 3,040 psi

Cell #C33 (Figure III-4a)

(3) Positive Plates 18" lg. x 4.2" wd. x 0.0255" tk.
1.465 g/in^2, 0.244#/plate

(4) Negative plates 18" lg. x 4.2" wd. x 0.026" tk.
1.61 g/in^2 , 0.268#/plate

(6) Separator 0.005" tk.

Case 2.931" I.D. x 5.532" int. height

Spacer 0.5" tk @ top

free SPACE:

Thickness - Approx. 0.01"/plate
Height- Approx. 11/16"- 13/16" @ Top
Approx. 3/16"-1/4" @ Bottom

from: $\sigma = \frac{W(N)}{w \cdot t}$ (assume no dyn. impl.)

4000 g ➔ σ_{max}^{pos} = 2120 psi

σ_{max}^{neg} = 2290 psi

One cell of each configuration, as described and shown in the pre-impact x-rays (Fig. III- 2a, 3a, 4a), had been previously cycled and only cell #PR114 was shorted prior to our testing. Initial indications were that the plates in all these cells would support the loading imposed by a 4000 g - 1 msec impact! The stresses that have been calculated do not exceed the values obtained during static bearing tests for plates with the same degree of lateral restraint. Dynamic bearing stress values gave excellent correspondence with the static values and indicated that a significant dynamic amplification factor is not required. The plates used in these cells are much longer than those used in static bearing tests and approximately equal in length to those used in dynamic bearing tests. This implies a lower natural frequency and therefore even less concern for requiring a dynamic amplification factor. Thus our only conclusion from previous evaluation of the

FIG. III-2 a

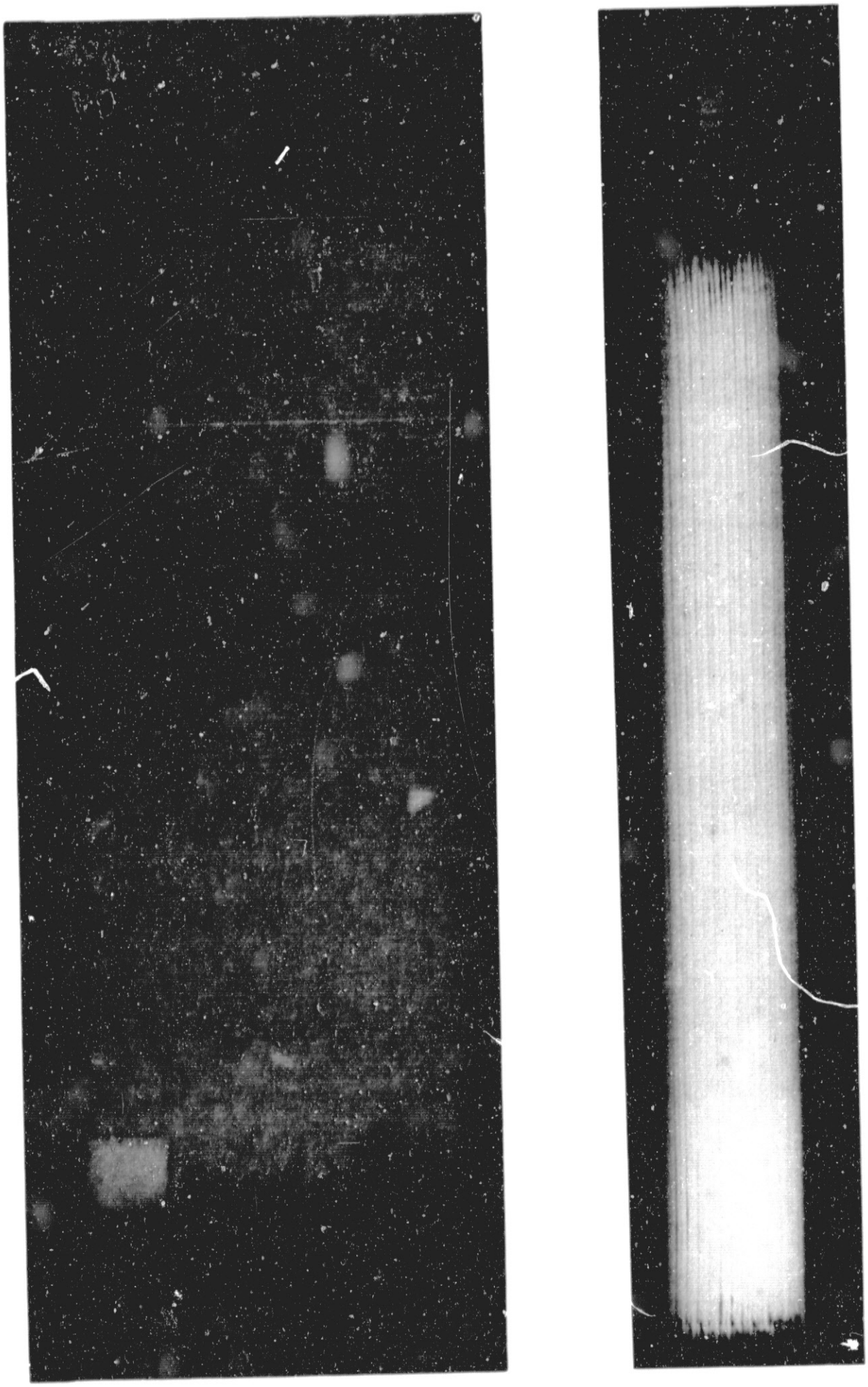

CELL #PR 38 PRE-IMPACT

FIG. III-3 a

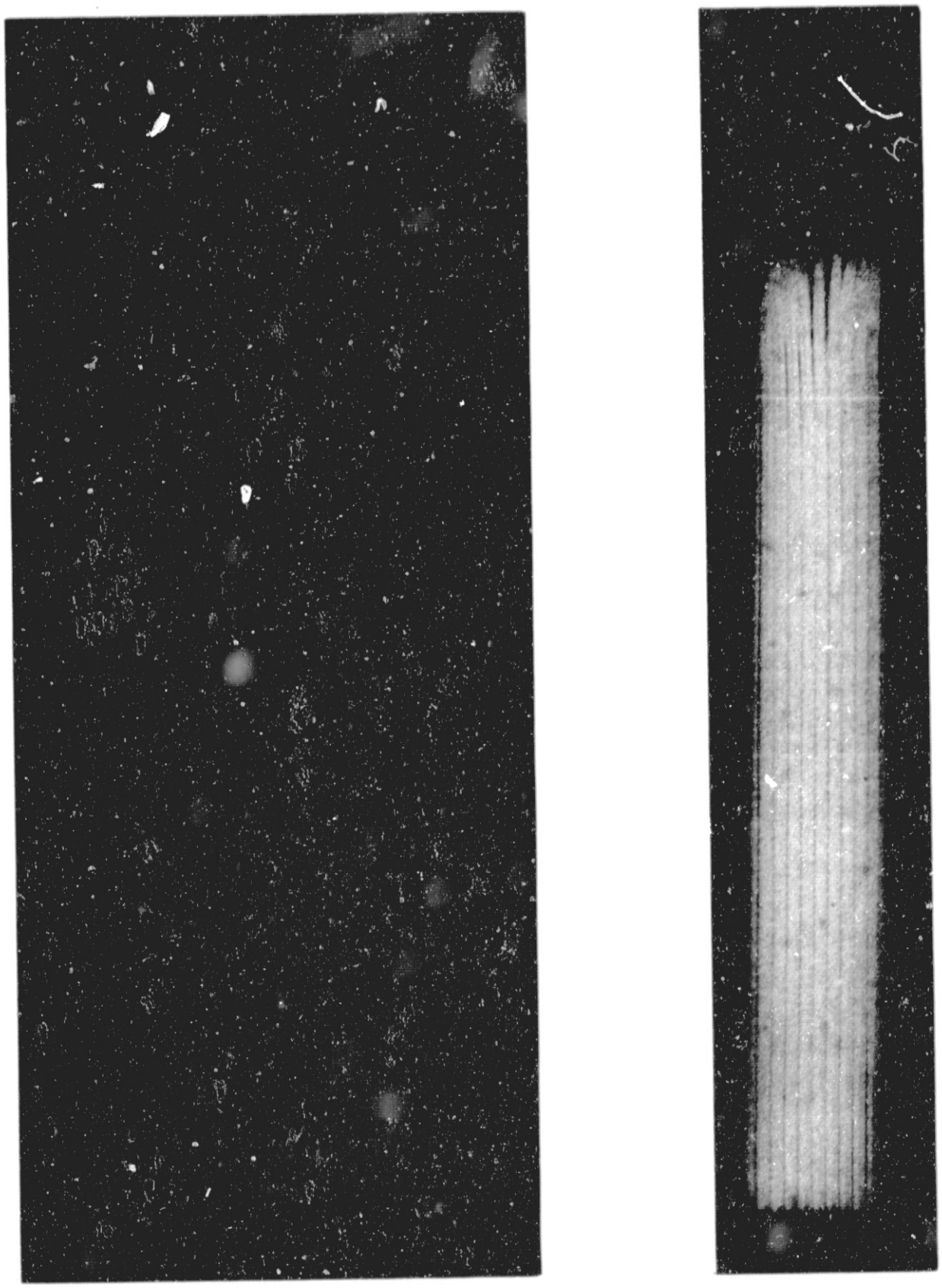

CELL #PR 114 PRE-IMPACT

FIG. III-4 a

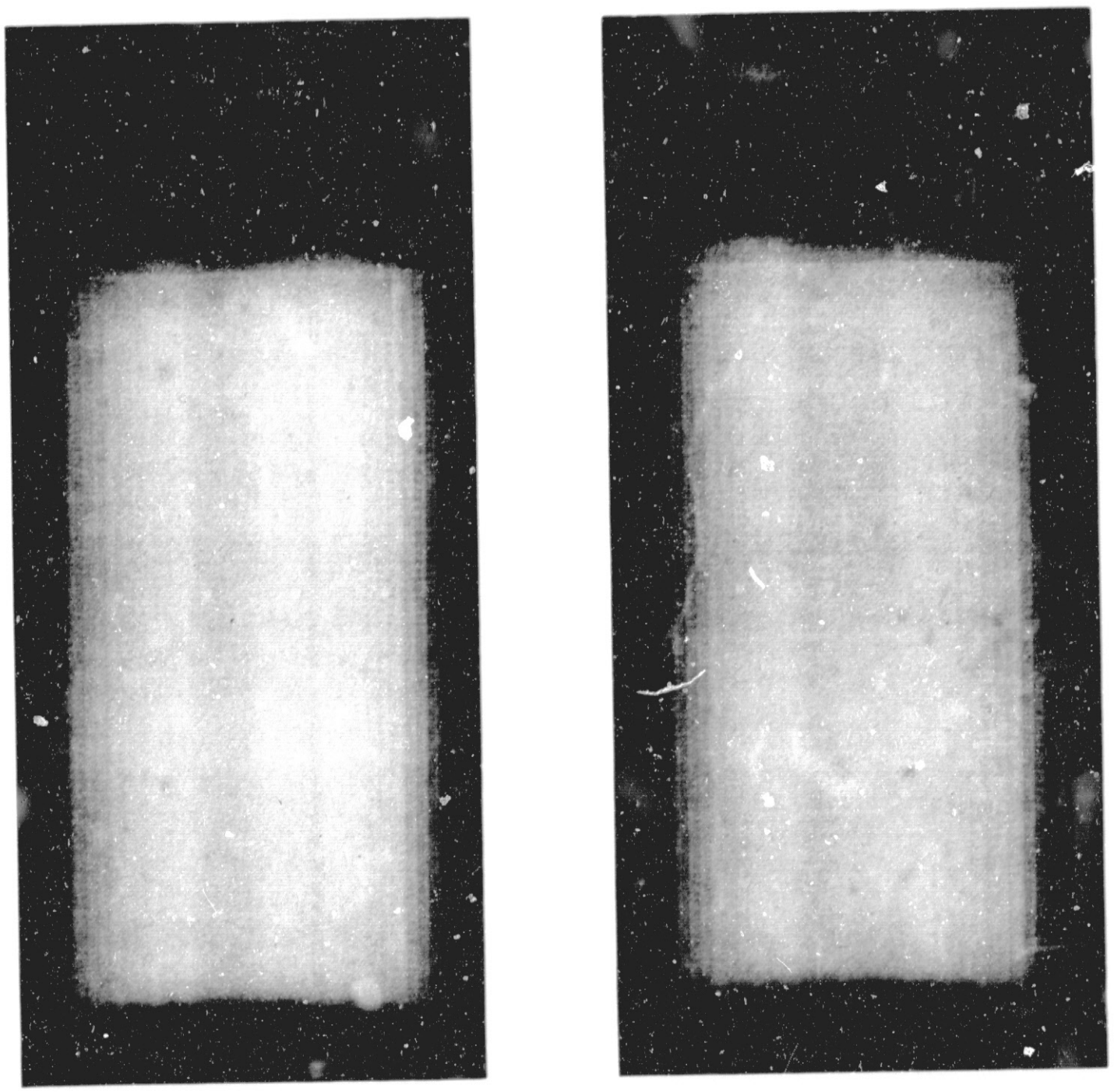

CELL #C 33 PRE-IMPACT

mechanical properties of Ni-Cd electrodes would be that the plates in any of these cells would survive impact.

(b) Analysis of the Impact Process:

The preliminary conclusions are indeed founded on design data. However, we must examine the manner of loading. There is reason for concern over the amount of free space permitted within these cells. It will be shown that this is the main reason for exmphasizing that these cells were not designed for impact resistance.

It is instructive to ask: Is a mere 1/16" vertical free space dangerous to a large cell's capability for impact resistance?

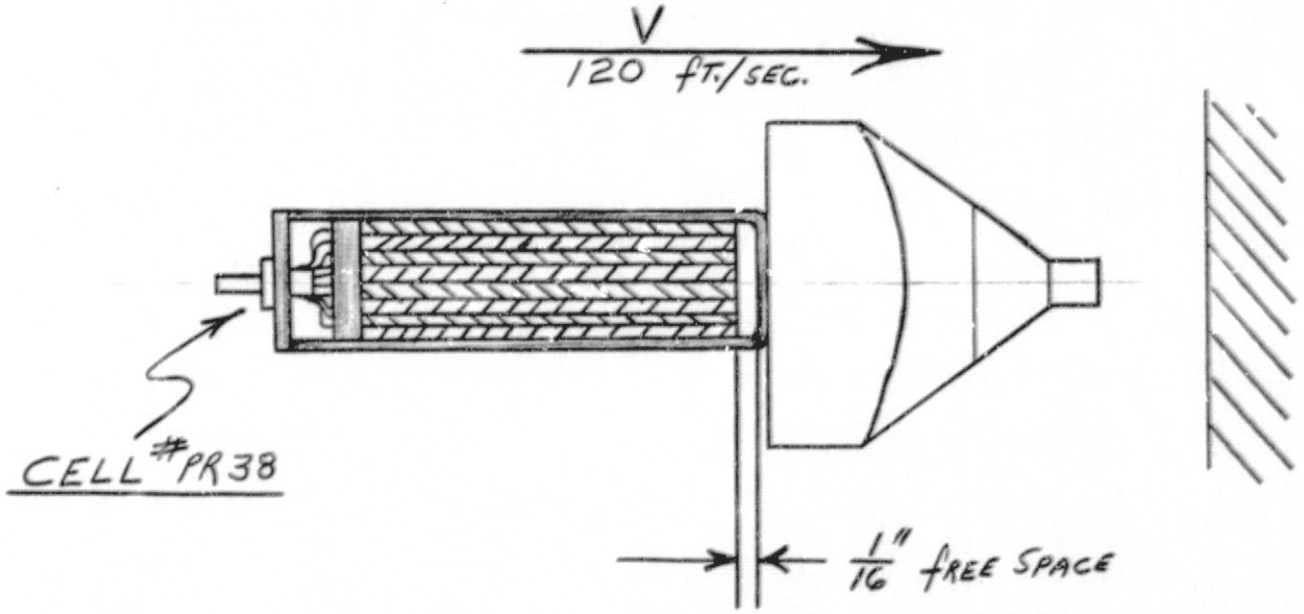

When impact occurs, the carriage, cell, and individual electrodes experience a 4000 g gravitational field for 1 msec. The resultant force exerted on a negative electrode is:

$$F = ma = 262\#$$

This force will accelerate the electrode to some higher velocity which will be limited by the distance (and thus the time) over which this acceleration

force can act:

$$S = v_i t + 1/2\ a\ t^2$$

$$t = 35\ \mu\text{sec}$$

with this time available to cover the 1/16" free space, the final electrode velocity at impact will be:

$$v_f = v_i + a\ t = 124.5\ \text{ft/sec}$$

Now during the same time interval, the carriage and cell case have to be decelerated to a velocity of:

$$v_f = v_i + a\ t = 115.5\ \text{ft/sec}$$

Diagramatically we have:

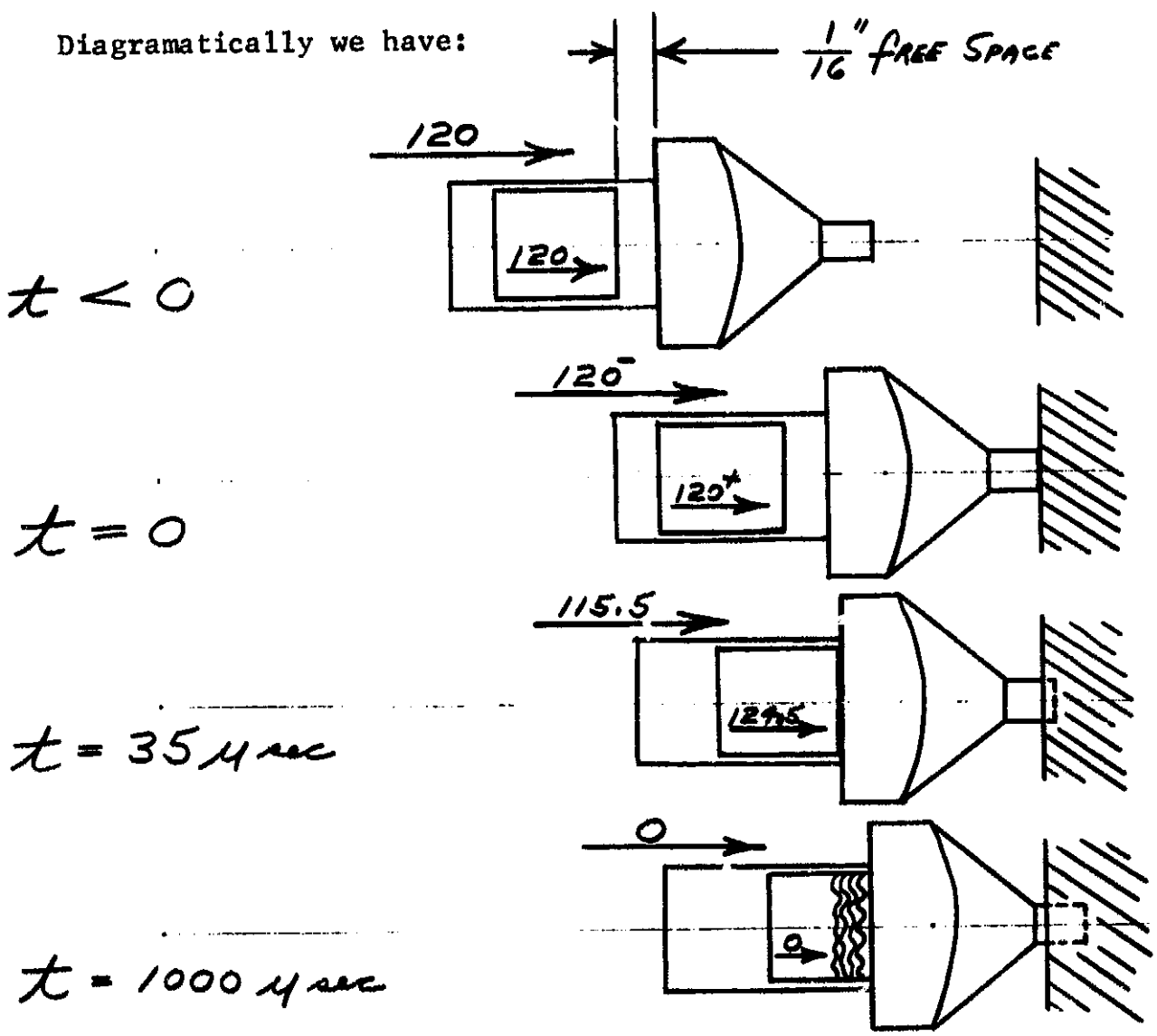

in reality therefore, we have the carriage and cell case experiencing entirely different loading than the electrodes:

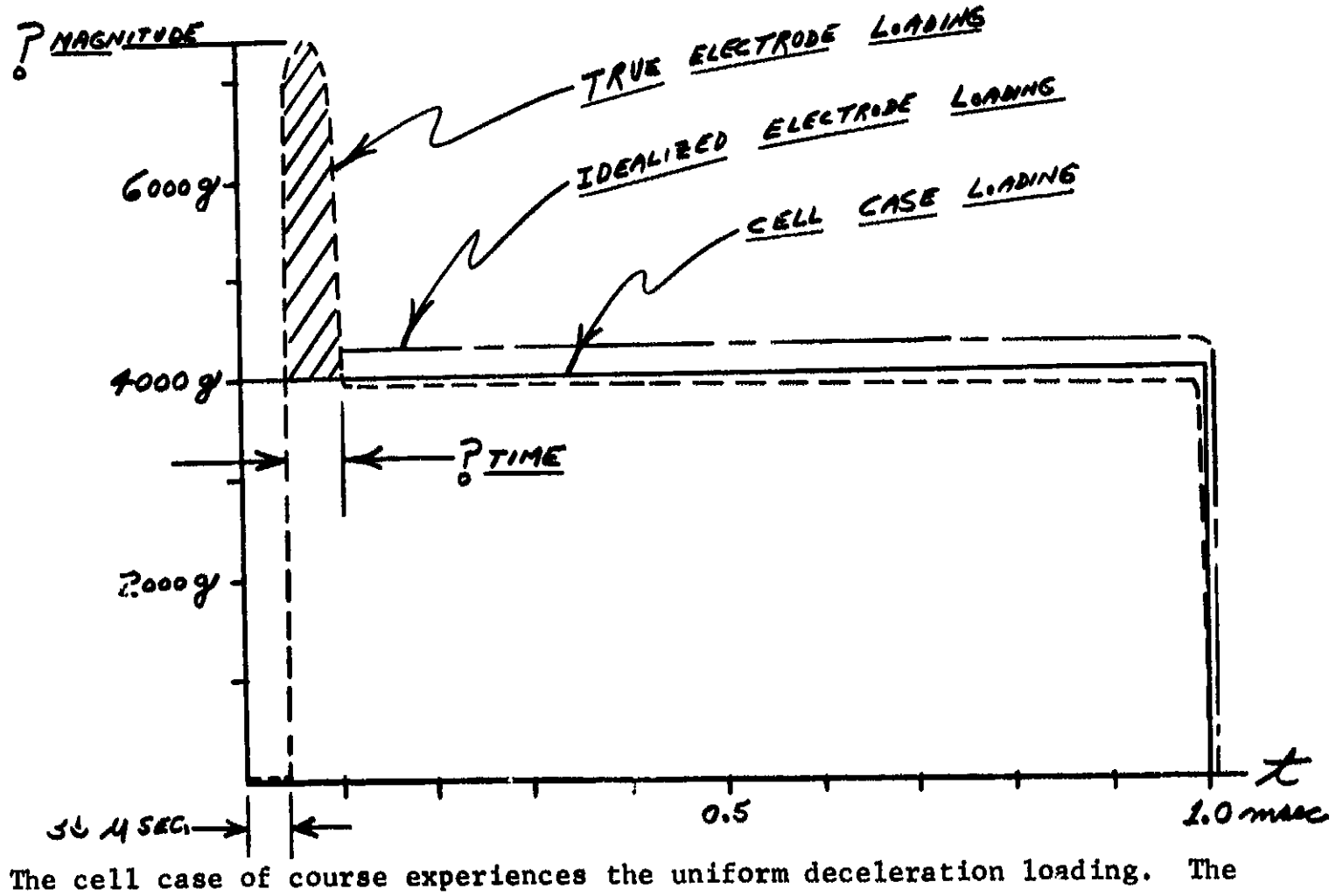

The cell case of course experiences the uniform deceleration loading. The electrode,however, has a relative velocity at its impact of 9 ft/sec which must be diminished before movement with the carriage (and 4000 g loading) can occur. Rapid deformation of the electrode will occur at this point, a loading increases for a short time. We can calculate the energy involved.

$$\int F.dt = m(\Delta v) = m \text{ (9 ft/sec)}$$

or the shaded area of the spike. Unfortunately, we can not determine the magnitude or time involved without additional experimental information describing the deformation process.

We can only assume that this is a small amount of energy and question if the electrode can accommodate it by deformation at maximum load for the remainder of time available. If the static bearing values are valid, the maximum stress that a negative electrode can support at .002"/plate lateral restraint is 3750 psi. Thus the maximum force is:

$$F = \sigma (w \cdot t) = 274\#$$

The amount of time required (by uniform force) to accomplish the total velocity change from 124.5 ft/sec —· - 0 ft/sec is:

$$F \cdot t = m (\Delta V)$$

$$t = 0.926 \text{ msec}$$

This amount of time is $<$ 0.965 msec still available and implies the deceleration could be accomplished safely (with a margin of only 39 μ sec!).

This exercise was performed for a specific plate (2.36 length: width ratio) and assumed a mere 1/16" free space yet, it dramatically illustrates the very fine distinction between failure and survival. Several points regarding this analysis must be noted:

1. The additional weight of electrolyte saturation was not included in the mass of the electrode.
2. The total area of the end of the electrode was presumed to be available for supporting load.
3. Prior to initial impact, the electrode pack was presumed stationary - maintaining its 1/16" relative distance to the cell case impact surface.
4. Most importantly, the effect of a damaging peak force at electrode

impact was neglected in our final statement of apparent survival.

(c) Results of Testing:

We shall now look at the results of impact tests performed on these cells and see that failure to achieve the above conditions will have rather obvious consequences.

The orientation of each cell during impact is shown below

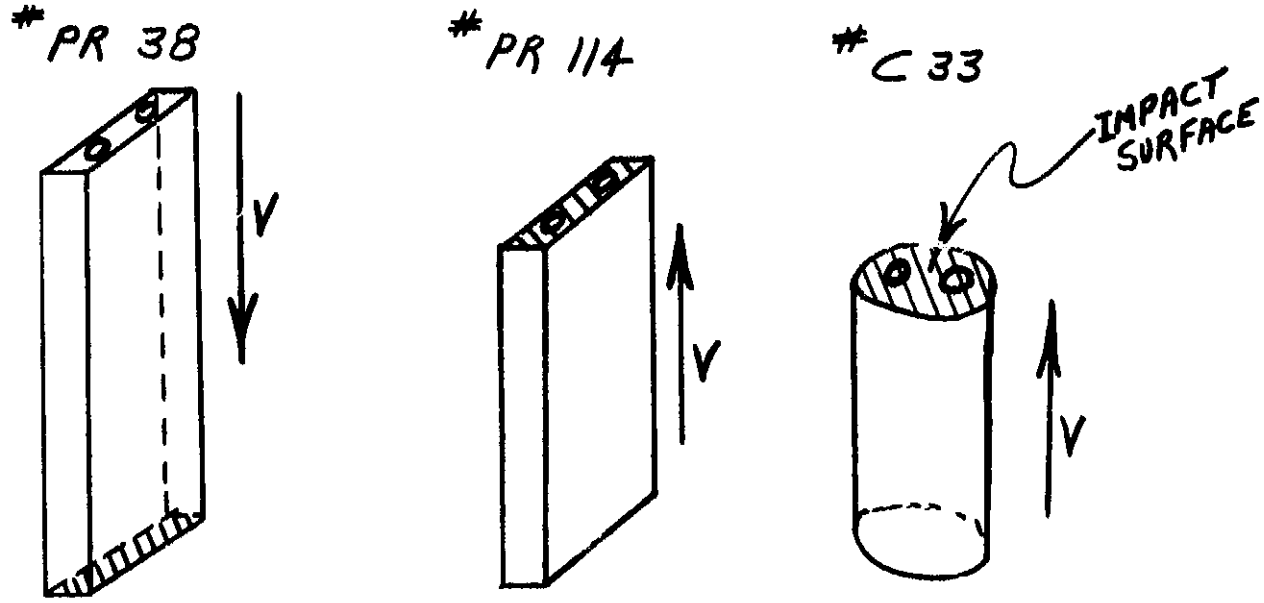

The description of the impact parameters for each cell (velocity, g-level, time) is given in Figure III-5 a, b, c. The time history of open circuit voltage during impact is also shown. All three cells failed under the imposed impact. X-rays taken of each cell immediately after impact are shown in Figures III-2b, III-3b, III-4b. Upon disassembly of each cell, photographs were taken of the electrode deformation and are shown in Figures III-2c, III-3c, III-4c. The visual evidence of failure depicts quite vividly the kinds of deformation that can occur when some of the earlier design points are not realized. We may discuss these tests individually:

FIG. III-5

UPPER TRACE: 2 msec/cm

LOWER TRACE: 0.5 msec/cm

(a) CELL #PR 38

V = 105 ft/sec

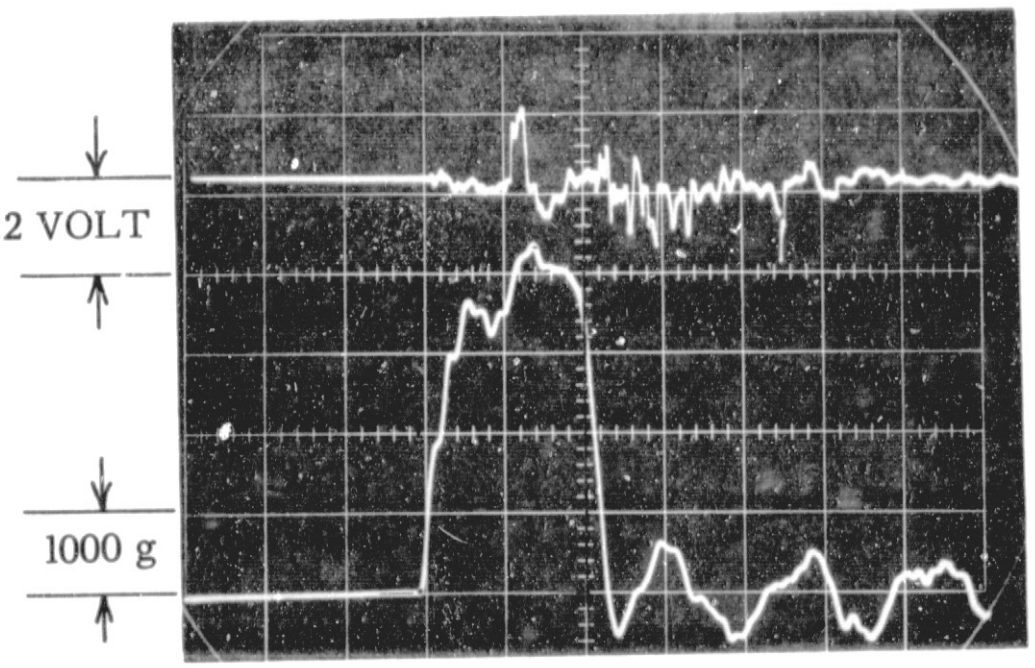

(b) CELL #PR 114

V = 104 ft/sec

EXTRANEOUS SIGNAL
NOT CONNECTED
TO SHORTED CELL

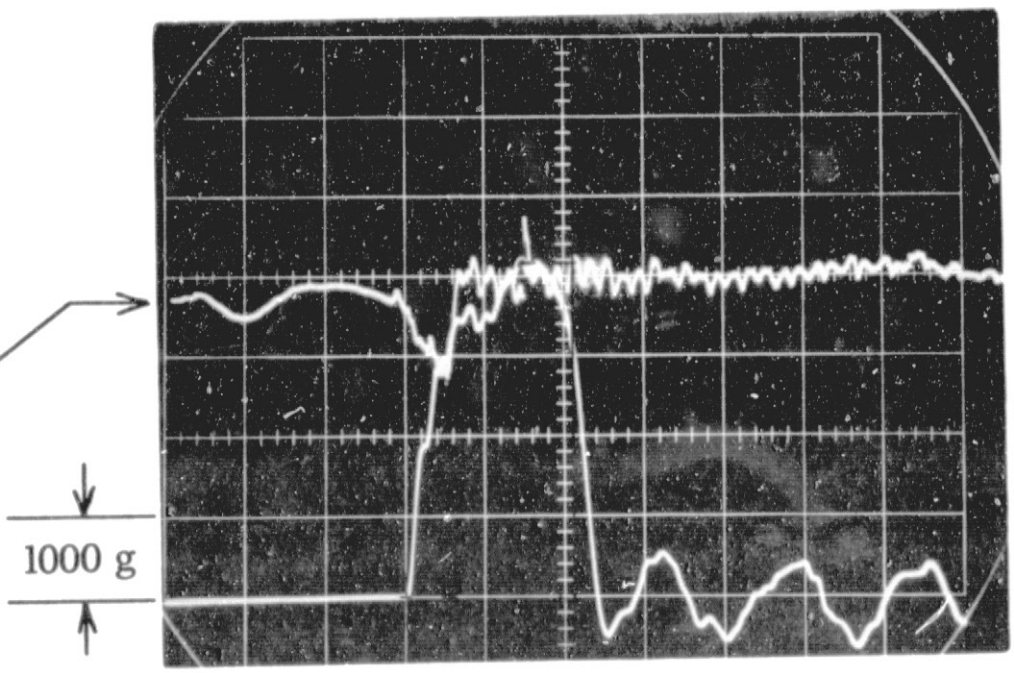

(c) CELL #C 33

V = 104 ft/sec

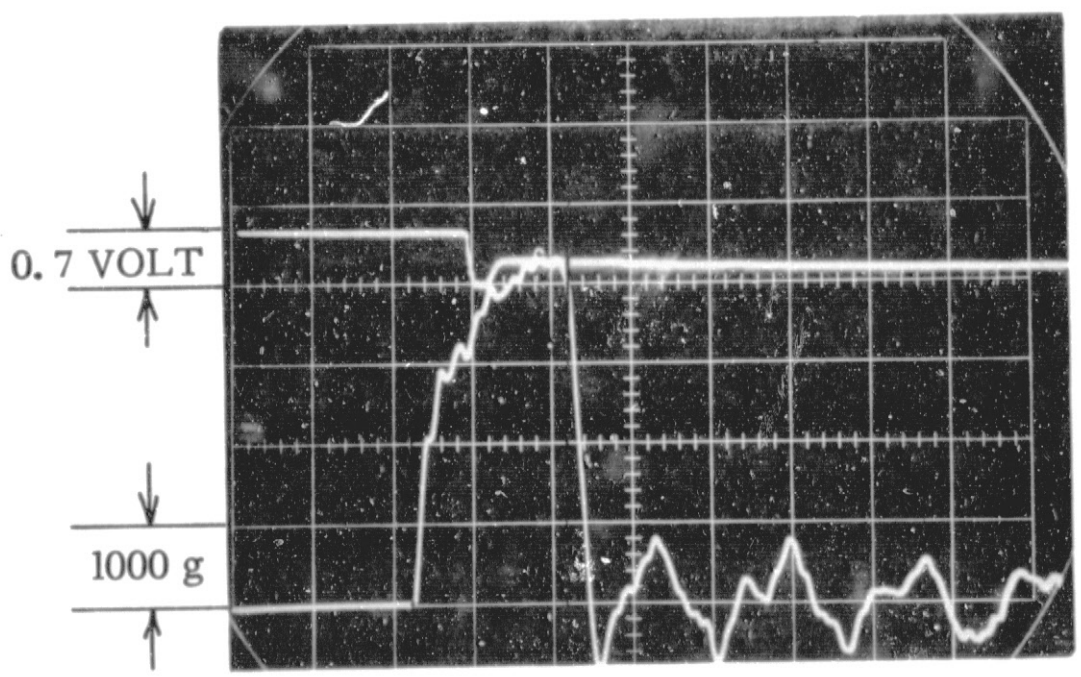

FIG. III-2 b

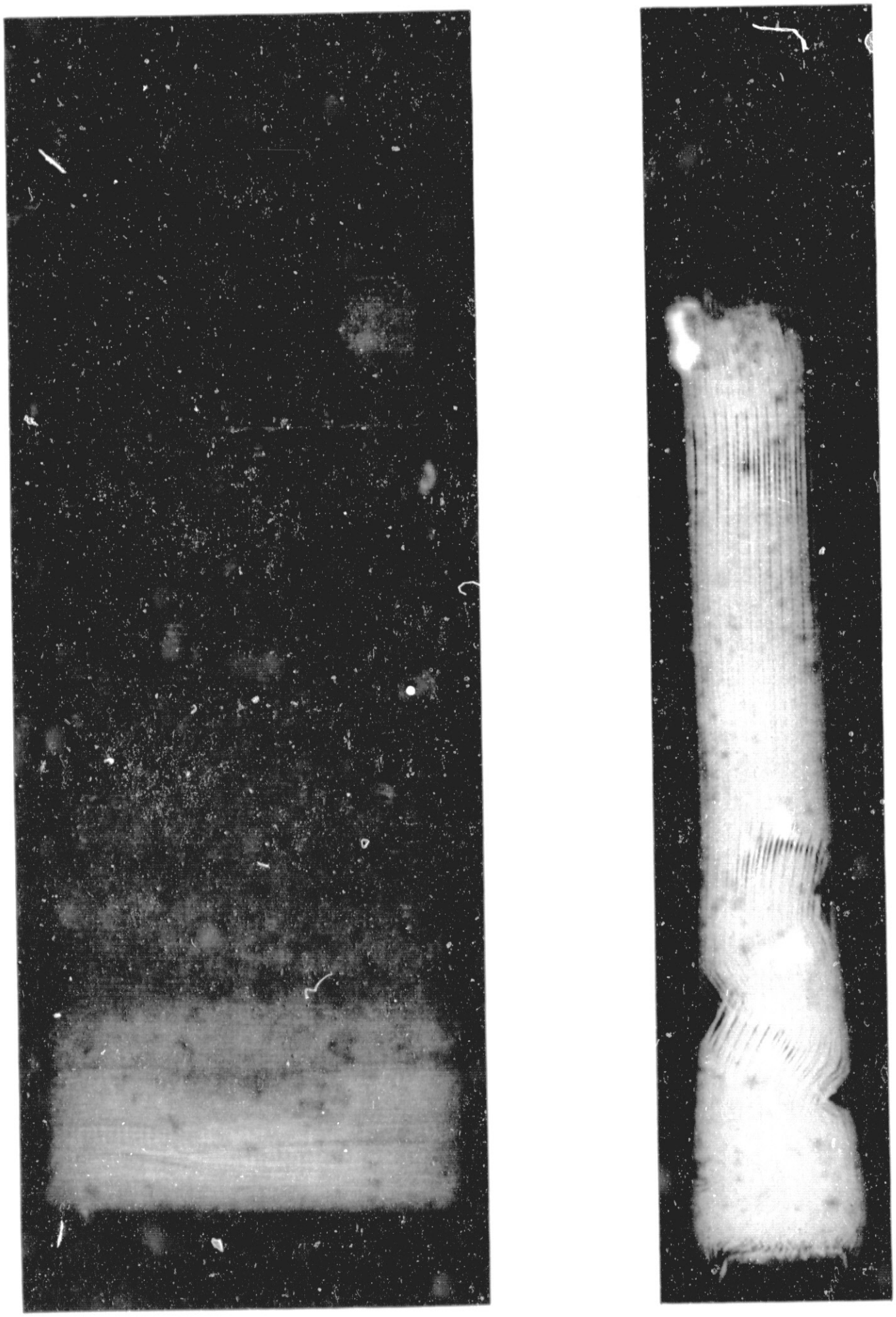

CELL #PR 38 POST-IMPACT

FIG. III-3 b

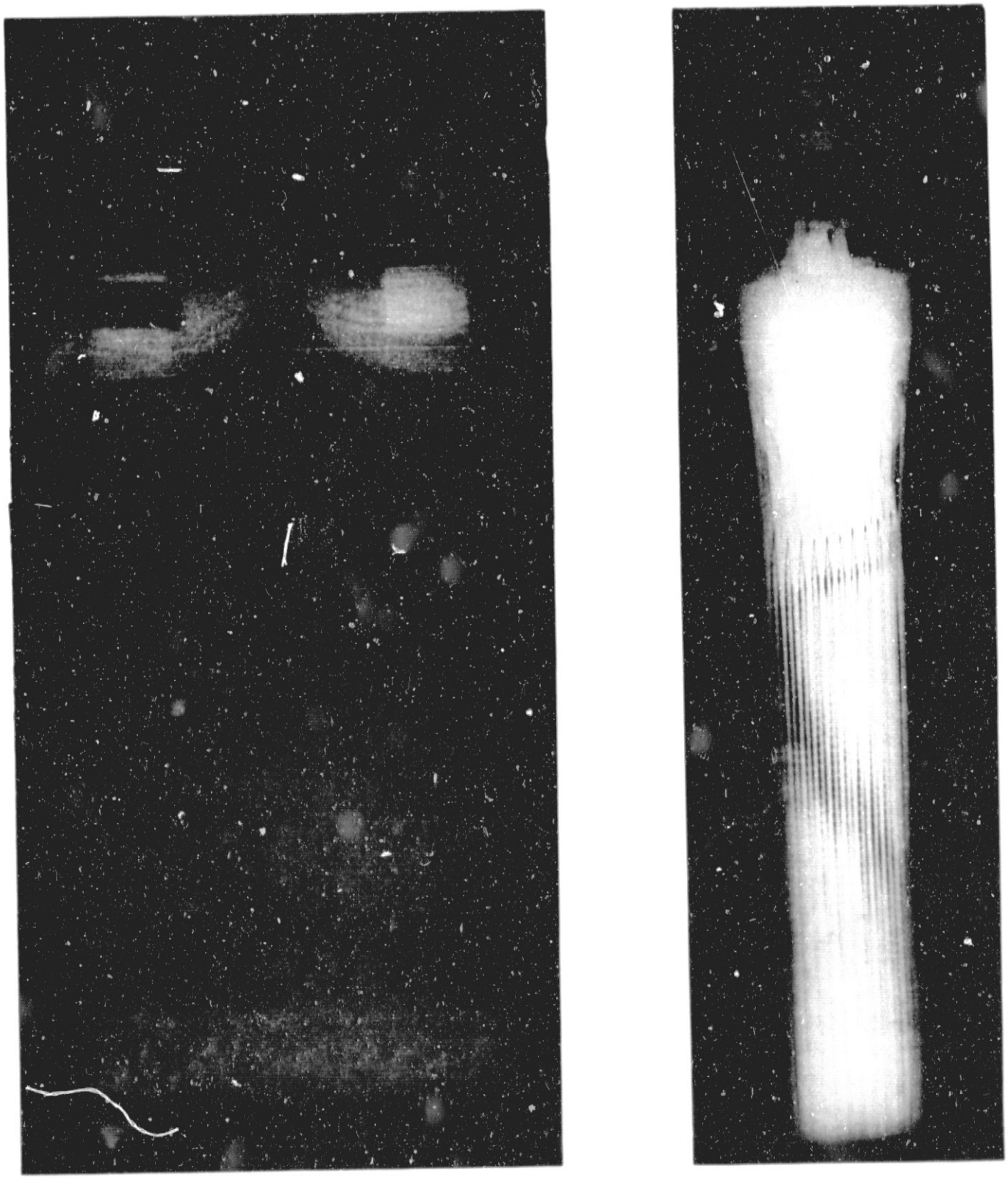

CELL #PR 114 POST-IMPACT

FIG. III-4 b

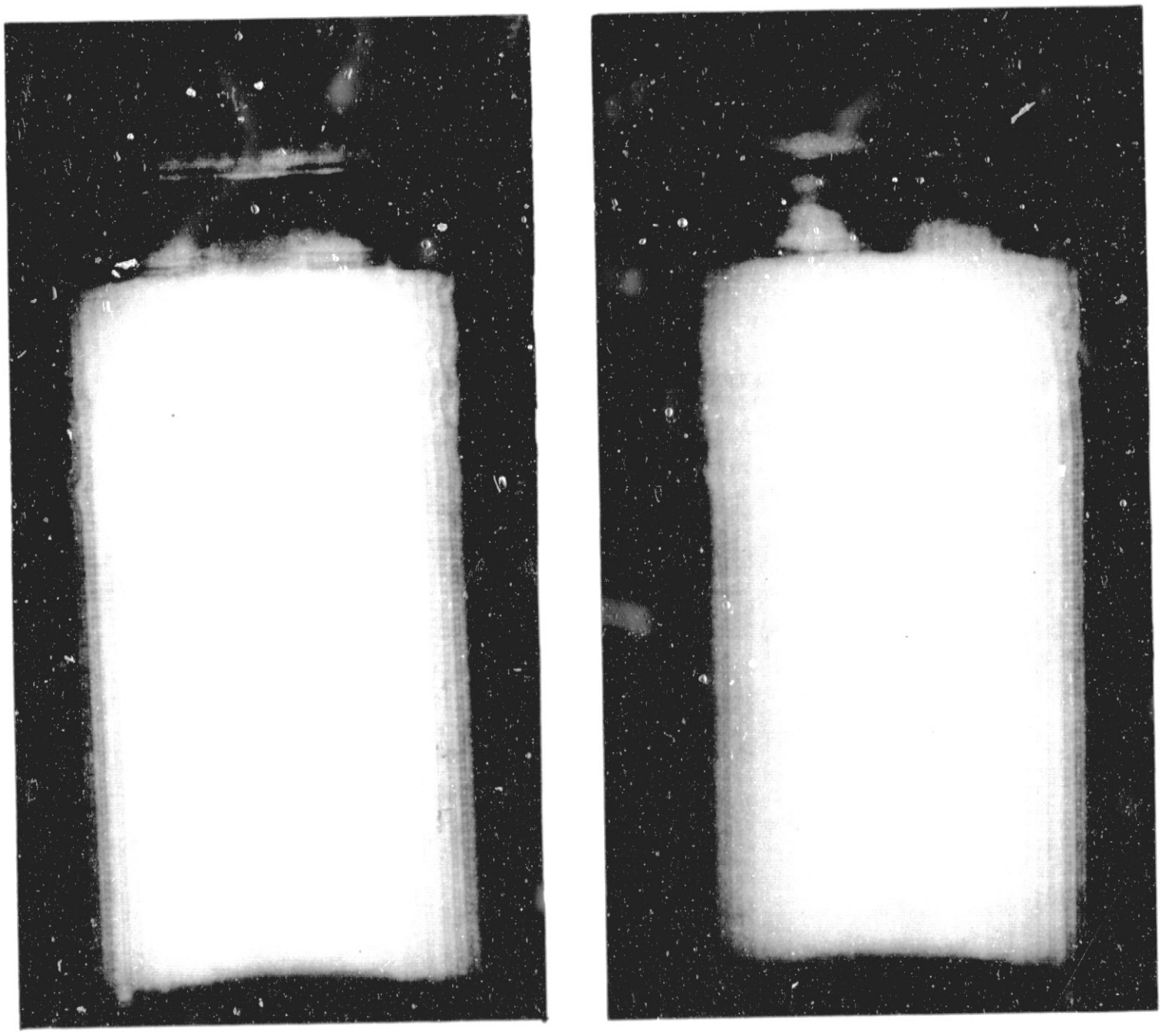

CELL #C 33 POST-IMPACT

FIG. III-2 c

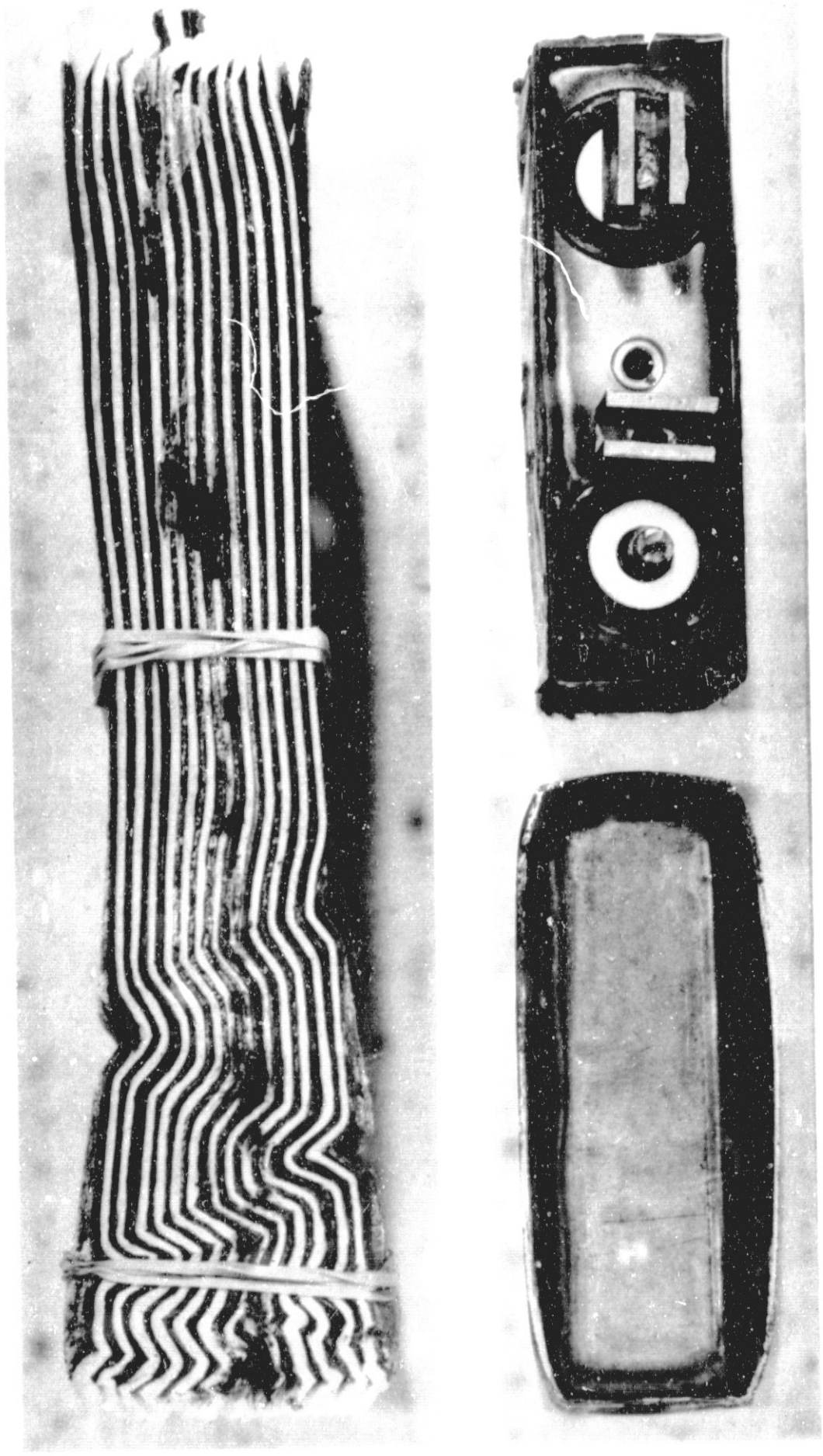

CELL #PR 38

FIG. III-3 c

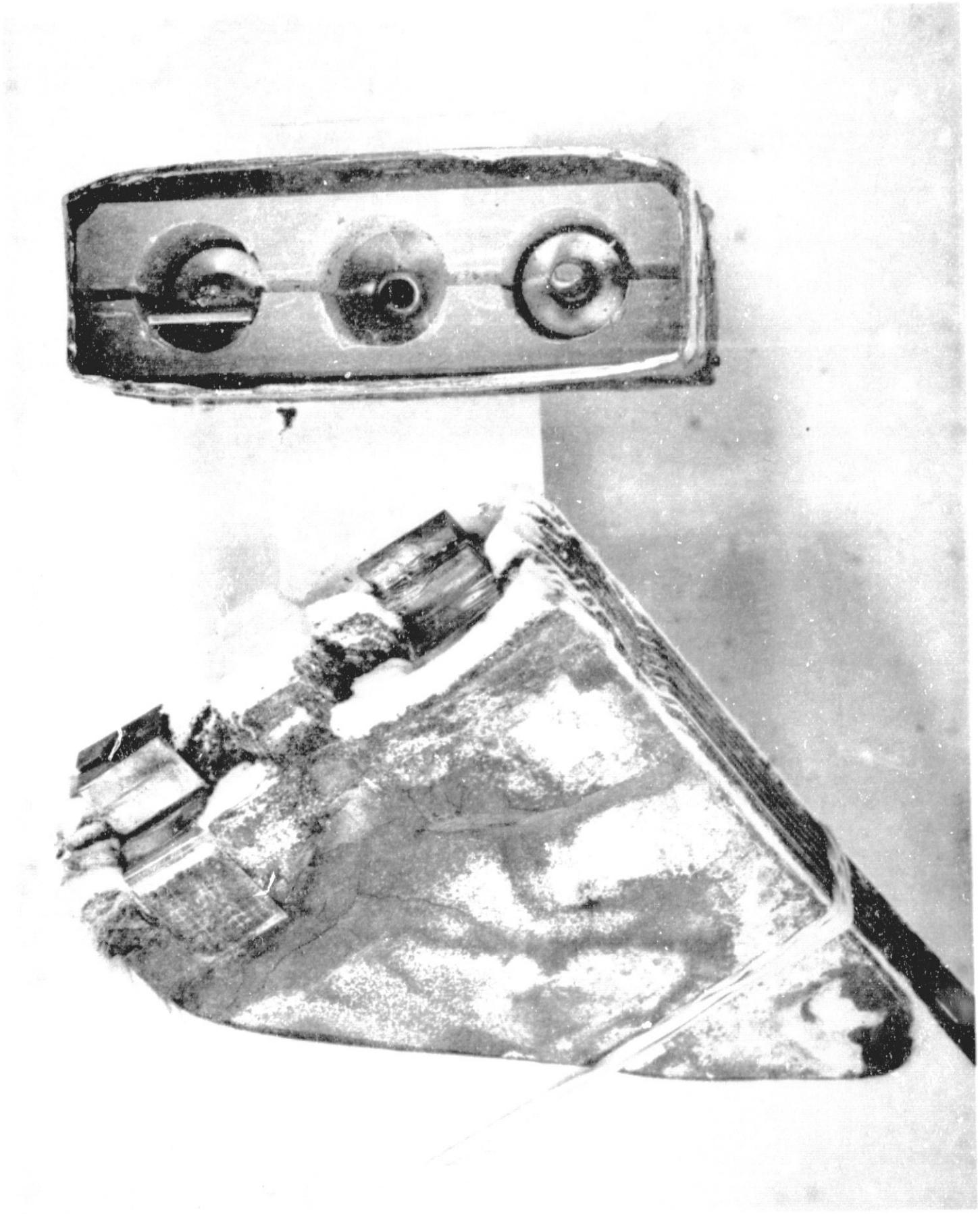

CELL #PR 114

FIG. III-4 c

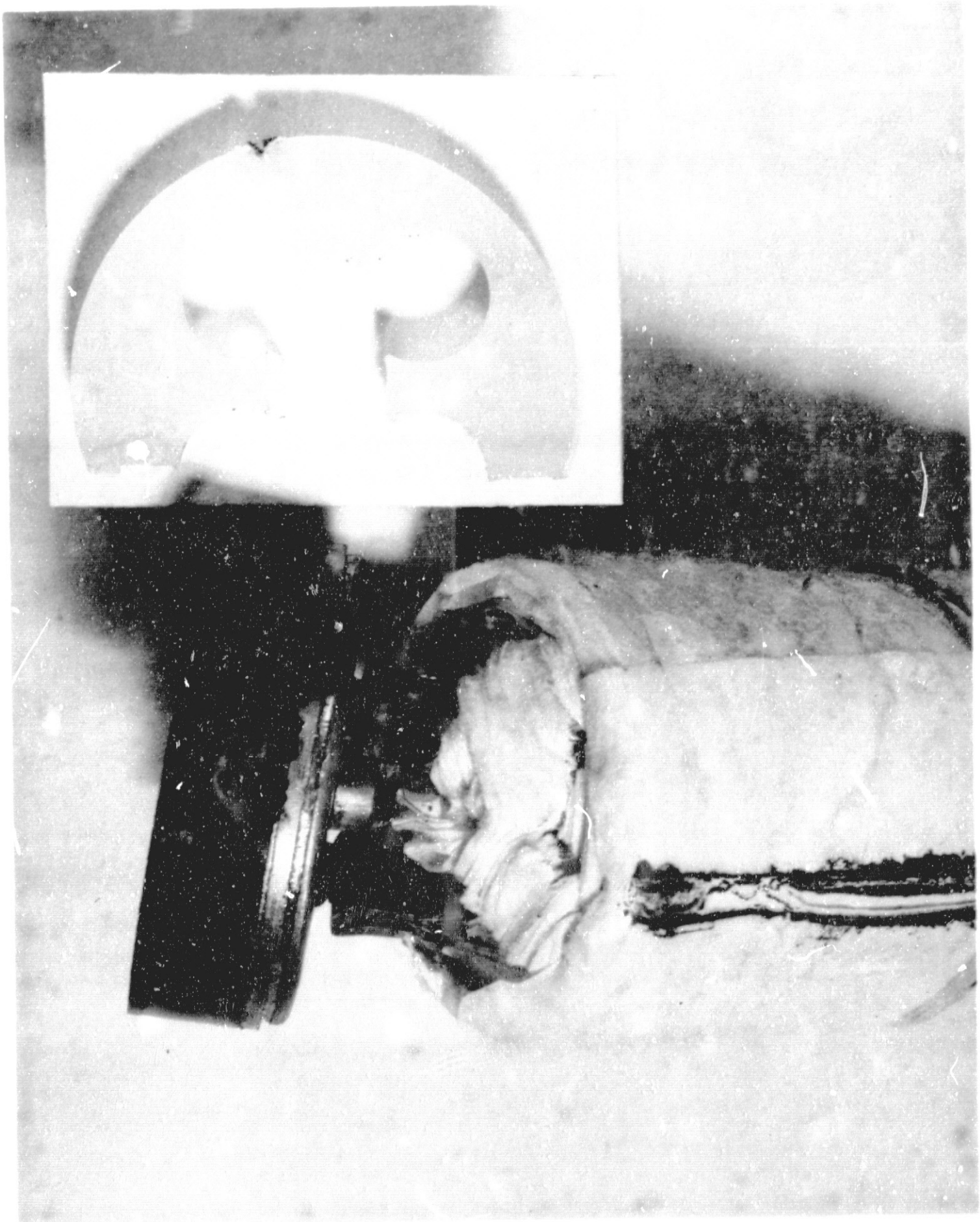

CELL #C 33

Cell #PR38:

The large prismatic cell failed in buckling of the electrodes. It was our decision to test each cell as an entity in the sense that external restraints would not be used. This lack of restraint showed that the cell case alone is not of sufficient strength to support its own weight under inertial load and the lateral pressure imposed on it by the deforming electrode pack. The electrode pack apparently had sufficient laterial restraint and support from its terminals to withstand the loading during acceleration. This is both a visual observation and the presence of full voltage at impact. Under deceleration a much lower degree of laterial restraint was available from the cell case, and the electrodes had little difficulty in buckling (Fig. III-2b, c). The electrodes could not reach the full value of stress which they are capable of supporting. The post-mortem failure analysis also showed that one terminal collector had apparently not been welded. This is the most likely cause for the erratic voltage trace shown in Figure III-5(a). We note, however, that voltage was maintained on this cell despite the defective terminal and the extensive deformation. It is our contention that this cell would not have experienced failure if thicker axial spacers and lateral restraining plates had been used.

Cell #PR114:

The smaller prismatic cell had the largest free space at the impact end of any cell and is largely responsible for the damage. We cannot make a judgement on the motions during acceleration. Although there is no visual damage to the bottom of the electrode pack we do not have a trace to

indicate the voltage at impact. During deceleration both terminal collectors were fractured. The most significant lesson in the study of this cell is the total ineffectiveness of the spacer design.

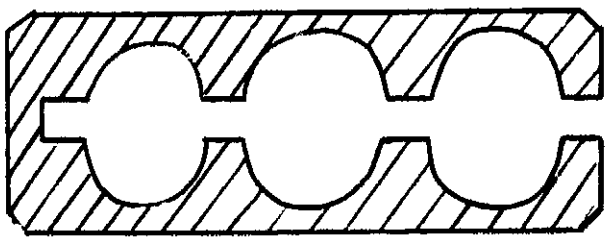

$\Rightarrow 1.35\ in^2$

63% of ELECTRODE PACK BEARING AREA

The predicted stresses for this cell become meaningless under this situation and failure is the obvious consequence. The visual observations of the top of the electrode pack dramatically show the areas which supported load (Fig. III-3b,c). The spacer vent hole area is quite emphatic. We note that the failure mode in supported areas is again buckling. This again indicates that low lateral restraint (static plate spacing and dynamic cell case expansion) prevented the electrodes from reaching their ultimate compression stress.

Cell #C33:

The cylindrical cell developed direct shorting in the terminal areas of the cell (Fig. III-5c) as electrode motion was severe during impact. Again, the spacer design was solely responsible for this failure.

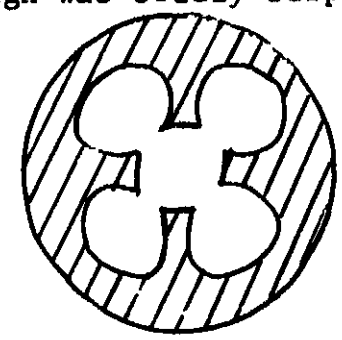

$\Rightarrow 2.60\ in^2$

59% of ELECTRODE PACK BEARING AREA

As shown in Fig. III-4b, c, the plates moved forward into the open areas of

the spacer. The open core in particular had large axial excursion. Again, there was no damage to the cell during acceleration (visual observation and cell voltage trace). It is significant that this cylindrical configuration has resisted nearly totally the buckling mode of failure. Even in the areas where severe bearing loads were possible, the x-ray analysis shows only traces of buckling. The stability of the cylindrical cell is apparent mainly because of the inherent cell case design. What we have seen is that the cell cases in the two prismatic designs (without the benefit of restraining plates as normally used on batteries) were the prime cause of lowering lateral restraint under impact condition. This confirms our contention that our electrodes themselves will resist buckling and go on to the true ultimate compressional stress that we have established.

In conclusion, the study of these cells has provided the design emphasis that we desired. The importance of static assembly plate spacing, the use of spacers that maximize effective bearing area and axial thickness, and the cell case contribution to pack integrity have been adequately demonstrated. In short, we have stated the precautions that must preceed the use of our design data to predict a cell's behavior under impact loading.

C. TESTING OF Ni-Cd ELECTRODES

(a) MECHANICAL PROPERTIES OF ELECTRODES IN BEARING LOADING:

1. INTRODUCTION:

The determination of the mechanical properties of Ni-Cd electrodes under tensile and compressive loading has been previously documented in the eighth quarterly JPL report (April - June, 1969). This report will describe the third and final method of loading employed to complete the strength characterization of this material. Bearing tests, although certainly related to the study of compression loading have been distinguished here as a separate method. The main reason is that we do not insist upon any one failure mode. Instead, we attempt to shift from one failure mode to another in a controlled fashion. A second reason for distinguishing this series of tests is that the present manner of loading more closely approximates the type of freedom and failure that might be experienced in an actual battery. It was envisioned that under high gravitational fields our plate material might exhibit any one of three failure modes:

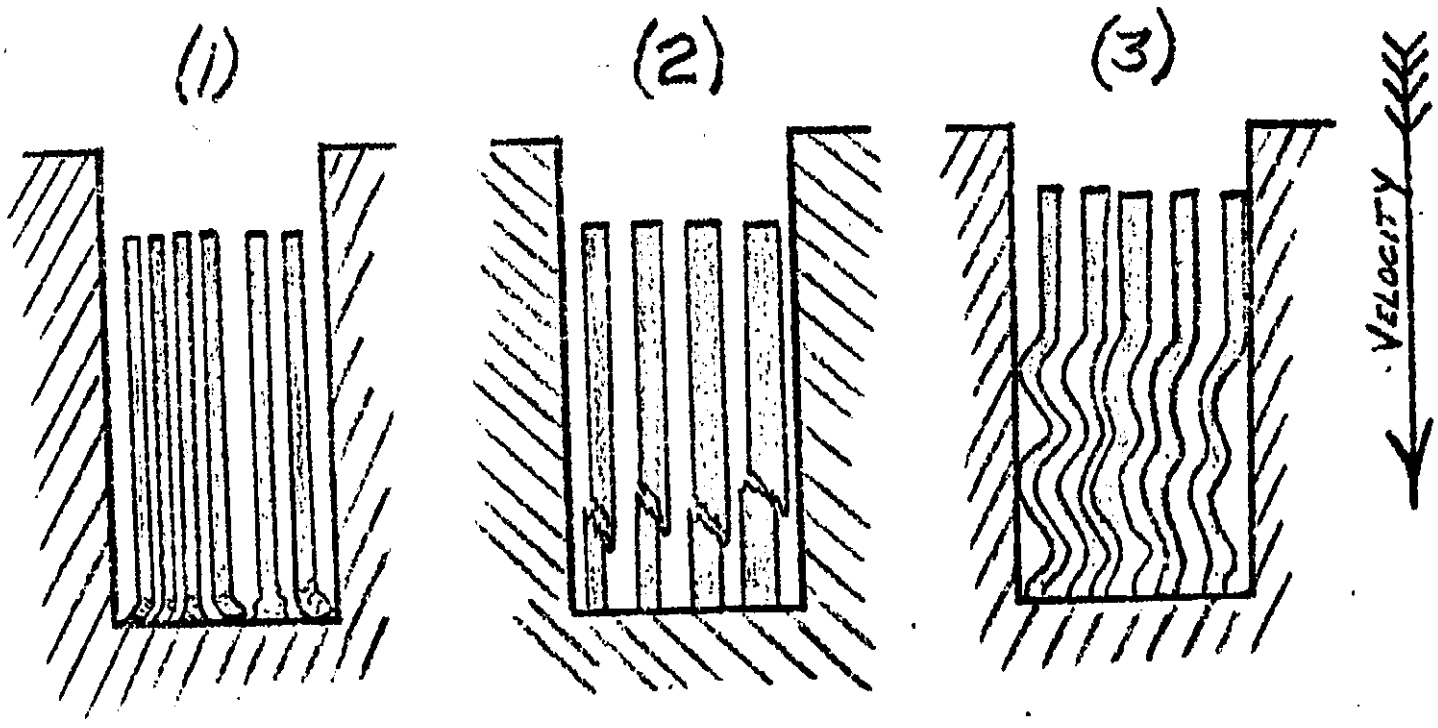

(1) True Bearing Failure: The bearing failure mode would be exemplified by edge crushing of the plate material at the fixed impact surface. If this failure mode were exhibited, it would

occur at a lower value of inertial stress than that maximum required to cause compressional failure as previously determined (JPL eighth QTR report). This failure mode has significant implications to the battery manufacturer since it is most likely to cause separator penetration and shorting of the cell.

(2) Compression-Shear Failure: The true compression failure mode would be exhibited if ultimate bearing stress exceeded ultimate compression stress. If this is the case, then the value observed would represent the maximum inertial stress that can be supported by this material. It is obvious, therefore, that the battery designer would be extremely interested in this determination.

(3) Buckling Failure: The buckling mode of failure will be observed at a lower stress level than that associated with either failure mode (1) or (2) and is obviously to be avoided. Hence, the determination of the degree of lateral restraint necessary to prevent this transfer of failure mode is of prime design important.

With these considerations and goals in mind, the experimental program was outlined to investigate the occurance of all three failure modes under controlled lateral restraint at both static and dynamic rates of loading.

2. CONSTANT DEFORMATION STATIC TESTING:

The static bearing loading was accomplished on a universal testing machine at a constant deformation rate ($\dot{\varepsilon} \approx 0.0007\ sec^{-1}$). The manner of specimen loading is shown on the proceding page:

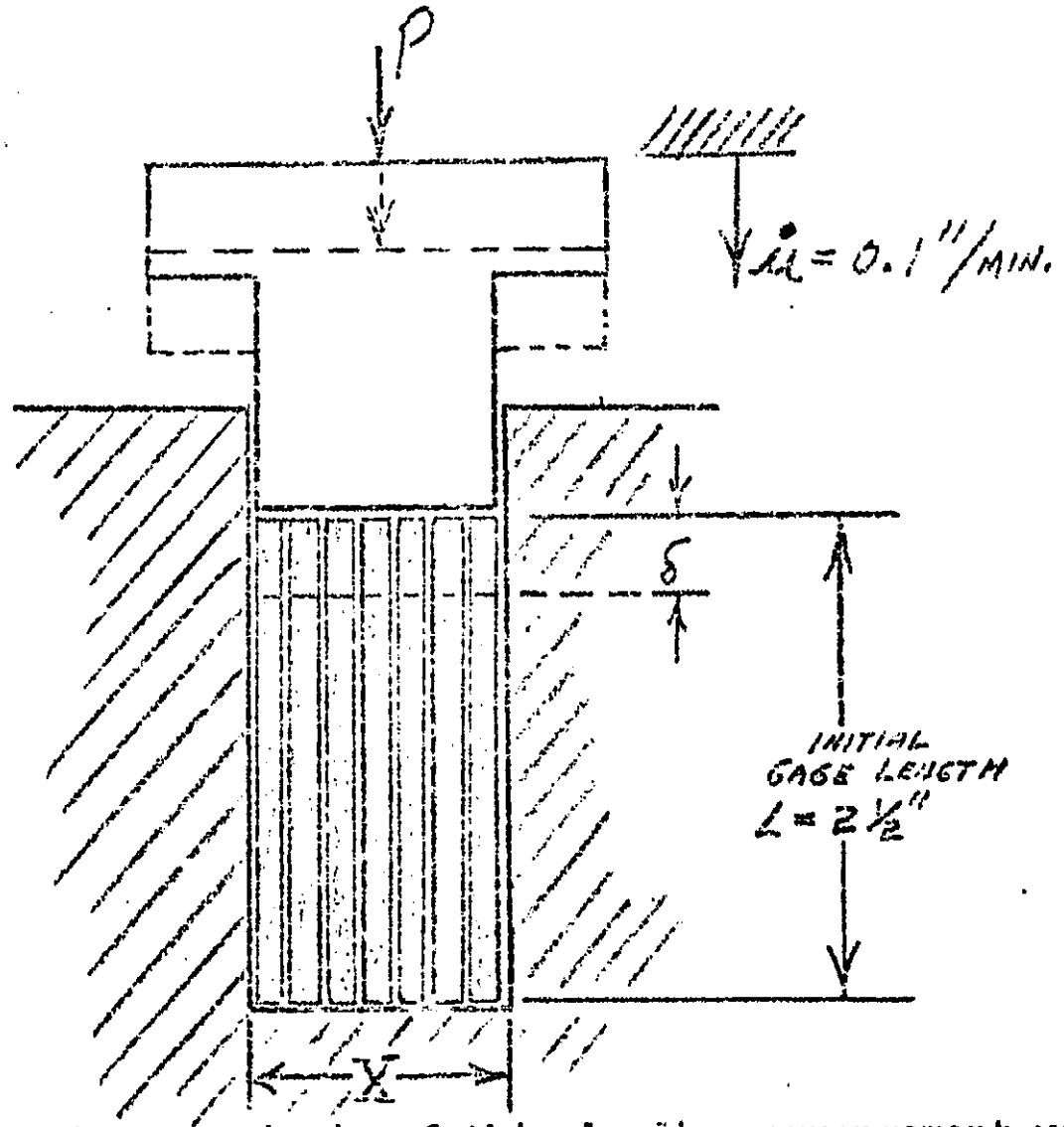

The essential characteristic of this loading arrangement was the controlled lateral restraint. The degree of lateral restraint was normalized for all tests to a value of additional space allowed for each electrode.

$$S = \frac{X - \left[(t_{p1} + t_{p2} + \ldots + t_{pn}) + (n + 1)\, t_s\right]}{n}$$

S = excess deformation space permitted per plate (in)

X = constant dimension of fixture

t_{p1} = thickness of plate (Typ. 0.026")

t_s = separator thickness

n = number of plates

Thus stress, σ, could be defined as:

$$\sigma = \frac{P}{w(t_{p1} + t_{p2} + \ldots + t_{pn})}$$

where the denominator is simply the area of plates being compressed and P is the total force as recorded from the load cell of the machine on the y-axis. Strain in this study was taken as $\epsilon = \frac{\delta}{L}$ and again $\delta = \dot{\mu} t$ was directly displayed on the x-axis of our recorder.

The static bearing tests carried out under this type of loading were conducted on positive and negative plates at spacing values ranging from .000"/plate - .009"/plate. The specimens are shown in Fig. III-6. The progression from left to right illustrates the complete transfer of failure mode from true compressional-shear to buckling as the spacing is increased. We observe the ultimate loads decrease to that minimum level associated with pure buckling. Important to note is the total absence of edge-crushing or true bearing failure. What is observed then, is an ultimate bearing stress which seems to be greater than the ultimate compression stress for this material under static conditions.

The complete stress-strain behavior as defined above is shown for these specimens in Figure III-7 and III-8. Ultimate strain levels are fairly uniform regardless of failure mode mainly due to our definition of an overall apparent macro-strain. The stress levels are important however and large differences have been exhibited in direct relation to the spacing allowed and our ability to restrain buckling. The values of buckling stress and ultimate compression stress obtained in this study agree very well with the values determined earlier under strict compression loading (Figure III-*H*, eighth JPL QTR report).

TABLE III-1

MATERIAL	STATIC BUCKLING STRESS		ULTIMATE COMP. STRESS	
	Compression (1/2"G.L.)	Bearing (Max. Spacing)	Compression (1/4"G.L.)	Bearing (Min. Spacing)
Pos. Plate	2700	3000	5600	6500
Neg. Plate	2300	2300	3000	4900

FIG. III-6

STATIC BEARING

MAXIMUM STRESS (S)

NEGATIVE

.000"/PLATE

S = 4910 PSI

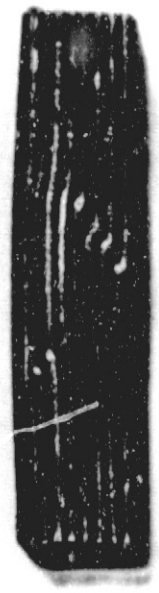

.001"/PLATE

S = 4000 PSI

.0025"/PLATE

S = 3715 PSI

.0045"/PLATE

S = 2760 PSI

.009"/PLATE

S = 2290 PSI

POSITIVE

.000"/PLATE

S = 6500 PSI

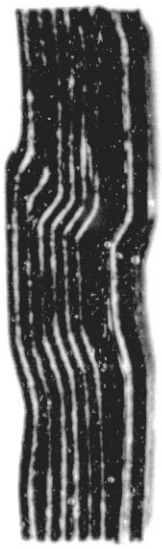

.0025"/PLATE

S = 4585 PSI

.001"/PLATE

S = 5480 PSI

.0045"/PLATE

S = 1385 PSI

Fig III-7

STRESS vs STRAIN

STATIC BEARING

Positive Plate

.005 IN/Plate

.0025 IN/Plate

.0015 IN/Plate

* OBSERVED BUCKLING

σ_{cr} (ksi) $\times (10)^2$

0 6 12 18 24 30 42 48 54 60

0 1 2 3 4 5 6 7 8 9

STRAIN inch/inch $(10)^{-2}$

Fig III-8

STRESS vs STRAIN

STATIC BEARING

Negative Plate

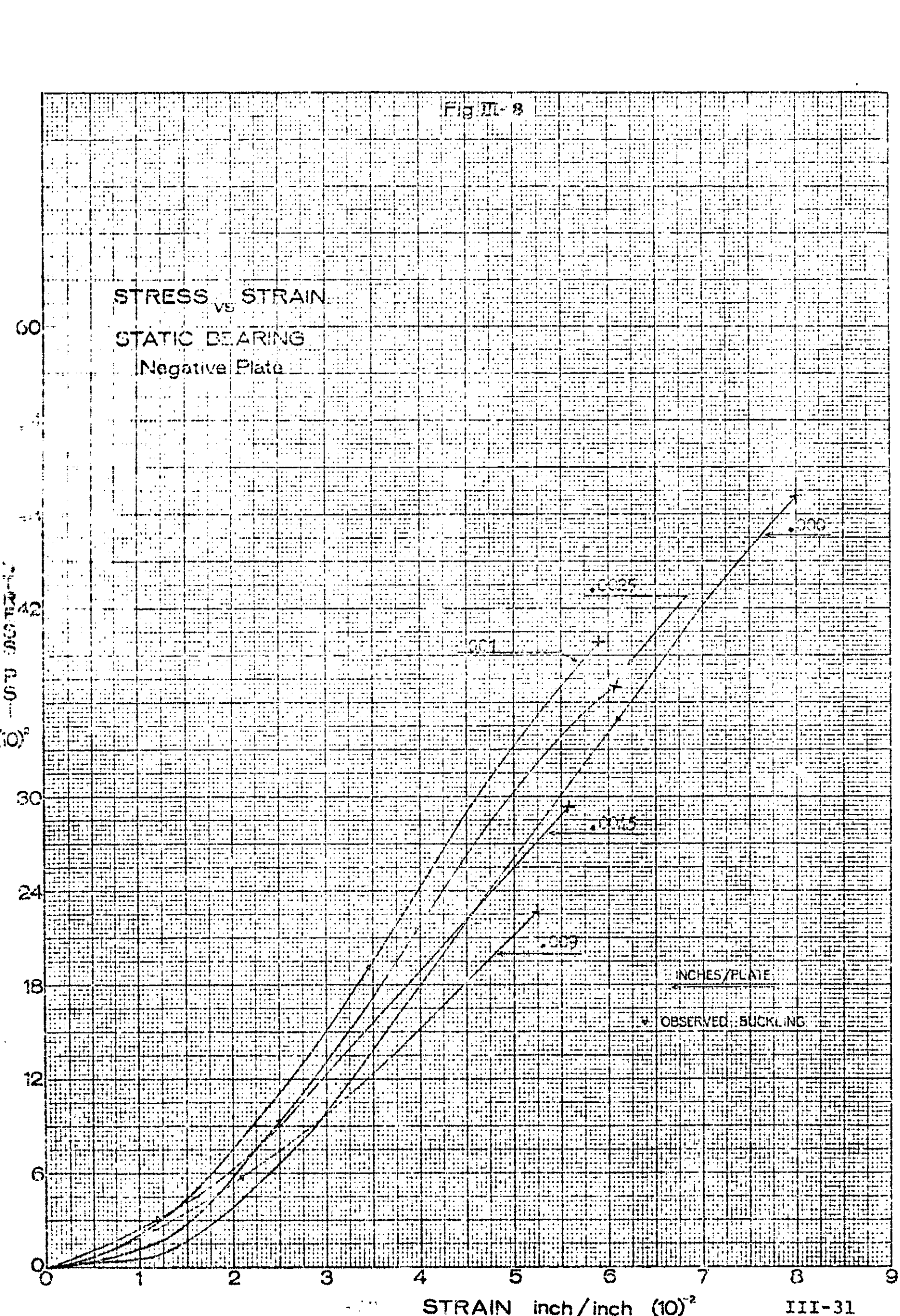

3. DYNAMIC BEARING LOADING:

Having established a static strength foundation, we were interested in observing possible changes in these values because of increased loading rate. Dynamic bearing tests were performed by use of a loading fixture as shown below:

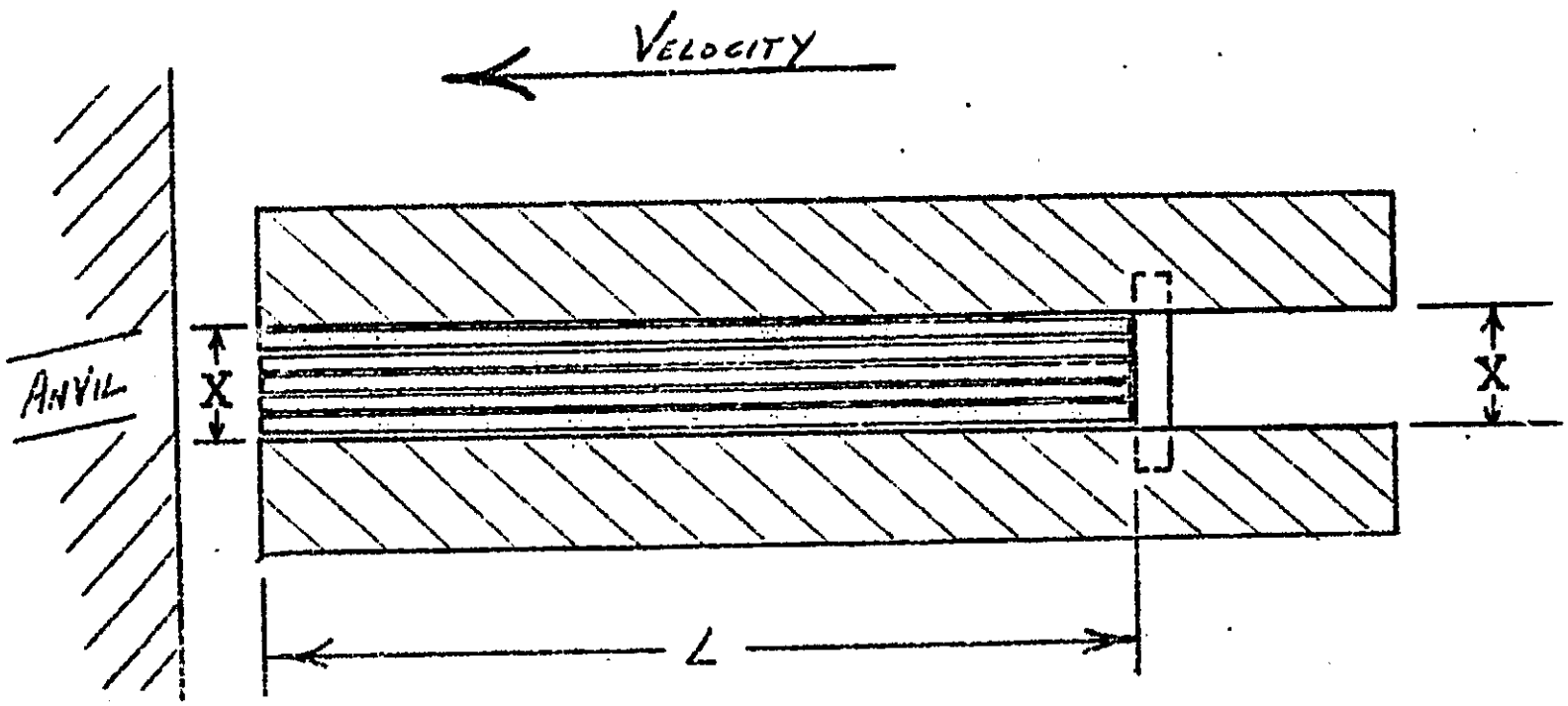

In this arrangement the plates were not "fixed" as in the compression fixture but were free to move and to crush at the ends if sufficient force was applied. Controlled spacing/plate, however, through the use of shims, was the essential feature of this fixture in order to duplicate the static conditions of loading. Initial plate length and impact level could be varied and thus maximum stress, σ_{max}, has been defined here as:

$$\sigma_{max} = \frac{P}{A} = \frac{m(Ng)}{(t \cdot w)} = \frac{(w \cdot L \cdot \rho)(Ng)}{g\ (t \cdot w)}$$

$$\sigma_{max} = \left(\frac{\rho}{t}\right)(LN)$$

where: ρ = area wt. density (#/in.^{2})
t = plate thickness (in.)
L = plate length (in.)
N = number of g's accel. (-)

Thus, for a given test at a controlled spacing/plate, the maximum stress would be calculated from the measurement of plate dimensions and applied deceleration. This max. stress would either cause visual failure at the end of the plates or it would not. If this max. stress was sufficient to fail the plates, we would lower the value to find the point where the material would not fail. If the same max. stress was not sufficient to fail the plates, the level would be raised to the point of failure. This partly explains the span line of experimental determination of failure-non failure shown later on Fig. III-9. This procedure was followed for each value of spacing selected. Fig. III-9 presents the values of dynamic failure loads superimposed on the static failure loads as a function of plate spacing or degree of lateral restraint. The static curves are well behaved and exhibit the greater strength of the positive electrode and show both electrodes tending toward a nearly common buckling stress asymptote. This is again in agreement with the earlier static compression study. These curves display the need to maintain a high degree of lateral restraint if excessive loading must be endured.

The dynamic load levels that are indicated as span lines on Fig. III-9 are not solely the limits of two experimental levels. We have included in these lines the results of both positive and negative plates. Several of each type were placed in each fixture and the difference in stress was very small. This was essentially as expected since it agreed with the static results observed - that at larger spacing, buckling is dominant and there is thus little distinction between the two electrodes. This is shown by the joining of the two static curves and their tending toward a common asymptote.

As lateral restraint was increased, however, we reached a point where we were unable to produce failure in either electrode (single point on Fig. III-9 @ .0025" spacing). In other words, taking the longest plate (6-5/8") that could be accommodated in

Fig III-9

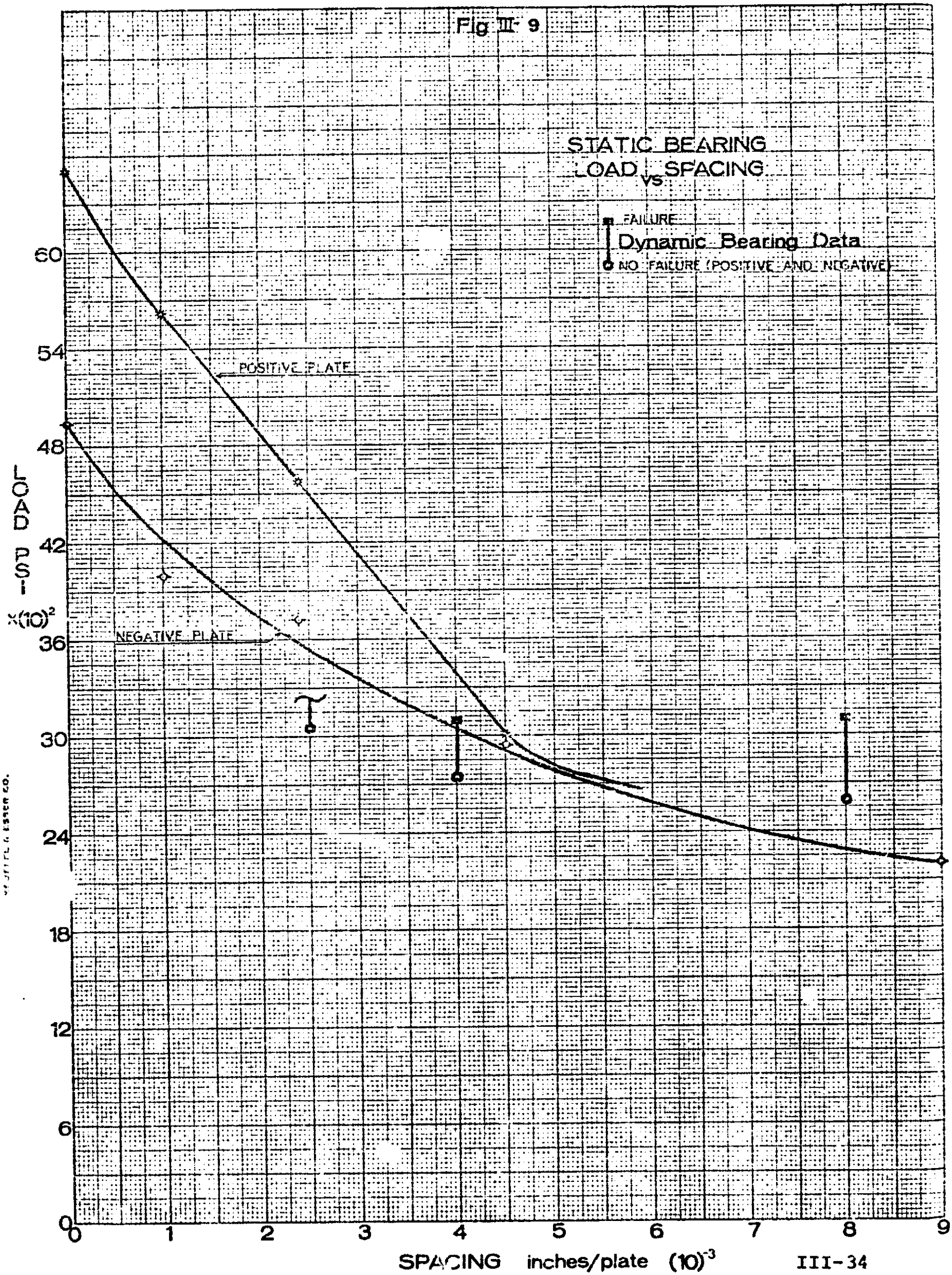
STATIC BEARING
LOAD vs SPACING
FAILURE
Dynamic Bearing Data
NO FAILURE (POSITIVE AND NEGATIVE)
POSITIVE PLATE
NEGATIVE PLATE
LOAD PSI X(10)²
60
54
48
42
36
30
24
18
12
6
0
0
1
2
3
4
5
6
7
8
9
SPACING inches/plate (10)⁻³

our fixture, and employing the highest impact level (meas. mean 4000g) for 1.1 msec from 110 ft./sec.) Available at that time, the maximum stress developed (3100 psi for NEG.; 2900 psi for POS.) was not sufficient to produce failure. Thus only a lower bound could be established at this degree of lateral restraint (see Table III-2).

It appears, however, that the dynamic curve, if able to be completed, would have a shape or character similar to the static curve. The dynamic values of ultimate stress are nearly equal to those obtained statically and supports the position that $\dot{\varepsilon}$ effects may not be important in compression (see discussion pg. III-42 and III-45 eighth JPL QTR report). This is valuable information in that it makes the transfer from static to dynamic results less complicated.

The failure modes exhibited in the dynamic study included all three mechanisms to some degree. In the case of minimum lateral restraint, the onset of buckling at the impact end was dominant as expected. As we increased the degree of lateral restraint, both compression-shear (very close to the impact edge) and bearing failure (edge crushing of the impact surface) were displayed in nearly equal amounts. It appears therefore, that in high rate loading the ultimate bearing stress nearly coincides with the ultimate compression stress.

It is valuable as a final summary to tabulate the dynamic results obtained in this study and compare them with previous determinations of dynamic ultimate strength.

TABLE III-2

	Dynamic σ_{ult} Tension	Dynamic σ_{ult} Compression	Dynamic σ_{ult} Bearing @.008"	@.004"	@.0025"
Pos. Plate	2000	>2600	2800	2800	>2900
Neg. Plate	2000	2400	3000	2800	>3100

(b) Friction Properties of Electrodes:

Several methods of loading were employed during the electrode characterization work which maintained adjacent plates in close proximity. In the case of bearing, a prime variable was the degree of lateral restraint as normalized by the spacing/plate. Precautions were taken in this type of testing to insure a reasonable approximation of the frictional forces between electrodes. These techniques were based on a measurement of frictional behavior. A series of tests were carried out in the following manner:

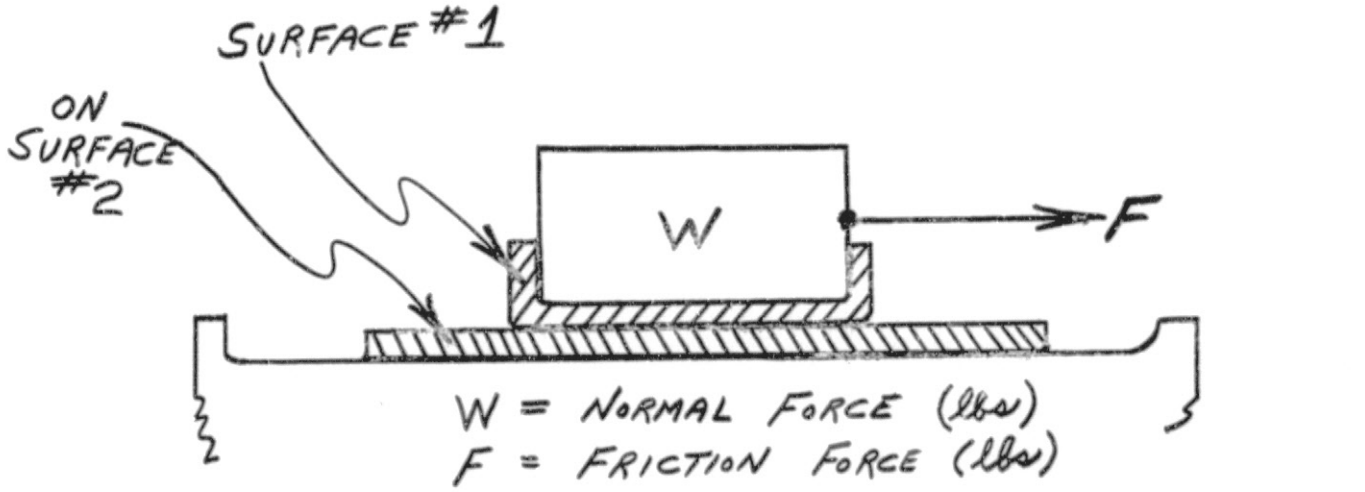

The results of this testing are summarized in Table III-3. The coefficients of static friction are given along with the test pressure (g/in^2) for each material combination.

TABLE III-3

		On Surface #2						
		Negative Plate Screen Side	Negative Plate Slurry Side	Wax Paper	Teflon Sheet	Pellon *	Positive Plate Screen Side	Positive Plate Slurry Side
SURFACE #1	Negative Plate Screen Side	0.71 (615)	0.57 (870)	0.13 (870)	0.25 (440)	0.64 (680)		
	Negative Plate Slurry Side		0.53 (870) 0.81 (124)	0.40 (440)	0.30 (440) 0.25 (112)	0.69 (635) 0.10 (22)		
	Positive Plate Screen Side			0.10 (870)	0.14 (870)	0.74 (590)	0.35 (440)	0.35 (440)
	Positive Plate Slurry Side			0.15 (440)	0.18 (440) 0.28 (112)	0.62 (705) 0.10 (21)		0.30 (440) 0.30 (112)

* Entire System Saturated with KOH

D. Dynamic Response of Elements to Impact Loading

(a) Development of Strain Gage Techniques

The measurement of Poisson's ratio made it necessary to employ resistance strain gages early in our testing program (8th JPL QTR Report Pg III-48). Some of the experimental difficulties in using these gages on a porous battery electrode were discussed. Further development of this technique was necessary before dynamic strain measurements could be made under impact conditions. This report will briefly outline our comparitive study of gages and techniques.

Several gages were chosen for study since various types (BLH) are manufactured differently and are compatible with various cements. We expect different behavior from these combinations in terms of degree of reinforcement and elongation range. The various combinations and gage characteristics are shown in Table III-4. Two gages of each type were cemented with each compatible adhesive on negative plate tensile specimens. Negative plate material is weaker than positive and tension loading more acurately demonstrates

TABLE III-4

		GAGE TYPE				
		PA-7	FAE 25 12 P	FAP 12 12 S6	AF 7 1 S6	C8
Gage Length	1/8 Inch			X		X
	1/4 Inch	X	X		X	
Grid Material	Constantan	X	X	X	X	
	Isolastic					X
Grid Properties	Regular			X	X	X
	Post-Yield (annealed)	X	X			
Grid Shape	Wire	X			X	X
	Foil		X	X		
Backing Material	Regular Paper					X
	Thin Paper	X		X	X	
	Epoxy Film		X			
Cements	SR-4	XX		XX	XX	X
	E-910	X	XX	X	X	

the failures and elongation limits of accurate strain output. Each specimen was placed in a universal testing machine and loaded in quasi-static tension. Load cell output (stress) and strain output from both the strain gage and a conventional extensometer were simultaneously recorded on an X-Y plotter. We could thus compare the strain reading from the strain-gage (ϵ_G) to the reading from the extensometer (ϵ_E) at any given stress level. Table III-5 summarizes the results of this study and gives the observed ratio strain-gage reading to extensometer reading (ϵ_G: ϵ_E) for the applicable strain (ϵ_E) range. The "FAP" gage seems to possess the least reinforcement and fairly consistant results in a good portion of the elastic region, especially when used with E-910. The "AF-7" gage seems to be very consistant at higher strain levels when used with either SR-4 or E910 although its output ratio seems quite low.

A second series of tests were performed with the same specimens. $\sigma-\epsilon$ curves had been obtained earlier (8th QTR JPL Fig. III-C) and a modulus of elasticity reported $E = 1.0 \pm 0.1 \times 10^6$ psi. Thus, dead weight loading was employed (stress) and the strain-gage reading was recorded. We could thus compare the strain-gage reading to the strain value taken from the curve at each stress level. Furthermore we could compare this experimental $\sigma-\epsilon$ slope to the more accurate value of modulus determined earlier. Table III-6 summarizes the results of this study. It appears that the three techniques represented by specimens 4, 7, 9 show considerable promise. The $\sigma-\epsilon$ curve shows a significant plastic deformation beyond the 1000 $\mu\epsilon$ point yet technique 9 remains bothersome in the lower stress limit

TABLE III-5

Ratio $\epsilon_G : \epsilon_E$ for Quasi-Static Tensile Loading

	Gage Type	Adhesive	Specimen #	Output Ratio & Strain Limit
	PA 7	SR-4 SR-4 910 910	1A 1B 2A 2B	12 ($20\mu\epsilon_E$) 2.5 ($45\mu\epsilon_E$) 0.5 ($200\mu\epsilon_E$)
	FAE 25 12 P	910 910	3A 3B	3.5 ($45\mu\epsilon_E$) 0.5 ($> 300\mu\epsilon_E$)
	FAP 12	SR-4 SR-4	4A 4B	0.38 ($> 500\mu\epsilon_E$)
*	12 S6	910 910	5A 5B	0.52 ($620\mu\epsilon_E$)
	AF 7 1	SR-4 SR-4	6A 6B	3.4 ($100\mu\epsilon_E$) 0.98 ($375\mu\epsilon_E$) 0.2 ($> 1375\mu\epsilon_E$ 1.8 ($100\mu\epsilon_E$) 0.61 ($400\mu\epsilon_E$)
*	S6	910 910	7A 7B	1.8 ($100\mu\epsilon_E$) 0.61 ($300\mu\epsilon_E$) 0.17 ($> 520\mu\epsilon_E$) 0.21 ($3600\mu\epsilon_E$)
	C8	Duco	8	15 ($20\mu\epsilon_E$) 2.1 ($100\mu\epsilon_E$) 0.5 ($> 520\mu\epsilon_E$)
		SR-4 SR-4	9A 9B	1.8 ($50\mu\epsilon_E$) 0.18 ($200\mu\epsilon_E$) 0.8 ($90\mu\epsilon_E$) 0.45 ($360\mu\epsilon_E$)
		910	10	2.6 ($35\mu\epsilon_E$) 0.11 ($240\mu\epsilon_E$)

TABLE III-6

Ratio $\varepsilon_G : \varepsilon_{CURVE}$ FOR DEAD WEIGHT LOADING

	Specimen #	Ratio $\varepsilon_{Gage} : \varepsilon_{\sigma-\varepsilon\ curve}$ @ $\varepsilon_{\sigma-\varepsilon}$ Level curve					E $X10^6$ PSI $\sigma - \varepsilon$ gage (stress limit) PSI
		@ 75 $\mu\varepsilon_c$	@ 250 $\mu\varepsilon_c$	@ 450 $\mu\varepsilon_c$	@ 950 $\mu\varepsilon_c$	@ 2700 $\mu\varepsilon_c$	
	1A	Shorted					
	1B	1.96	1.52	1.34	0.89	0.32	0.65 (550)
	2A	0.29	0.32	0.30	0.2	0.1	2.95 (700)
	2B	1.07	0.78	0.73	0.43	0.19	1.20 (500)
	3A	--	0.34	0.30	0.21	0.10	2.70 (650)
	3B	1.12	0.72	0.75	0.49	0.22	1.19 (>700)
*	4A	1.05	0.64	0.63	0.43	0.20	1.33 (700)
	4B	1.14	0.89	--	0.55	0.23	1.04 (650)
	5A	0.67	0.58	0.49	--	0.15	1.70 (700)
	5B	0.93	0.68	0.65	--	0.19	1.35 (650)
	6A	1.4	1.3	1.2	--	0.33	0.71 (500)
	6B	1.24	1.25	1.18	0.75	0.32	0.75 (600)
*	7A	1.0	0.76	0.72	0.45	0.2	1.2 (600)
	7B	1.16	0.87	0.80	0.53	0.23	1.1 (> 700)
†	8	2.66	2.11	--	1.3	0.59	0.44 (> 700)
*	9A	1.15	1.12	1.0	0.62	0.28	0.87 (500)
	9B	1.5	1.13	1.1	0.65	0.24	0.81 (450)
	10	0.84	0.61	0.56	0.34	0.15	1.52 (450)

capability. Techniques 4 and 7 seem to have good reproducibility, ratio values, modulus values and high stress limits. Thus 4 and 7 were the two techniques selected for subsequent strain measurements reported in a later section. Additional work in this area should look at these two techniques under compression loading. There is good reason to suspect that this will be less severe than the tension loading used for initial screening. The strain limits are likely to be elevated and it is important to measure the compression modulus of elasticity.

(b) Theoretical Predictions of Dynamic Response

(1) One-degree of freedom analysis of natural frequency:

The natural frequencies, f_{N_n}, of a vibrating system or element are a most important parameter in the study of the transient as well as the steady state response of that system. Therefore, our preliminary analysis effort was directed toward a modified single degree of freedom approach to approximate the natural frequencies of our system. With this approximation, we could then examine the consequences of the value of f_{N_1} so obtained with respect to the shock spectra of the specified deceleration pulse.

The single degree of freedom system employed is shown below:

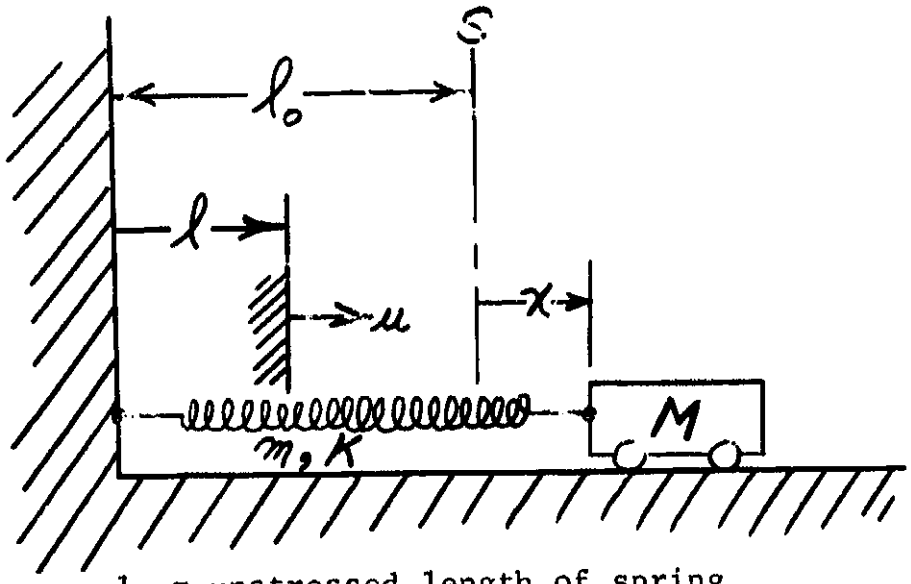

l_o = unstressed length of spring

S = static equilibrium position

x = dynamic displacement of body

M = Mass of body

l = length along spring

u = dynamic displacement of dl

m = mass of spring

K = spring constant

This system permits the mass of the spring to be considered and $\omega_{N_1} \neq \sqrt{\frac{K}{M}}$ as in the simple case. Thus we can use this system to reduce our distributed - mass (infinite degree-of-freedom) element (battery electrode) to a lumped - parameter system utilizing the concept of vibrational transfer of potential and kinetic energy. This method has been accurately described in the literature and for this system it has been shown that the natural frequency (undamped) is:

$$\omega_{N_1} = \frac{\pi}{2}\sqrt{\frac{K}{2M + m}} \quad \text{for } M \ll m$$

(Rad./Sec.)

The accuracy of this equation is shown by the absurd assumption that $m \rightarrow 0$ while M remains finite. Application of the equation to this situation gives

an error in ω_{N_1} that is only 11% too high.

Thus if $M \longrightarrow 0$, we have the case of a spring alone without concentrated end mass and:

$$\omega_{N_1} \approx \frac{\pi}{2}\sqrt{\frac{K}{m}} \qquad \text{for } M = 0$$

or for our elastic spring element of length, l, apparent cross sectional area, A, and apparent modulus of elasticity, E, we have:

$$K = \frac{AE}{l}$$

and:

$$\omega_{N_1} \approx \frac{\pi}{2}\sqrt{\frac{AE}{lm}}$$

or:

$$f_{N_1} = \frac{\omega_{N1}}{2\pi} \approx \frac{1}{4}\sqrt{\frac{AE}{lm}} \qquad \text{(cy/sec)}$$

Now for battery electrodes we may write for convenience:

$$A = \text{width} \times \text{thickness} = wt$$

$$m = \frac{\text{weight}}{g} = \frac{\text{length x width x area density}}{g} = \frac{l \cdot w \cdot \rho}{g}$$

where: ρ = area weight density

and:

$$f_{N_1} = 1/4\sqrt{\frac{w \cdot t \cdot E \cdot g}{l \cdot l \cdot w \cdot \rho}}$$

or

$$f_{N_1} = C\sqrt{\frac{E}{l}} \qquad \text{Where: } C = 1/4\sqrt{\frac{t \cdot g}{\rho}}$$

Specifically for our Ni-Cd electrodes:

t = thickness (.025" - .028") = 0.0265 in.

g = acceleration of gravity = 386 in./sec^2

ρ = area weight density = 3.2×10^{-3} #/in^2

($2.8\text{-}3.2 \times 10^{-3}$ #/in^2 positive)

($3.3\text{-}3.5 \times 10^{-3}$ #/in^2 negative)

Variables:

E = modulus of elasticity

0.1×10^6 psi negative plate in compression

1.0×10^6 psi positive plate in tension

l = length of electrode

normally 3" - 8"

Thus: C = 14

and the fundamental frequency of longitudinal vibration for sintered Ni-Cd electrodes is given by:

$$f_{N_1} = (14)\frac{\sqrt{E}}{l}$$

This fundamental natural frequency has been calculated for various plate lengths and values of E and is plotted in Figure III-10.

(2) Shock Spectra Implications:

A shock spectrum is a plot showing the peak response of a variable - frequency, single degree of freedom oscillator to a specific shock pulse as a function of the natural frequency of the oscillator. It is important to understand from the start, that the shock spectrum tells us what A shock pulse will Do not what it is. This is much different than a Fourier spectrum or plot of the Fourier analysis performed to describe a given shock pulse. It is appropriate to consider a row of n mass-spring elements mounted on a horizontal base which will receive a specific shock pulse. If each oscillator has a different natural frequency $\left(f_{N_1} = \frac{1}{2\pi}\sqrt{\frac{K}{M}}\right)$ and we

FIGURE III-10

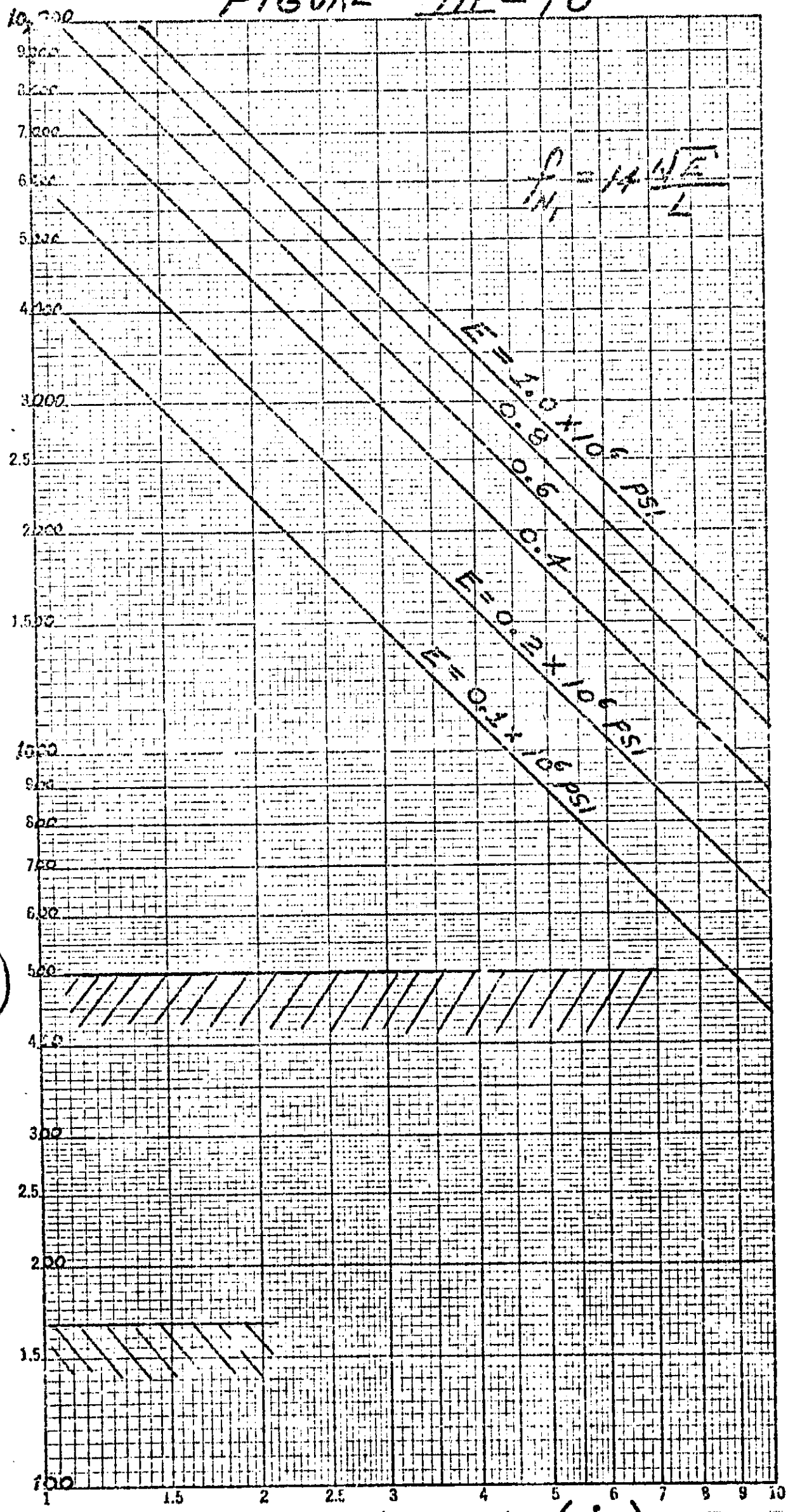

could attach a pen to each mass, we would obtain n values of peak response which related to the input base displacement would allow us to plot a relative-response vs. natural frequency curve or the shock spectrum for that pulse. It has been found that when a signle degree of freedom, linear, undamped system with a distinct natural frequency is subjected to a mechanical shock, its response or resultant motion will be determined by the magnitudes, shape, and time duration of the shock pulse. In fact, the amplification spectrum as it is sometimes called, is rather insensitive to the exact time-history of the pulse. Rather, the rise-time of a given pulse is the most important factor which distinguishes the maximum amplification factors for various pulse shapes. The total impulse and rise time are the two main damage criteria. As will be seen, the rapid rise time of our square pulse implies the highest maximum value of any pulse shape (theoretically = 2X). In general, the shock spectrum will not have frequency alone as the abcissa because of the above considerations, rather a ratio of the shock pulse length (t_o) to the natural period of the oscillator (T) is more useful ($\frac{t_o}{T}$). Depending on the value of this ratio, however, we find that the system's response <u>during</u> application of a given shock pulse may differ considerably from the motion <u>after</u> the shock pulse had ended ($t = t_o$). It is therefore common to plot a "primary" spectrum (response during shock input ($o < t < t_o$) and a "residual" spectrum (response after shock input $t_o < t < \infty$) to fully generalize the behavior of various elements to various shock durations of a certain pulse shape. However, it is more useful to provide the designer of shock-resistant elements with a

single "maxi ax" spectrum plot arrived at by taking the greater value from the "primary" or the "residual" plots throughout the frequency ratio range of interest.

It is not appropriate to reiterate the derivations and analyses of various spectra characteristics that can be found in the literature. The value of using this consept is well recognized and it is only important that we understand the fundamentals in order to apply the information that can be obtained. Thus the character of the maximax shock spectra can be obtained directly from the literature. In our case, we wish to consider a <u>single</u> shock input:

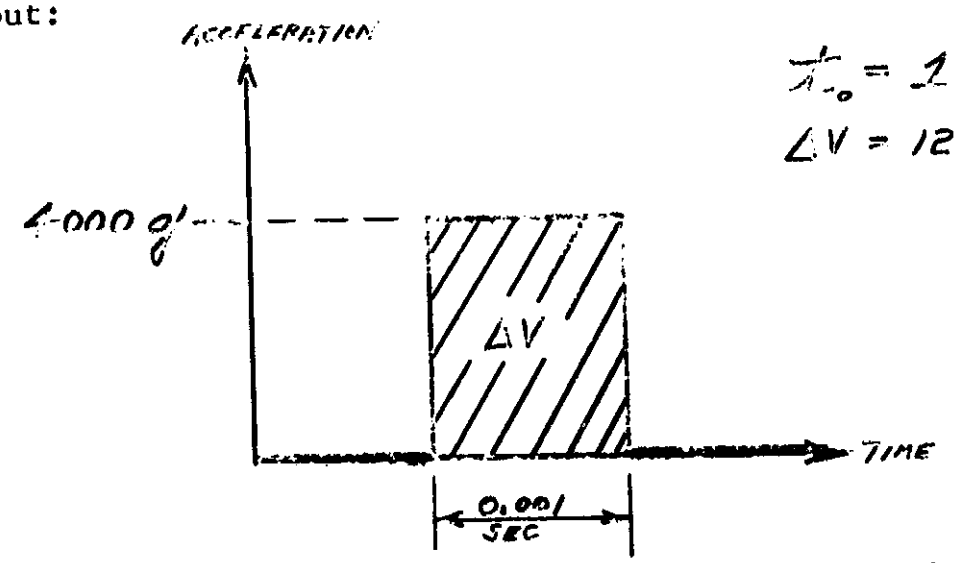

Thus we can establish the abscissa directly as the natural frequency of our Ni-Cd electrodes rather than as a time ratio.

The ordinate is simply the relative response and can be scaled directly in numerical <u>dynamic amplification factors</u>. It must be remembered that the response can be thought of as displacement, acceleration, etc. (The same quantity describing the input pulse). More useful to the designer is the concept of force or stress (indirectly strain) amplification over that of a

static loading equal to the amount of input acceleration.

The shock spectrum for the pulse illustrated above is given in Fig. III-11 with the ordinate and abcissa scaled as discussed for optimum use in our problem. The basic implications are: (1) Any Ni-Cd electrode with a natural frequency greater than 167 cy/sec will experience an amplification of the nominal input forces under dynamic loading. (2) Any Ni-Cd electrode with a natural frequency greater than 500 cy/sec will experience twice the nominal input forces under this dynamic loading situation.

From a design point of view, the calculation of natural frequencies in the previous section now has more value. It may be instructive to outline the design considerations that have been formulated:

(1) The manner of loading must first be identified and this will dictate the modulus of elasticity and strain-rate effects from previous determinations of the mechanical properties of our electrode.

(2) Space considerations may indicate a trial size of our electrode.

(3) The design pluse magnitude will be used to calculate the static stress applied to this size and weight electrode.

(4) The natural frequency of this specific electrode is determined.

(5) The shock spectrum (for the design pulse) is used to determine the dynamic amplification factor which applies.

(6) The actual stress which this electrode will experience under this design pulse loading can now be calculated.

(7) The effect of this stress on the electrode is now determined from

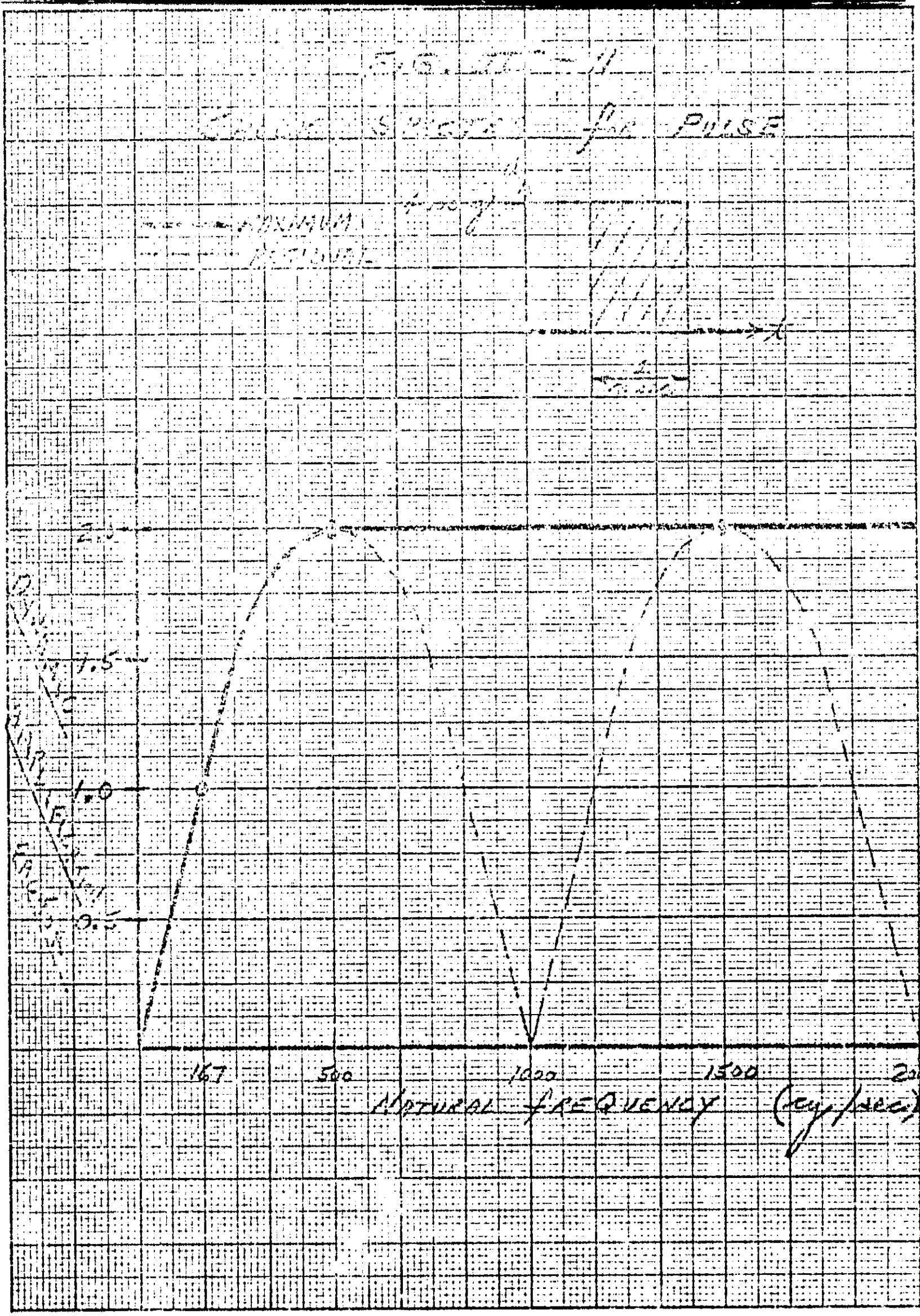

previous determinations of this electrode's mechanical properties under the same manner of loading.

The importance of determining complete experimental information concerning the mechanical properties of Ni-Cd electrodes is now obvious. Without such information, design can neither begin (step 2) nor can a valid judgement be made (step 7) concerning the actual damage that may or may not occur to an electrode in a specific loading situation.

(3) Analysis of Displacement and Stress for Distributed - Mass element:

The frequency-shock spectra analysis is quite straightforward and can provide valuable information to the designer. It does not permit a direct calculation of the stress within the element, however, and it does not give us a description of the deformation process. What we would like is an insight into the actual displacements within an electrode and the stresses that are applied during impact. We seek an accurate description of stress and strain as a function of location and time. This type of information can only be obtained by a more rigorous analysis of our distributed - mass element. To explore the possibility of solution, we have formulated the problem as a long slender element of uniform cross sectional area, A, and constant initial velocity (rigid body motion),-V, which is subjected to a sudden longitudinal deceleration at time t = o. The problem is shown below:

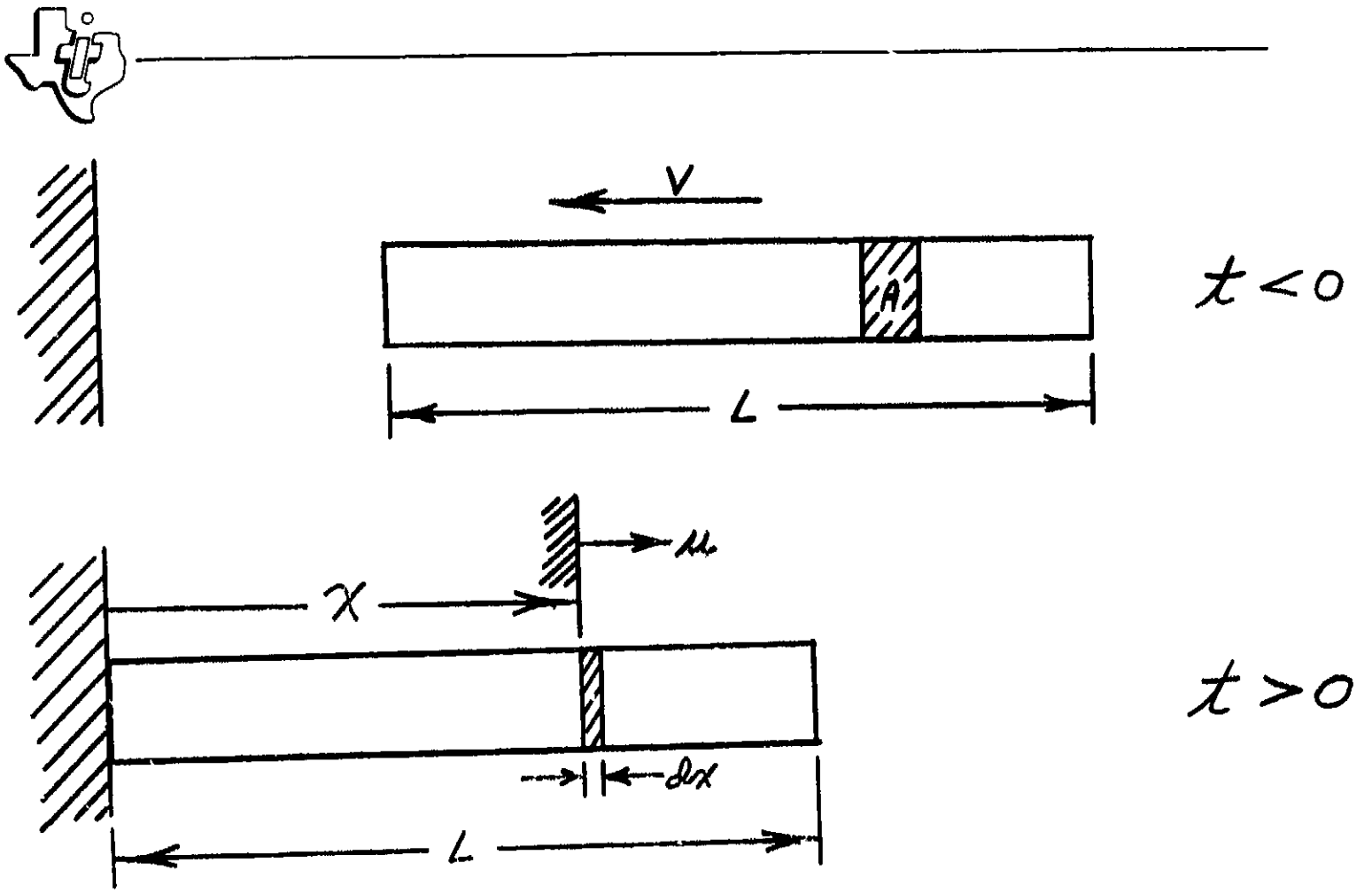

We may write a balance of forces for a mass element dx:

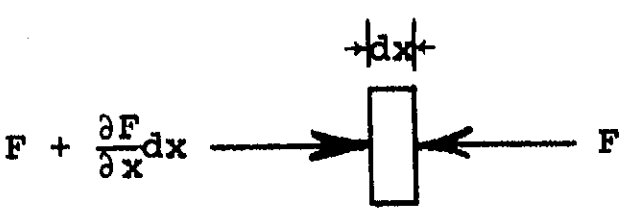

$$\Sigma F = ma$$

$$\left(F + \frac{\partial F}{\partial x}\,dx\right) - F = \left(\frac{A\gamma dx}{g}\right)\frac{\partial^2 u}{\partial t^2}$$

$$\frac{\partial F}{\partial x} = \left(\frac{A\gamma}{g}\right)\frac{\partial^2 u}{\partial t^2} \qquad (1)$$

where: $A \cdot dx$ = volume
γ = volume weight density
g = acceleration of gravity
$\frac{\partial u}{\partial t}$ = velocity of element

We can now introduce the assumption of elastic material behavior:

$$F = \sigma A$$
$$F = (\varepsilon E)A$$
$$F = \frac{\partial u}{\partial x} EA$$
$$\frac{\partial F}{\partial x} = EA\,\frac{\partial^2 u}{\partial x^2}$$

where: σ = stress
$\varepsilon = \frac{\partial u}{\partial x}$ = strain
E = modulus of elasticity

Now EQ. (1) becomes:

$$\frac{\partial^2 u}{\partial x^2} = \left(\frac{\gamma}{Eg}\right) \frac{\partial^2 u}{\partial t^2}$$

or:

$$\frac{\partial^2 u}{\partial t^2} = a^2 \frac{\partial 2u}{\partial x^2} \qquad (2)$$

which is the general "wave equation" in which:

$$a = \sqrt{\frac{Eg}{\gamma}} = \sqrt{\frac{E}{\rho}} \quad \text{where: } \rho = \text{mass density}$$

and a is the velocity of elastic strain wave travel in this material.

We have for our case:

Initial Conditions	Boundary Conditions
$u\ (x,o) = o$	$u\ (o,t) = o$
$\frac{\partial u}{\partial t}\ (x,o) = -V$	$\frac{\partial u}{\partial x}\ (L,t) = o$

imposed by our considerations of constant initial velocity, rigid fixed end and free unstressed end.

Following the method of separation of variables we assume the general solution of EQ.(2) may have the form:

$$u\ (x,t) = X\ (x)\ T(t) \qquad (3)$$

$$\Longrightarrow \frac{\partial^2 u}{\partial t^2} = X\ T'' \quad \& \quad \frac{\partial^2 u}{\partial x^2} = T\ X''$$

where: X & T are functions of x & t alone and " denotes total (not partial) differentiation

Now we may write EQ.(2) as:

$$X\ T'' = a^2\ T\ X''$$

$$\frac{T''}{T} = a^2 \frac{X''}{X} = \mu$$

$$T'' = \mu T \qquad X'' = \frac{\mu}{a^2}\ X$$

Now if $\mu<o$ (as it must for periodic solution), we can write

$$\mu = -\lambda^2$$

and the component ordinary differential equations will be:

$$T'' = -\lambda^2 T \qquad \& \qquad X'' = -\frac{\lambda^2}{a^2} X$$

and whose solutions are known:

$$T = A \cos \lambda t + B \sin \lambda t$$

&

$$X = C \cos \frac{\lambda}{a} x + D \sin \frac{\lambda}{a} x$$

Therefore, the general product solution EQ.3 can be written:

$$u(x,t) = (C \cos \frac{\lambda}{a} x + D \sin \frac{\lambda}{a} x)(A \cos \lambda t + B \sin \lambda t) \quad (4)$$

Now we may begin to evaluate the constants by examining the first boundary condition in EQ.(4):

$$O = C\ (A \cos \lambda t + B \sin \lambda t)$$

$$\Longrightarrow C = O \text{ in general for all } t$$

Examining the second boundary condition in EQ.(4):

$$\left(\frac{\partial u}{\partial x}\right)_{x=L} = (D \frac{\lambda}{a} \cos \frac{\lambda}{a} L)(A \cos \lambda t + B \sin \lambda t) = O$$

$$\Longrightarrow (D \frac{\lambda}{a}) \cos \frac{\lambda}{a} L = O \quad \text{in general for all } t$$

$$\therefore \cos \frac{\lambda}{a} L \overset{\text{must}}{=} O$$

$$\Longrightarrow (\frac{\lambda}{a} L) = \frac{(2n-1)}{2} \pi \qquad n = 1,2,3,.....$$

Hence: $$\lambda_n = \frac{(2n-1)\ a\pi}{2L} \qquad n = 1,2,3,.....$$

Now the general solution EQ.(4) has been reduced but contains the series of added product solutions and can be written:

$$u\ (x,t) = \sum_{n=1}^{\infty} \sin \frac{(2n-1)\pi}{2L} x \left[A_n \cos \frac{(2n-1)\pi a}{2L} t + B_n \sin \frac{(2n-1)\pi a}{2L} t\right] \quad (5)$$

where: A_n and B_n are not formally the same constants as A and B in EQ.(4) and must now be evaluated from our initial conditions.

Examining the first initial condition in EQ.(5):

$$0 = \sum_{n=1}^{\infty} A_n \sin \frac{(2n-1)\pi}{2L} x$$

$$\Longrightarrow A_n = 0 \quad \text{in general for all } x$$

Examining the second initial condition in EQ.(5):

$$\left.\frac{\partial u}{\partial t}\right)_{t=0} = \sum_{n=1}^{\infty} B_n \left(\frac{(2n-1)\pi a}{2L}\right) \sin \frac{(2n-1)\pi}{2L} x = -V \qquad (6)$$

We recognize a similarity between EQ.(6) and a half-range Fourier Series expansion. We know that if some f(t) is an odd periodic function, then the coefficients in the Fourier Series of f(t) are:

$$a_n = 0 \quad ; \quad b_n = \frac{2}{p} \int_0^p f(t) \sin \frac{n\pi t}{p} \, dt$$

Hence, the problem of determining B_n in EQ.6 is really the problem of expanding the given function f(x) in a half-range sine series expansion over the interval $0<x<L$.

Repeating EQ. 6:

$$f(x) = -V = \sum_{n=1}^{\infty} \left[\frac{(2n-1)\pi a}{2L} B_n\right] \sin \frac{(2n-1)\pi}{2L} x$$

Requires that the groups

$$\left[\frac{(2n-1)\pi a}{2L} B_n\right]$$

will be the coefficients of the half-range sine expansion of the known function f(x).

Thus from:

$$b_n = \frac{2}{p} \int_0^p f(t) \sin \frac{n\pi t}{p} \, dt$$

we can write (taking $p \equiv L$):

$$\left[\frac{(2n-1)\pi a}{2L} B_n\right] = \frac{2}{L} \int_0^L f(x) \sin \frac{(2n-1)\pi x}{2L} dx$$

or:

$$B_n = \frac{4}{(2n-1)\pi a} \int_0^L (-V) \sin \frac{(2n-1)\pi x}{2L} dx \qquad (7)$$

and performing the required integration:

$$B_n = \left[\frac{-8\ VL}{(2n-1)^2\ \pi^2\ a}\right] \qquad (8)$$

Now we may write the final general equation for displacement from EQ. 5:

$$u\ (x,t) = \sum_{n=1}^{\infty} \sin \frac{(2n-1)\pi}{2L} x \left[\frac{-8\ VL}{(2n-1)^2 \pi^2\ a} \sin \frac{(2n-1)\pi a}{2L}\ t\right]$$

or:

$$u\ (x,t) = \frac{-8\ VL}{a\ \pi^2} \sum_{n=1}^{\infty} \frac{1}{(2n-1)^2} \sin \frac{(2n-1)}{2} \pi \frac{x}{L} \sin \frac{(2n-1)}{2} \pi \frac{at}{L} \qquad (9)$$

which now fully describes the elastic displacement at any time and any longitudinal location along the electrode.

We see immediately that:

$u\ (x,t) = 0$ @ $x = 0$ for all t

$u\ (x,t) = 0$ @ $t = 0$ for all x

$u\ (x,t) =$ max. @ $x = L$ for any t

$u\ (x,t) =$ max. @ $t = {}^{L}/_{a}$ for any x

We know further that the natural frequencies of this sinusoidal displacement u(t) or vibration are:

$$f_{N_n} = \frac{\lambda n}{2\pi} \quad \text{(cycles/sec)} \quad n = 1,2,3,.....$$
$$= \frac{(2n-1)\ a\pi}{(2\pi)\ 2L}$$

therefore:

$$f_N = 1\ (\tfrac{a}{4L}),\ 3\ (\tfrac{a}{4L}),\ 5\ (\tfrac{a}{4L}),\ \ldots\ldots\ldots\ldots \qquad (10)$$

Examining the fundamental natural frequency:

$$f_{N_1} = \frac{a}{4L} = \frac{\sqrt{E/\rho}}{4L} = \frac{\sqrt{Eg/\gamma}}{4L} = \tfrac{1}{4}\sqrt{\frac{tg}{\rho}}\frac{\sqrt{E}}{L}$$

We find that it is equivalent to the "approximation" we had obtained earlier in Section III-D, (b), (1) in our consideration of the single degree of freedom system. This is not actually surprising since the earlier approximation employed sine functions as "guesses" for both the normal function and the time function. This means now that Figure III-10 gives us the true natural frequency, f_{N_1}, as confirmed by a rigorous analysis.

Having obtained a complete solution (EQ. 9) for elastic displacement, we can now investigate the general stress solution since:

$$\frac{\partial u(x,t)}{\partial x} = \varepsilon$$

and:

$$\sigma = E \left(\frac{\partial u}{\partial x}\right)$$

Since we have made the initial assumption of elastic material behavior.

Therefore:

$$\sigma\ (x,t) = E \left(\frac{-8\ VL}{a\pi^2}\right) \sum_{n=1}^{\infty} \frac{1}{(2n-1)^2} \sin \frac{(2n-1)\pi a}{2L}\ t \cos\frac{(2n-1)\pi}{2L} x \left(\frac{(2n-1)\pi}{2L}\right)$$

and the general stress solution is:

$$\sigma\ (x,t) = \frac{-4EV}{a\pi} \sum_{n=1}^{\infty} \frac{1}{(2n-1)} \cos \frac{(2n-1)}{2} \pi \frac{x}{L} \sin \frac{(2n-1)}{2} \pi \frac{at}{L} \qquad (11)$$

which fully describes the elastic stress within the element at any time and any longitudinal location along the electrode.

We see immediately that:

$\sigma\ (x,t) \neq 0$ @ $x = L$ for all t

$\sigma\ (x,t) = 0$ @ $t = 0$ for all x

$\sigma\ (x,t) = \max$ @ $x = 0$ for any t

$\sigma\ (x,t) = \max$ @ $t = L/a$ for any x

We can also note that the higher modes are of much greater consequence in determining the stress than in determining the displacement.

Observe that:

$$u \equiv \sum_{n=1}^{\infty} \frac{1}{(2n-1)^2} (-1,0,+1) \equiv (\frac{1}{1} + \frac{1}{9} + \frac{1}{25} + \frac{1}{49} + \ldots)$$

$$\sigma \equiv \sum_{n=1}^{\infty} \frac{1}{(2n-1)} (-1,0,+1) \equiv (\frac{1}{1} + \frac{1}{3} + \frac{1}{5} + \frac{1}{7} + \ldots\ldots)$$

Nevertheless, we assume convergence and note for future calculations that:

$$1 + \frac{1}{9} + \frac{1}{25} + \frac{1}{49} + \ldots\ldots = \frac{\pi^2}{8}$$

and: $1 - \frac{1}{3} + \frac{1}{5} - \frac{1}{7} + \ldots\ldots = \frac{\pi}{4}$

are both convergent series.

We are interested in the expression for maximum stress which occurs at the fixed end (x = 0):

$$\sigma_{\underline{max.}}(0,t) = \frac{-4EV}{a\pi} \sum_{n=1}^{\infty} \frac{1}{(2n-1)} \sin \frac{(2n-1)}{2} \pi \frac{at}{L} \qquad (12)$$

Numerical Analysis:

Currently in this phase of our contract we have been unable to use a computer to fully analyze the implications of our equations (9) and (11) describing displacement and stress. This should be done for many combinations of x and t values in order to understand their physical meaning more fully. We have, during this completion phase of the contract however, attempted to numerically evaluate the maximum stress (EQ. (12)) for a few values of time, t.

@ t = 0:

$$\sigma_{x=o} = \frac{-4EV}{a\pi} (0 + \frac{1}{3}(0) + \frac{1}{5}(0) + \frac{1}{7}(0) + \ldots\ldots) = 0$$

@ t = L/2a:

$$\sigma_{x=o} = \frac{-4EV}{a\pi} ((.707) + \frac{1}{3}(.707) + \frac{1}{5}(-.707) + \ldots\ldots)$$

$$= \frac{-4EV}{a\pi} \quad (+.757)_{n=1\ldots12}$$

$$\approx \frac{-4EV}{a\pi} \left(\frac{\pi}{4}\right)$$

@ $t = \frac{L}{a}$:

$$\sigma_{x=o} = \frac{-4EV}{a\pi} \left(1 + \frac{1}{3}(-1) + \frac{1}{5}(+1) + \frac{1}{7}(-1) + \ldots\ldots\right)$$

$$= \frac{-4EV}{a\pi} \quad (.764)_{n=1\ldots12}$$

$$= \frac{-4EV}{a\pi} \left(\frac{\pi}{4}\right) \qquad \text{exactly}$$

@ $t = \frac{3L}{2a}$:

$$\sigma_{x=o} = \frac{-4EV}{a\pi} \ (.757)_{n=1\ldots12} \qquad \text{same as } t = \frac{L}{2a}$$

$$\approx \frac{-4EV}{a\pi} \left(\frac{\pi}{4}\right)$$

@ $t = \frac{2L}{a}$

$$\sigma_{x=o} = \frac{-4EV}{a\pi} \ (0) = 0$$

from $t = \frac{2L}{a}$ to $t = \frac{4L}{a}$ all values are identical except for sign reversal.

It is apparent then that we have simply the summation of the fundamental and all the odd sinusoidal harmonics which is of course a square wave. The coefficients of the odd harmonies appear to imply a $\frac{\pi}{4}$ multiplier for the fundamental. We can sketch the first three modes:

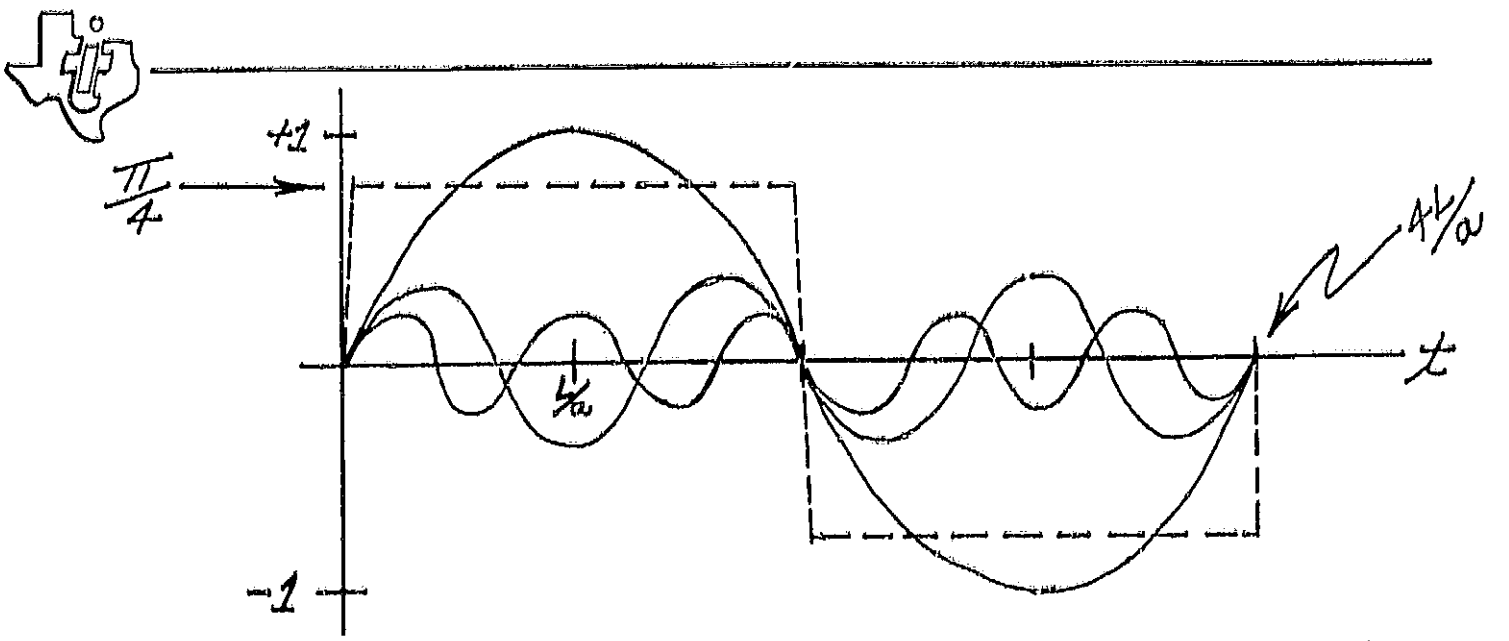

and diagrammatically show the stress wave propagation as follows:

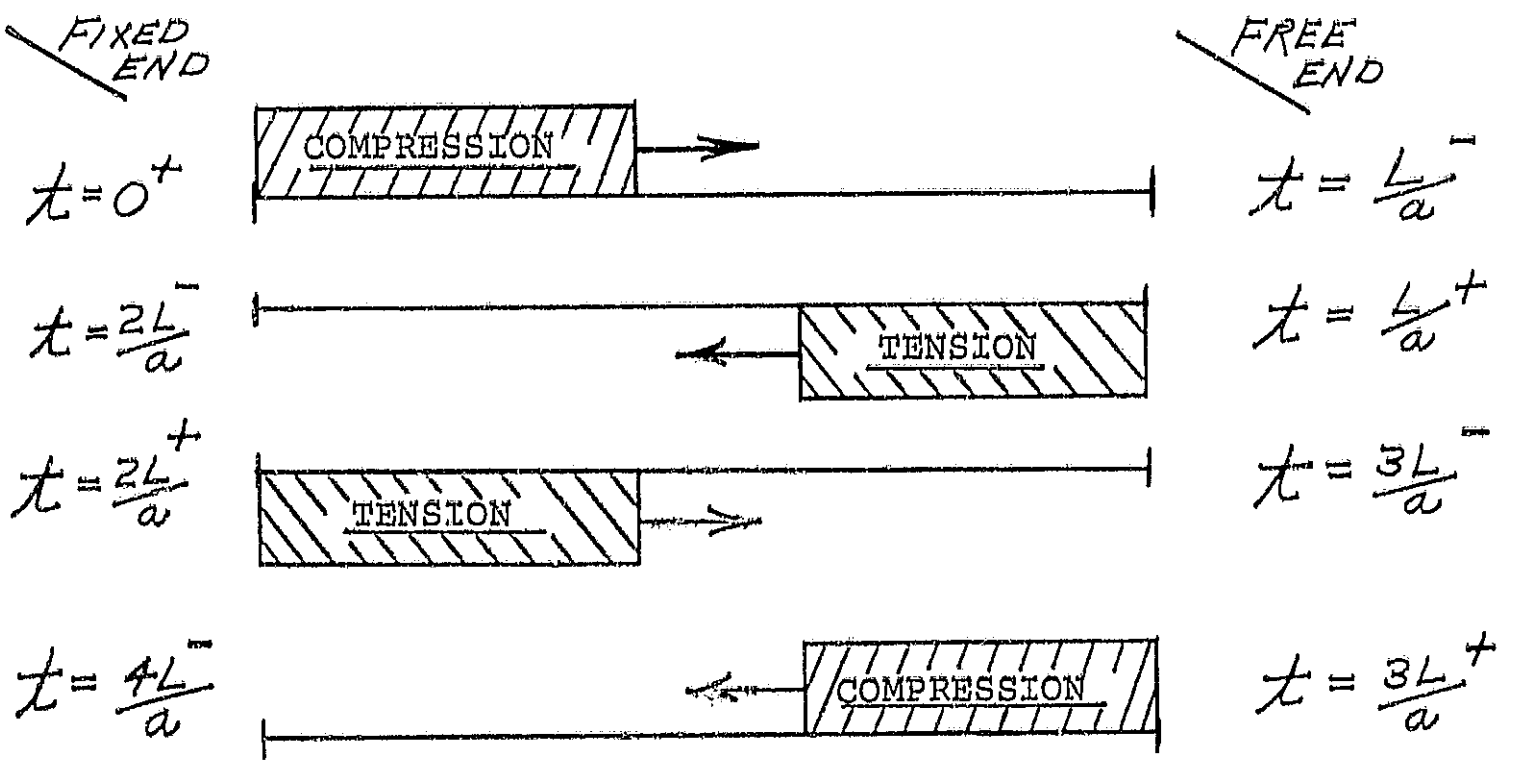

This indicates that at the fixed end where stress is a maximum, we have a state of compression for the time interval $0<t<\frac{2L}{a}$, followed by a state of tension for the time interval $\frac{2L}{a} < t < \frac{4L}{a}$. This process is then cyclic at a frequency of $(\frac{a}{4L})$ cycles/sec.

Conclusion:

In this section (3), we have given a complete solution which when coupled with a high speed computer and the proper values of E, a, V, will provide a full evaluation of the elastic displacements and stresses within any element at all locations and

and times. The sole limitation of this general solution, of course, is the one assumption that made the solution possible -- elastic material behavior. If we do not impose this material limitation and allow stress to be some general function of strain however, we do not obtain EQ.(2) as the governing differential equation.

Rather:

$$\frac{\partial F}{\partial x} = \left(\frac{A\gamma}{g}\right) \frac{\partial^2 u}{\partial t^2} \qquad (1)$$

Holds as before, but in general:

$$\sigma = f(\varepsilon)$$

and we have:

$$\frac{\partial \sigma}{\partial x} = \left(\frac{\gamma}{g}\right) \frac{\partial^2 u}{\partial t^2}$$

now: $$\frac{\partial \sigma}{\partial x} = \frac{\partial \sigma}{\partial \varepsilon} \cdot \frac{\partial \varepsilon}{\partial x} = \frac{\partial \sigma}{\partial \varepsilon} \cdot \frac{\partial \left(\frac{\partial u}{\partial x}\right)}{\partial x} = \frac{\partial \sigma}{\partial \varepsilon} \left(\frac{\partial^2 u}{\partial x^2}\right)$$

and

$$\frac{\partial \sigma}{\partial \varepsilon} \left(\frac{\partial^2 u}{\partial x^2}\right) = \rho \frac{\partial^2 u}{\partial t^2} \qquad (13)$$

whose general solution has not been obtained. EQ.(13) therefore introduces the most significant portion of non-linearity into our system. We understand that JPL has devoted some effort to the treatment of this and large displacement non-linearities. Recent literature has discussed ways of introducing empirically the non-linearities implied by plastic and strain hardening behavior. This area is in need of further analysis. If the current work were continued, the research indicated for a more complete understanding of dynamic response is in the introduction

of these material behavior non-linearities into the general governing differential equation (13) and the physical interpretation of its solution with the aid of computer analysis.

One further point does not concern the validity of the solution given, but concerns the exactness of its applicability to our experimental loading situation. In question is the first boundary condition which was used in our solution to describe the rigid fixed end:

$$u\ (o,t) = 0$$

If time permits, we should go back and examine the effect on our solution of imposing a condition of uniform deceleration during the time interval of impact:

$$u(o,t) = -Vt - \frac{a}{2} t^2 \qquad o<t<.001/sec.$$

This may more accurately describe the displacement of this end of the bar during the time of loading and could thus make the existing solution conservative in its prediction of stresses which may be higher than those actually experienced in our testing.

(c) Experimental Determinations of Dynamic Response

(1) High Speed Photographic Analysis

Following an analysis or theoretical prediction of mechanical behavior, we most desired an experimental verification of that prediction. One method to experimentally obtain the actual displacements of an element during a loading situation is to visually observe and measure them. We have, therefore, used high speed photography to examine the motion of our electrodes during impact. Only four series of tests have been run with speeds up to 9000 frames per second. There is little experimental difficulty in triggering and focus, etc. with our present system. The true value of this technique has not been developed or realized because of our termination of experimental work. It appears, however, that a great deal of information concerning the description of dynamic displacements could be gained by this method. Further work would have included the following: (1) use of the highest impact level and longer plates to provide larger and more easily observed displacements. (2) increase the framing rate of our present system (which is capable of 16,000 frames per second) to permit more accurate distance-time measurements. (3) use of a more accurately scribed reference grid which might employ the recently developed "Transfer Grid Method" of Moiré fringe analysis.

(2) Dynamic Strain Measurements

Although the experimental effort has not been extensive, some work has been done in the measurement of dynamic strain under impact conditions using the strain-gage techniques discussed earlier. Reasonable corrolation with our theoretical predictions was indicated before the experimental work ended. This portion of the report will indicate the relation of these preliminary findings to the theoretical predictions that have been made.

a. Aluminum Plates:

The mechanical properties of the aluminum alloys are well established and readily available. An aluminum plate loaded within it's elastic region is obviously a more well-behaved system than our porous plate material. Thus our initial experimental work was aimed at confirming our theoretical analysis by the use of an aluminum plate:

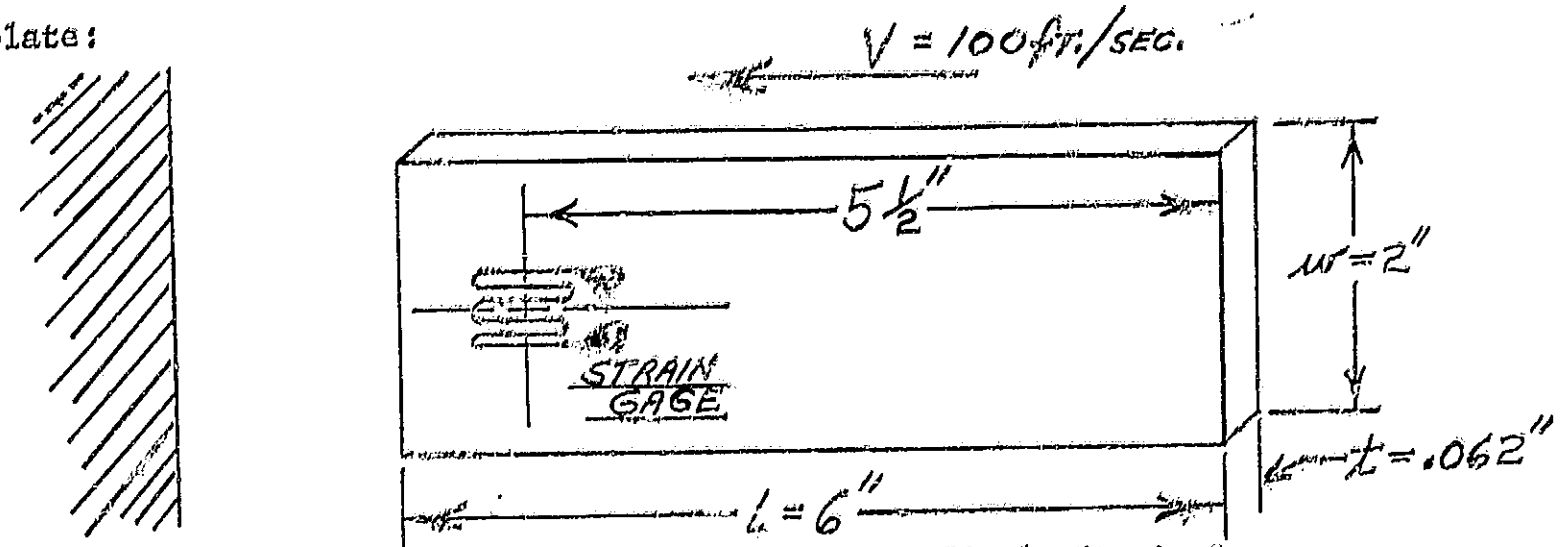

6061 - T6 Alloy:

$E = 10.0 \times 10^6$ PSI
$\sigma_Y = 40{,}000$ PSI
$\sigma_{ULT} = 45{,}000$ PSI
$\gamma = 0.0976$ #/in^3
$\rho = 0.00605$ #/in^2
$a = 16{,}600$ ft/sec

Single Strain Gage:

$R = 120\ \Omega$
$K = 2.0$
$E = 12.0$ Volts
$\Delta E = \frac{R^2\ KE\ (\Delta\varepsilon)}{(R\&R)^2} = (6.0)\ \Delta\varepsilon$

We could first calculate the natural frequency, f_{n_1}, of this element by either of the two equivalent equations we have given earlier:

$$f_{n_1} = 1/4 \sqrt{\frac{Eg}{\rho}} \quad \frac{\sqrt{E}}{L} \equiv 1 \left(\frac{a}{4L}\right)$$

and we find $f_{n_1} = 8{,}300$ cy/sec.

The lower trace of Fig. III-12 shows the acceleration time history of loading imposed on this plate during impact. We note that the pulse length (t_o) is 0.001 sec. The shock spectrum given in Fig. III-11, therefore, applies directly. Since the calculated $f_{n_1} = 8{,}300$ cy/sec >> 500 cy/sec, we can only conclude from this spectrum that

FIG. III-12

UPPER TRACE:

DYNAMIC STRAIN - 1 msec/cm; 1 mo/cm

LOWER TRACE:

ACCELERATION PULSE - 0.5 msec/cm; 1000 g/cm

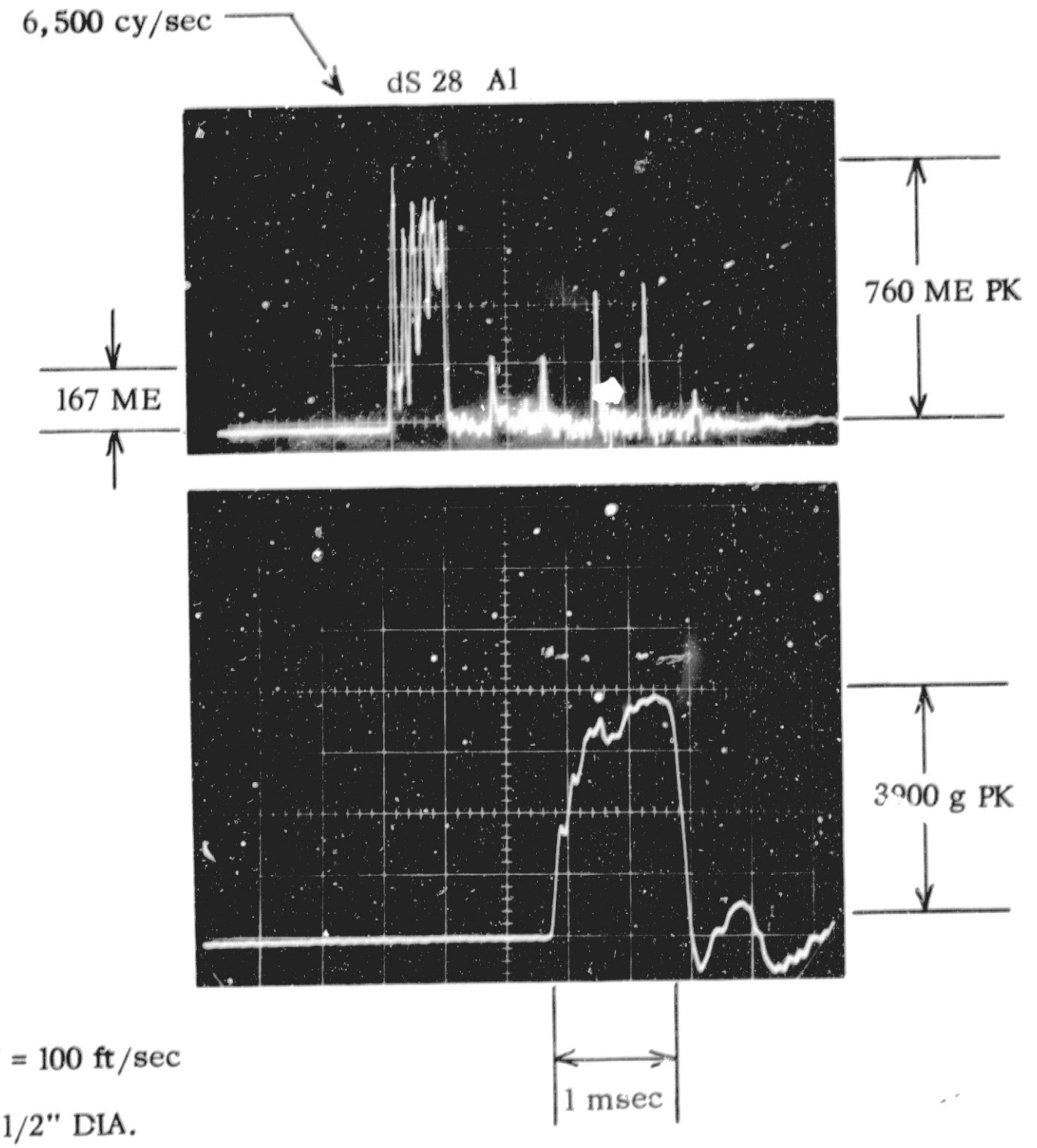

V = 100 ft/sec

1 1/2" DIA.

DYNAMIC STRAIN OSCILLOGRAPH OF AL PLATE

a dynamic amplification factor equal to 2.0 must be used.

Due to simple inertia loading, the static stress level at the gage location ($L' = 5\ 1/2''$) may be calculated:

$$\sigma = \frac{ma}{A} = \frac{(L' \cdot w \cdot t \cdot \gamma)}{g\ (w \cdot t)}\ (Ng) = L'\gamma N \Rightarrow \sigma_{static} = 2100 \text{ psi}$$

Employing the dynamic amplicfication:

$$\sigma_{dyn.} = 4200 \text{ psi}$$

And: $$\varepsilon_{DYN} = \frac{\sigma\ DYN}{E} = 420\ \mu\varepsilon$$

is the expected gage output under this loading condition. We now note that the upper trace of Figure III-12 has recorded an experimental peak strain of $\varepsilon = 760\ \mu$ in/in. Two considerations can modify this discrepancy. In the experimental record, it is possible that the subsequent peaks which indicate a more uniform 668 μ in/in peak strain level are truely more significant. The calculation of static stress was carried out in a simple and straightforward manner. However, our detailed theoretical analysis showed that a uniform elastic stress wave will propagate through the material and its magnitude at the gage location will be determined by total length ($L=6''$) because of the time durations involved, and recognition of the Cosine function of x. Therefore, with effective $L' = L = 6''$ we would calculate an expected $\varepsilon_{dyn} = 458\ \mu$ in/in. The difference between measured and calculated strain is then 210 μ in/in. This is quite encouraging as a very preliminary experimental result. Since $\epsilon_{meas} > \epsilon_{calc}$, we might rule out strain-rate effects and investigate inertia response of the gage and plastic deformation even though there is no residual recorded at the gage location.

The predicted natural frequency (f_n) of the cyclic displacement within our element was 8,300 cy/sec and should be recorded by the strain gage. The upper trace of Fig. III-12 shows this cyclic strain behavior within the plate at a frequency of approximately 6,500

cy/sec. Again, it is encouraging to see this preliminary corrolation but we cannot account for the discrepancy (1800 cy/sec) at this time. The true physical significance of the subsequent spikes at a frequency of approximately 1100 cy/sec (nearly the half-period of the loading pulse) is also not appreciated at this time.

We may now look at the experimental results and the predictions from our detailed analysis. We suspect that since the general stress equation (11) contains a cosine x term there will be little difference between the calculated max. stress (x = 0) and the stress at the gage location (x = L/12). It also appears that our series in the max. stress equation (12) converges to $\frac{\pi}{4}$. We may, therefore, calculate the max. elastic stress predicted:

$$\sigma_{max}(o, t) = \frac{-4EV}{a\pi}\left(\frac{\pi}{4}\right) = -\frac{EV}{a} = -60{,}000 \text{ PSI}$$

Now:

$$60{,}000 \text{ PSI} > 40{,}000 \text{ PSI} = \sigma_{yield}$$

In fact not only plastic deformation is implied but 60,000 PSI $> \sigma_{ult}$!

Even if we assume that a high strain-rate sensitivity elevates the dynamic yield stress and the elastic modulus still applies we have:

$$\varepsilon_{predicted} = \frac{\sigma}{E} = 6{,}000\ \mu\varepsilon$$

This value is > 0.2% ε normally taken as the yield point, yet there was no observation of plastic deformation after repeated loading at this impact level. Furthermore the experimental strain trace showed no residual strain (plastic or lack of Zero return) yet the fact remains:

760 $\mu\varepsilon$ PK	<<	6,000 $\mu\varepsilon$ PK
Experimental		Predicted

There is another way to study the implications of the predictions since we know from similar work that the maximum particle velocity that can be obtained in this elastic

element is:

$$v = \frac{a\sigma_{yield}}{E} = 66.4 \text{ ft/sec}$$

Now since v < V applied to the end, we must form a compressed zone of which the loaded end must suffer plastic deformation. However, plastic deformation is not observed and our only conclusion must be that our analytical prediction is nearly an order of magnitude conservative ! The fault must lie in the first boundary conditon we have assumed:

$u_{(o,t)} = o$ implies no carriage displacement during the loading period:

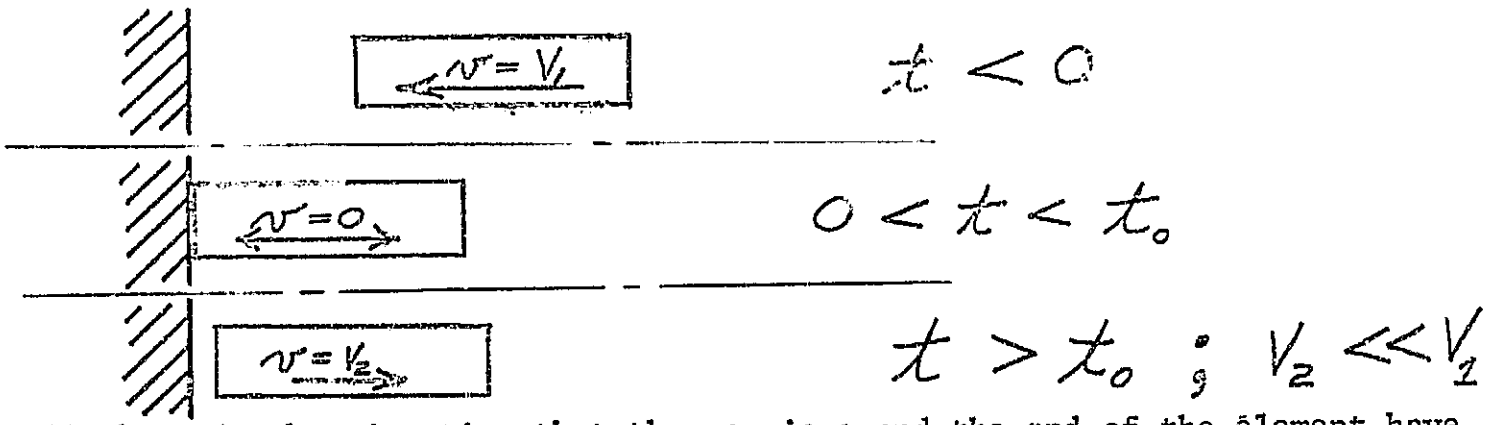

What we really have is the situation that the carriage and the end of the element have an absolute displacement during the loading period:

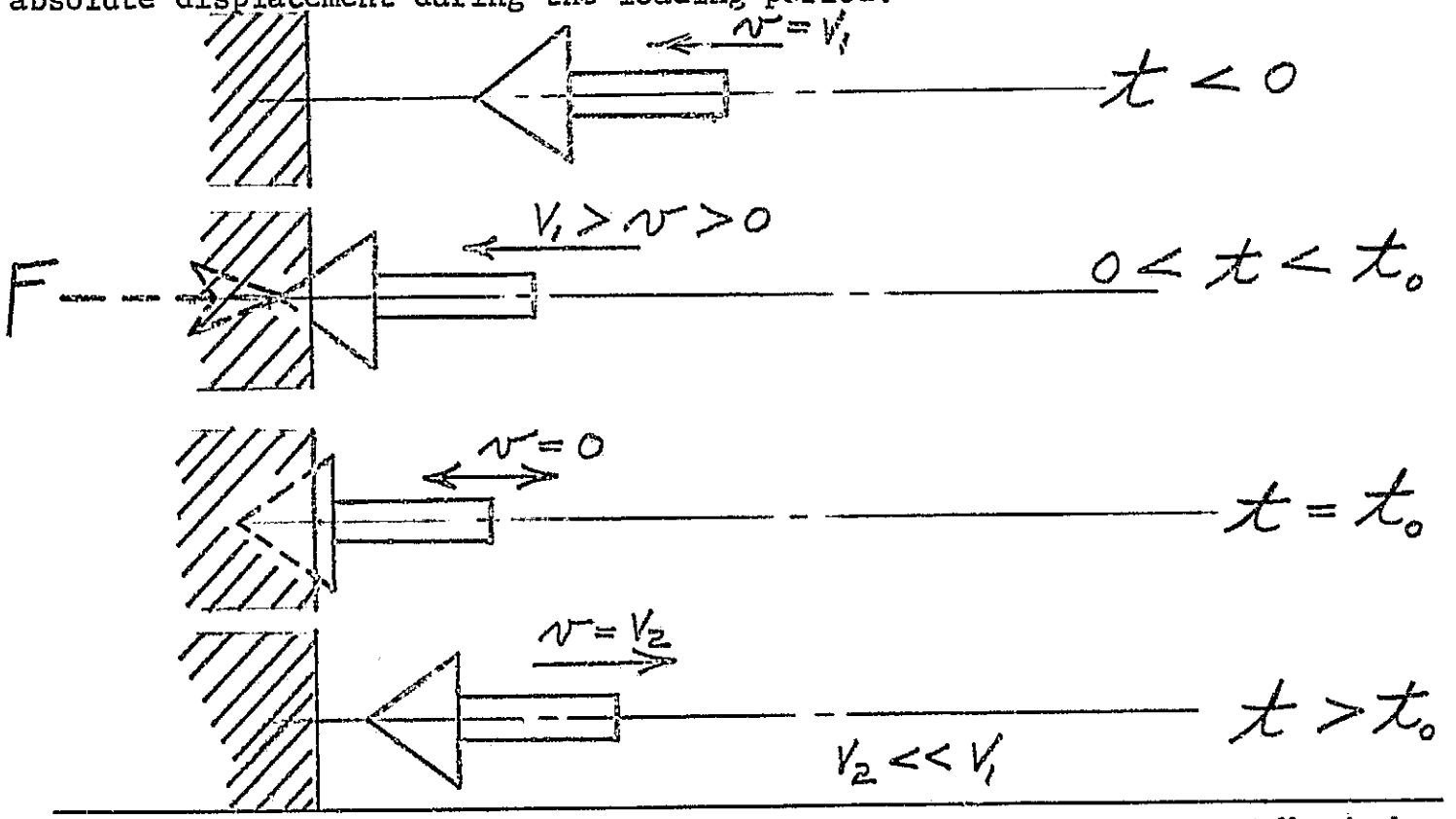

metallurgical
materials division

Thus we must modify our analytical prediction if time permits to account for this boundary condition. Consideration of this, of course, will reduce the predicted magnitude and have a strong effect on the discrepancy that has been brought out by our preliminary experimental results.

(b) Ni - Cd Electrodes:

Following our study of the aluminum plate, we have obtained some preliminary results on the negative electrode.

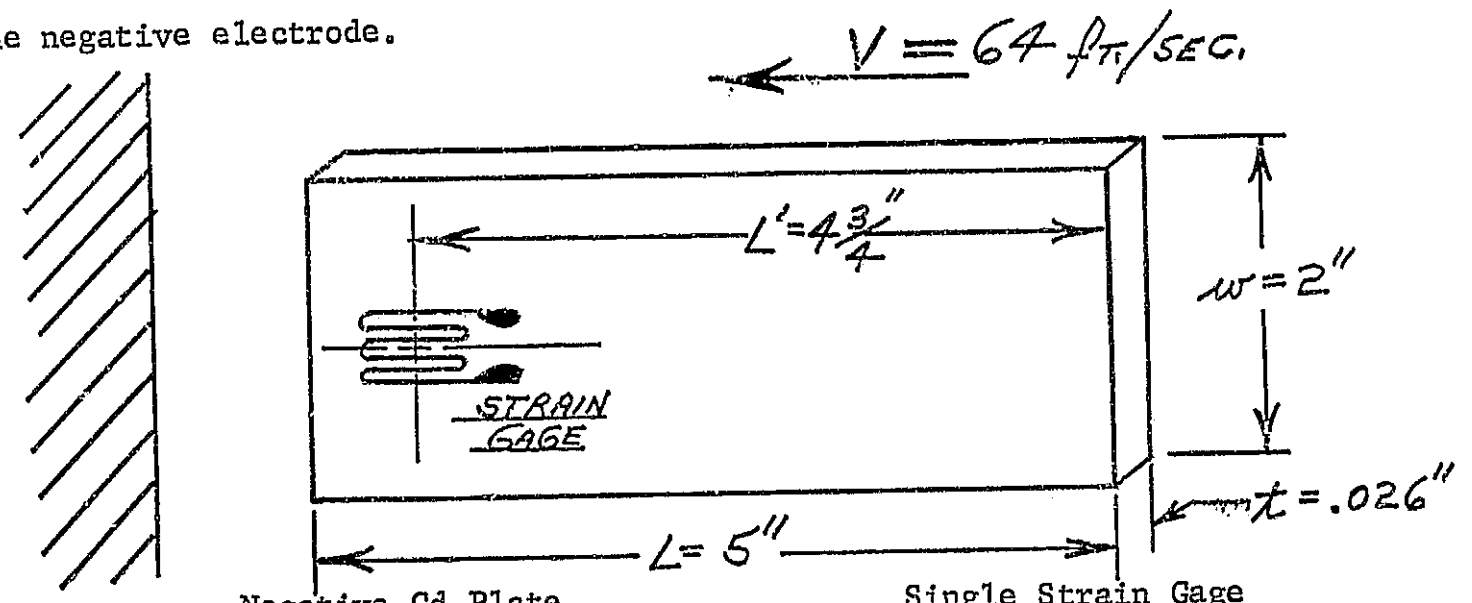

$E \approx 0.5 \times 10^6$ PSI
$\sigma_{comp.\ ult.} \approx 3000 - 5000$ PSI
$\gamma = 0.127$ #/in^3
$\rho = 0.0033$ #/in^2
$\alpha \approx 3250$ ft/sec

AF-7-1-56 (E-910)
$\Delta E = (6.0)\,\Delta E$

Again, it is first useful to determine the natural frequency of this element either by calculation as before or directly from Figure III-10 for this case.

$$f_{n_1} \approx 2000 \text{ cy/sec}$$

The lower trace of Figure III-13 shows the acceleration-time history of the loading and the pulse length t_o is approximately 1.4 msec. Thus, we cannot use the shock spectrum of Figure III-11 directly ($t_o \not\approx$ .001sec). However, the amplification factor of 2.0 will apply to any element with a $f_{n_1} > 356$ cy/sec for this loading pulse if we assume

FIG. III-13

UPPER TRACE:

DYNAMIC STRAIN - 2 msec/cm; 5 mo/cm

LOWER TRACE:

ACCELERATION PULSE - 0.5 msec/cm; 1000 g/cm

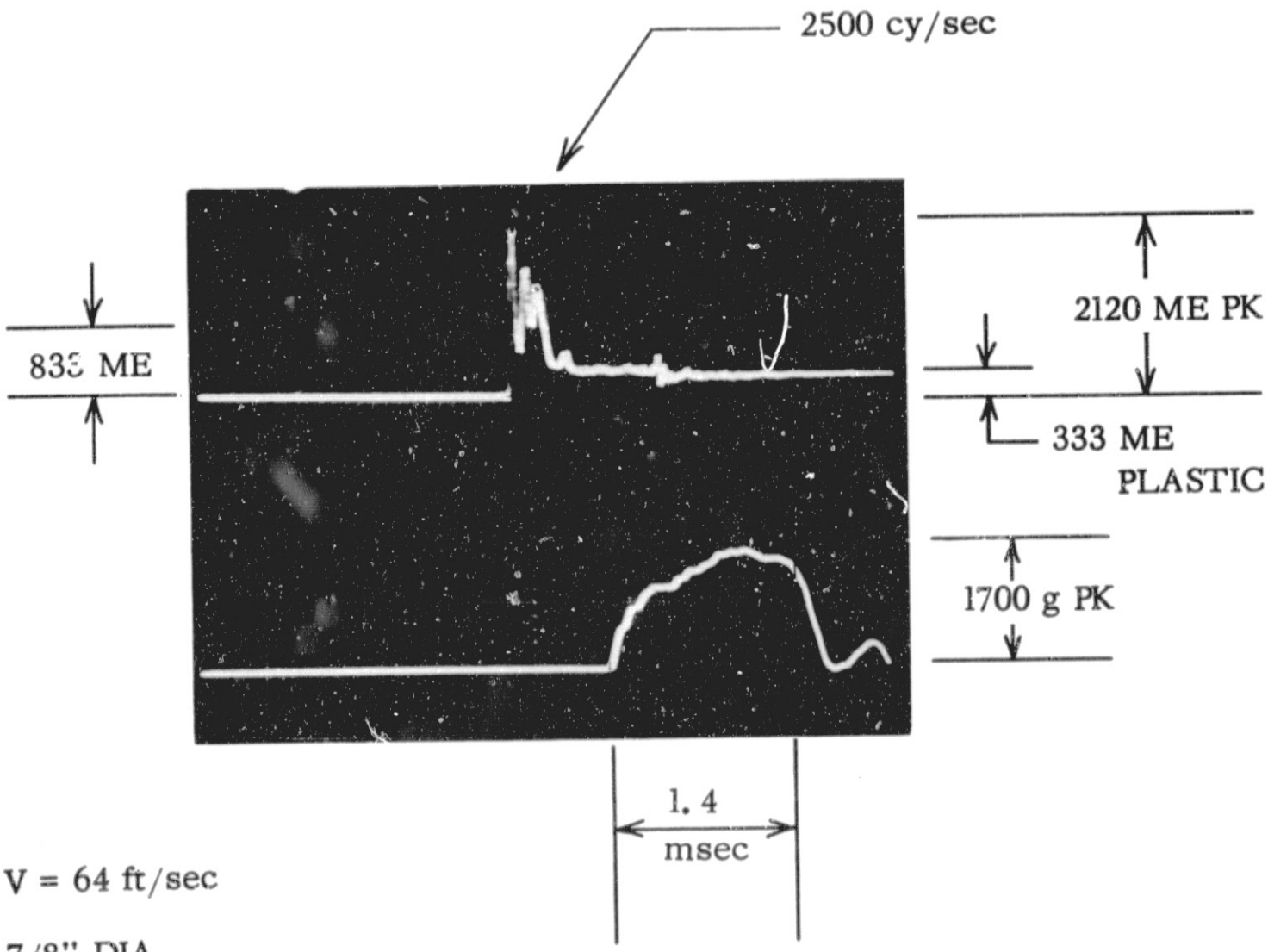

V = 64 ft/sec

7/8" DIA.

d = 0.367"

DYNAMIC STRAIN OSCILLOGRAPH OF Cd ELECTRODE

it is square. It is obvious that f_{n_1} = 2000 cy/sec >> 356 cy/sec and the maximum amplification factor will apply. The maximum will apply for any shape pulse of this duration. However, we could question the use of the square wave for this low velocity impact level and assume the experimental record more closely approximates a half-sine pulse. If this is true, a maximum amplification factor of 1.8 will apply.

The upper trace of Figure III-13 shows a cyclic strain behavior within the electrode at a frequency of approximately 2500 cy/sec. This is in good agreement with our predicted 2000 cy/sec. Futhermore, it implies that the governing elastic modulus may be higher:

$$E = \left(\frac{f_h L}{14}\right)^2 = 0.8 \times 10^6 \text{ PSI}$$

Which is reasonable with respect to many earlier experimental observations.

We may now calculate the maximum stress due to simple inertia loading (using the total length L):

$$\sigma = \frac{ma}{A} = L\gamma N = 1080 \text{ PSI}$$

Retaining the 2.0 x amplification factor:

$$\sigma_{dyn} = 2160 \text{ PSI}$$

which implies: $\epsilon = \frac{\sigma}{E} = 4300\,\mu$ in/in PK.

The upper trace of Figure III-13 has recorded an experimental peak strain level of only 2120 μ in/in. There is one consideration that might help explain this discrepancy although we have no experimental confirmation at this time. We know that if a material is one-half critically damped (C/C_c =0.5) , its maximum amplification factor for a half-sine pulse is only 1.1 and further, the experimental strain trace has indicated a modulus of E $\simeq 0.8 \times 10^6$ PSI. If both factors are taken into account we would predict a peak strain of only 1470 μ in/in. This is lower than the recorded peak yet equal to the approximately 1450 μ in/in strain level recorded by subsequent peaks.

This is likely an optimistic consideration but is important enough that it should be investigated if work were continued since it is a very beneficial material property of this porous electrode. The simple explanation for the 50% experimental value is the reinforcement effect of the strain gage which has been documented in table III-5 and III-6 of this report.

It is important to note the lack of zero-return in the upper trace of Figure III-13. This indicates a residual plastic strain of 333 μ in/in. The 0.21% PK strain recorded is also reasonable from our observations of apparent absence of permanent set. When entered on the $\sigma-\varepsilon$ curve (Figure III-C. JPL 8TH quarter report) for Negative Plate we would expect as much as 40% of the total strain could be plastic. The lower value recorded experimentally is neither appreciated nor bothersome at this preliminary stage. What is important is the ability of this technique to record into this region of higher strain levels.

Considering the complete analysis, we could evaluate the stress by equation (12) as we did for aluminum:

$$\sigma_{max}(o,t) = \frac{-4EV}{a\pi}\left(\frac{\pi}{4}\right) = 9850 \text{ PSI}$$

If our origiral values E = 0.5 x 10^6 PSI and a = 3250 ft/sec are used for our 64 ft/sec impact. This value of $\sigma_{max} >> \sigma_{ult}$ as was the case for the aluminum plate analysis. The reasons for this discrepancy have been discussed in the previous section. In conclusion, the experimental measurement of dynamic strain during impact loading has been accomplished. The frequency data of elastic wave propagation that has been obtained may be our most valuable tool for determining the value of the dynamic modulus of elasticity. The ability to measure the residual plastic strain component in a total strain level has also been demonstrated. This ability will allow us to very accurately determine the dynamic $\sigma-\varepsilon$ curve from a number of tests. Information well beyond the em-

pirical yield point 0.2% ε seems very possible. The preliminary magnitudes that have been recorded are satisfactory at this time. In the case of aluminum, agreement was good and it is felt that the experimental data will corrolate very well with the predictions that can be made from the detailed analysis with proper boundary condition modification. We also need this boundary condition modification for electrodes in order to resolve the present magnitude discrepancies. The interplay of: (1) strain-gage reinforcement, (2) amplification factor based on pulse shape as well as frequency, (3) viscous damping of the porus material, (4) accuracy of E value, and (5) the compressional strain-gage behavior, have been briefly described. With an accurate experimental determination of E, σ may be accurately calculated from equation (12) if we have made the analytical modifications indicated. Then, we are confident that the dynamic amplification can be accurately determined for future use.

(d) BIBLIOGRAPHY

1. Shock and Vibration Handbook Vol 1,2,3 Ed. C.M. Harris and C.E. Crede, McGraw-Hill, 1961

2. Theory of Elasticity, S. Timoshenko and J.N. Goodier, McGraw-Hill, 1951

3. Engineering Vibrations, L.S. Jacobsen and R.S. Ayre, McGraw-Hill, 1958

4. Vibration and Shock in Damped Mechanical Systems, J.C. Snowdon, Wiley, 1968

5. Advanced Engineering Mathematics, C.R. Wylie, McGraw-Hill, 1960

6. Fourier Series and Boundary Value Problems, R.V. Churchill, McGraw-Hill, 1963

7. Vibration Problems in Engineering, S. Timoshenko, Van-Nostrand, 1955

8. Dynamics of Package Cushioning, R.D. Mindlin, Bell System Technical Journal, page 353, July-Oct., 1945

9. The Effect of Pulse Shape on Simple Systems Under Impulsive Loading, C.E. Crede, ASME Trans, page 957, August, 1955

10. Improved Sonic Apparatus for Determining the Dynamic Modulus of Concrete Specimens, C.E. Goodell, Proc. Amer. Concrete Institute, page 53, Sept. 1950

11. Effects of Impact on Simple Elastic Structures, J.M. Frankland, Proc. Soc. for Experimental Stress Analysis, page 7, 6, #2, 1948

12. Specification of Shock Tests C.E. Crede, SAE Paper 585B, 1962

13. Basic Shock and Vibration Theory, D. Pennington, Endevco Technical Paper #219, 1966

14. Prediction and Evaluation of Sensitivity to Transient Accelerations, M. Kornhauser, J. Applied Mechanics, page 371, December, 1954

15. Some Shock Spectra Characteristics And Uses, Y.C. Fung and M.V. Barton, J. Applied Mechanics, page 365, September, 1958

16. Shock Spectrum As A Criterion of Severity of Shock Impulses, C.T. Morrow, J. Acoustical Socity of Amer., page 596, 29, #5 May 1957

17. Response of Damped Elastic Systems To Transient Disturbances, R.D. Mindlin, Proc. Soc. for Experimental Stress Analysis, page 69, 5, #2, 1948

18. Design Criteria for Generalized High Strain, G. Kardos, Trans. ASME -, J. Engr. for Industry, page 485, August 1968

19. Shock Measurement, Bruel & Kjaer Technical Review #3, 1966